

| REPORT DOCUMENTATION PAGE  |  |   | Form Approved<br>OMB No. 0704-0188                |  |
|--|--|---|---|--|
| Public reporting burden for this collection of information is estimated to average 1 hour per response, including the time for reviewing instructions, searching existing data sources, gathering and maintaining the data needed, and completing and reviewing the collection of information. Send comments regarding this burden estimate or any other aspect of this collection of information, including suggestions for reducing this burden, to Washington Headquarters Services, Directorate for Information Operations and Reports, 1215 Jefferson Davis Highway, Suite 1204, Arlington, VA 22202-4302, and to the Office of Management and Budget, Paperwork Reduction Project (0704-0188), Washington, DC 20503. |  |   |   |  |
| 1. AGENCY USE ONLY (Leave blank)   |  | 2. REPORT DATE<br>7.Apr.00                  |   | 3. REPORT TYPE AND DATES COVERED<br>THESIS |
| 4. TITLE AND SUBTITLE<br>DESIGN, FABRICATION, AND MODEL DEVELOPMENT OF A SPACECRAFT TEST-BED FOR SIX-AXIS ACTIVE VIBRATION ISOLATION AND PRECISION POINTING  |  |   | 5. FUNDING NUMBERS                                |  |
| 6. AUTHOR(S)<br>2D LT ZUMBRUNNEN CLINTON R   |  |   |   |  |
| 7. PERFORMING ORGANIZATION NAME(S) AND ADDRESS(ES)<br>UNIVERSITY OF WASHINGTON   |  |   | 8. PERFORMING ORGANIZATION<br>REPORT NUMBER       |  |
| 9. SPONSORING/MONITORING AGENCY NAME(S) AND ADDRESS(ES)<br>THE DEPARTMENT OF THE AIR FORCE<br>AFIT/CIA, BLDG 125<br>2950 P STREET<br>WPAFB OH 45433  |  |   | 10. SPONSORING/MONITORING<br>AGENCY REPORT NUMBER |  |
| 11. SUPPLEMENTARY NOTES  |  |   |   |  |
| 12a. DISTRIBUTION AVAILABILITY STATEMENT<br>Unlimited distribution<br>In Accordance With AFI 35-205/AFIT Sup 1   |  |   | 20000424 226                                      |  |
| 13. ABSTRACT (Maximum 200 words)   |  |   |   |  |
| 14. SUBJECT TERMS  |  |   | 15. NUMBER OF PAGES<br>106                        |  |
|  |  |   | 16. PRICE CODE                                    |  |
| 17. SECURITY CLASSIFICATION<br>OF REPORT   |  | 18. SECURITY CLASSIFICATION<br>OF THIS PAGE |   | 19. SECURITY CLASSIFICATION<br>OF ABSTRACT |
|  |  |   |   | 20. LIMITATION OF<br>ABSTRACT              |

DTIC QUALITY INSPECTED 3

University of Washington

Abstract

DESIGN, FABRICATION, AND MODEL DEVELOPMENT  
OF A SPACECRAFT TEST-BED FOR SIX-AXIS ACTIVE  
VIBRATION ISOLATION AND PRECISION POINTING

Clinton R. ZumBrunnen

Chairman of the Supervisory Committee:

Assistant Professor Mark Campbell

Department of Aeronautics and Astronautics

This thesis describes the design, fabrication, model development, and model verification for a test-bed that simulates a mechanically noisy spacecraft bus. The test-bed includes an aluminum node-and-strut truss structure, articulating solar arrays, electromagnetic shaker mounts, attachment points for fuel tanks, and a soft spring suspension system to simulate a 0-g environment. A detailed finite element model of the system was developed, and experimental modal analysis coupled with model updating techniques was used to verify and improve the finite element model for the spacecraft test-bed. Model updating reduced the average error in the first twelve flexible modes of the system from 3.7% to 1.3%.

The University of Washington is currently investigating the benefits of active vibration isolation and precision pointing for the next generation of spacecraft. Research with such devices is important because the performance of multiple satellite clusters, applicable to communications and Earth and Space Science missions, requires an upgrade from RF to optical cross-links. With this upgrade comes a 10,000-fold increase in pointing requirements, which cannot be met with conventional methods. Current research utilizes multivariable control of a six-axis active vibration isolation and pointing device, or hexapod. The newly developed spacecraft test-bed can simulate realistic disturbance inputs on the noisy side of the hexapod to investigate its effectiveness in a more realistic setting. Such disturbances include reaction wheel imbalances, fluid slosh, and vibration from mechanical devices such as solar array drives.

DESIGN, FABRICATION, AND MODEL DEVELOPMENT  
OF A SPACECRAFT TEST-BED FOR SIX-AXIS ACTIVE  
VIBRATION ISOLATION AND PRECISION POINTING

Clinton R. ZumBrunnen

A thesis submitted in partial fulfillment of the requirements  
for the degree of

Master of Science in Aeronautics and Astronautics

University of Washington

1999

Department of Aeronautics and Astronautics

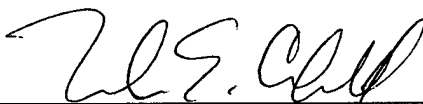
University of Washington  
Graduate School

This is to certify that I have examined this copy of a master's thesis by

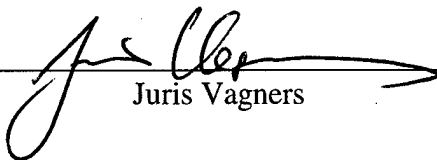
Clinton R. ZumBrunnen

and have found that it is complete and satisfactory in all respects,  
and that any and all revisions required by the final  
examining committee have been made.

Committee Members:



Mark Campbell



Juris Vagners

Date:

9/27/99

In presenting this thesis in partial fulfillment of the requirements for a Master's degree at the University of Washington, I agree that the library shall make its copies freely available for inspection. I further agree that extensive copying of this thesis is allowable only for scholarly purposes, consistent with "fair use" as prescribed in the U.S. Copyright Law. Any other reproduction for any purposes or by any means shall not be allowed without my written permission.

Signature\_\_\_\_\_

Date\_\_\_\_\_

# Table of Contents

|   |     |
|---|-----|
| Table of Contents .....                                     | i   |
| List of Figures .....                                       | iii |
| List of Tables.....   | vi  |
| Acknowledgements .....                                      | vii |
| Chapter 1: Introduction .....                               | 1   |
| 1.1 Motivation.....   | 1   |
| 1.2 Previous work .....                                     | 4   |
| 1.3 Organization.....                                       | 5   |
| Chapter 2: Background Information .....                     | 7   |
| 2.1 Future Systems Overview .....                           | 7   |
| 2.2 Interferometry .....                                    | 7   |
| 2.2.1 Space Technology 3 .....                              | 10  |
| 2.2.2 Stellar Interferometry Mission .....                  | 11  |
| 2.3 Space Communications.....                               | 13  |
| 2.4 Other Applications .....                                | 15  |
| 2.5 Summary of Pointing and Control Requirements .....      | 16  |
| Chapter 3: Test-Bed Design .....                            | 18  |
| 3.1 UW Hexapod .....  | 18  |
| 3.2 First Generation test-bed setup .....                   | 19  |
| 3.3 Second Generation Test-Bed Design and Construction..... | 20  |
| 3.3.1 Main Truss Structure .....                            | 21  |
| 3.3.2 Solar Array Structure.....                            | 26  |
| 3.3.3 Suspension System .....                               | 28  |
| Chapter 4: Finite Element Model .....                       | 33  |
| 4.1 Objective and Tools Used .....                          | 33  |
| 4.2 The Finite Element Model .....                          | 33  |
| 4.2.1 The Elements Used.....                                | 34  |
| 4.2.2 Modeling The Structure.....                           | 38  |
| 4.2.3 The FEM's Significant Modeshapes .....                | 48  |
| 4.3 Converting the Model from ANSYS to MATLAB .....         | 53  |
| 4.4 Creating the Input-Output State Space Model .....       | 55  |
| Chapter 5: Data Collection and Model Correlation .....      | 58  |

|   |  |     |
|---|--|-----|
| 5.1   | Modal Analysis Setup .....                   | 58  |
| 5.2   | Electromagnetic Shaker model .....           | 61  |
| 5.3   | Data collection and model correlation .....  | 62  |
| Chapter 6: Model Updating.....                  |  | 72  |
| 6.1   | Parameters Varied .....                      | 72  |
| 6.2   | Finite Difference Method.....                | 73  |
| 6.3   | Updating Results .....                       | 76  |
| 6.4   | Updated Finite Element Model Properties..... | 84  |
| Chapter 7: Conclusions and Recommendations..... |  | 87  |
| 7.1   | Conclusions.....                             | 87  |
| 7.2   | Recommendations.....                         | 88  |
| Bibliography.....                               |  | 90  |
| Appendix A. Modeling M-files .....              |  | 92  |
| Appendix B. Updating M-files .....              |  | 100 |

## List of Figures

|  |    |
|--|----|
| Figure 1.1: First generation Hexapod test-bed setup.....                                 | 3  |
| Figure 1.2: Bird's eye view of the Micro Precision Interferometer test-bed. ....         | 4  |
| Figure 1.3: Topography of the Honeywell Satellite Test-bed. ....                         | 5  |
| Figure 2.1: Interferometry Diagram. ....   | 8  |
| Figure 2.2: Old Space Technology 3 system deployed. ....                                 | 10 |
| Figure 2.3: Stellar Interferometry Mission. ....   | 12 |
| Figure 2.4: Illustration of Teledesic Constellation. ....                                | 14 |
| Figure 2.5: Illustration of the LandSat Co-Flyer and ALPHA missions. ....                | 16 |
| Figure 3.1: UW Hexapod configuration.....  | 18 |
| Figure 3.2: UW Hexapod strut design.....   | 19 |
| Figure 3.3: The second generation test-bed.....  | 20 |
| Figure 3.4: Final design of the test-bed main truss. ....                                | 22 |
| Figure 3.5: First mode shape of main truss. ....   | 24 |
| Figure 3.6: Top view of the two structural aluminum plates. ....                         | 25 |
| Figure 3.7: Solar array configuration and first modeshape. ....                          | 27 |
| Figure 3.8: Top view, solar array drive mechanism. ....                                  | 28 |
| Figure 3.9: Suspension truss load case and first mode shape at 22Hz. ....                | 29 |
| Figure 3.10: Side view of the test-bed suspended from the overhead truss. ....           | 30 |
| Figure 4.1: The BEAM4 element configuration. ....  | 35 |
| Figure 4.2: SHELL63 element configuration.....   | 36 |
| Figure 4.3: PIPE16 element configuration.....  | 37 |
| Figure 4.4: COMBIN14 element configuration .....   | 38 |
| Figure 4.5: MASS21 element configuration. ....   | 38 |
| Figure 4.6: Finite element model of the spacecraft test-bed structure in ANSYS. ....     | 39 |
| Figure 4.7: Element mesh of the top plate.....   | 40 |
| Figure 4.8: Photo of the actual connection between the top plate and the truss. ....     | 40 |
| Figure 4.9: Photo of the truss tube ends and the aluminum nodes.....                     | 41 |
| Figure 4.10: Modeled connection between the top plate and the truss.....                 | 41 |
| Figure 4.11: Picture of the truss model where the plates have been removed for clarity.. | 43 |
| Figure 4.12: Photo of the actual middle joint under the middle plate. ....               | 44 |
| Figure 4.13: Configuration of the middle joint on the structure. ....                    | 44 |
| Figure 4.14: Element mesh of the middle plate. ....                                      | 45 |
| Figure 4.15: Mesh of the model solar array. ....   | 46 |



|  |    |
|--|----|
| Figure 4.16: Photo of the shaker mounted on the disturbance node. ....                         | 47 |
| Figure 4.17: Mesh at the disturbance node. ....  | 47 |
| Figure 4.18: Pinned boundary conditions and 1-g acceleration applied to the model. ....        | 48 |
| Figure 4.19: First mode of the solar arrays. ....  | 49 |
| Figure 4.20: Another of six solar array modes. ....  | 50 |
| Figure 4.21: The first mode of the main truss at 21.3 Hz. ....                                 | 51 |
| Figure 4.22: The second mode of the main truss in the global Y-direction. ....                 | 51 |
| Figure 4.23: 3 <sup>rd</sup> mode of the main truss in the global Y-direction. ....            | 52 |
| Figure 4.24: First mode where motion is primarily in the global Z-direction. ....              | 53 |
| Figure 4.25: The shaker model block diagram. ....  | 57 |
| Figure 4.26: Shaker and Test-bed systems combined in series. ....                              | 57 |
| Figure 5.1: Modal analysis setup. ....   | 58 |
| Figure 5.2: The Kistler accelerometer (type 8630C) and signal-conditioning unit. ....          | 59 |
| Figure 5.3: Schematic of the data collection setup up. ....                                    | 60 |
| Figure 5.4: Location of the accelerometers that produced the experimental TFs. ....            | 60 |
| Figure 5.5: Transfer function from $V_{in}$ to an accelerometer on the proof mass. ....        | 62 |
| Figure 5.6: Shows the location of the accelerometers used to take data in Y-direction ...      | 64 |
| Figure 5.7: TF from the shaker $V_{in}$ to an accelerometer at the bottom center node. ....    | 65 |
| Figure 5.8: TF from the shaker $V_{in}$ to an accelerometer at the middle center node. ....    | 65 |
| Figure 5.9: TF from the shaker $V_{in}$ to an accelerometer at the top center node. ....       | 66 |
| Figure 5.10: Shows the location of the accelerometers used to take data in Z-direction ..      | 66 |
| Figure 5.11: TF from the shaker $V_{in}$ to an accelerometer at right bottom center node. .... | 67 |
| Figure 5.12: TF from the shaker $V_{in}$ to an accelerometer at right middle center node. .... | 68 |
| Figure 5.13: TF from the shaker $V_{in}$ to an accelerometer at the right top front node. .... | 68 |
| Figure 5.14: Shows the location of the accelerometers used to take data in X-direction. ....   | 69 |
| Figure 5.15: TF from the shaker $V_{in}$ to an accelerometer at back bottom center node. ....  | 70 |
| Figure 5.16: TF from the shaker $V_{in}$ to an accelerometer at back middle center node. ....  | 70 |
| Figure 5.17: TF from the shaker $V_{in}$ to an accelerometer at the back top right node. ....  | 71 |
| Figure 6.1: Flow Chart of the update process. ....   | 76 |
| Figure 6.2: Updated TF from the shaker $V_{in}$ to an accel. at the bottom center node. ....   | 78 |
| Figure 6.3: Updated TF from the shaker $V_{in}$ to an accel. at the middle center node. ....   | 78 |
| Figure 6.4: Updated TF from the shaker $V_{in}$ to an accel. at the top center node. ....      | 79 |
| Figure 6.5: Updated TF from the shaker $V_{in}$ to an accel. at right bottom center node. .... | 80 |
| Figure 6.6: Updated TF from the shaker $V_{in}$ to an accel. at right middle center node. .... | 80 |
| Figure 6.7: Updated TF from the shaker $V_{in}$ to an accel. at the right top front node. .... | 81 |

- Figure 6.8: Updated TF from the shaker  $V_{in}$  to an accel. at back bottom center node..... 82
- Figure 6.9: Updated TF from the shaker  $V_{in}$  to an accel. at back middle center node..... 82
- Figure 6.10: Updated TF from the shaker  $V_{in}$  to an accel. at the back top right node ..... 83

## List of Tables

|   |    |
|---|----|
| Table 2.1: Summary of pointing and measurement requirements.....  | 17 |
| Table 3.1: Fundamental frequencies for typical launch systems.....  | 21 |
| Table 3.2: Summary of the elements used to model the main truss structure.....  | 23 |
| Table 3.3: Spring deformation, spring constants, and bounce frequencies for supports...   | 30 |
| Table 6.1: List of the parameters used in the model updating process. ....  | 72 |
| Table 6.2: Frequencies for the first four modes in each global direction for the original<br>model, experimental data, and the updated model.. .... | 84 |
| Table 6.3: Summary of the finite element model information for the updated model.....   | 85 |
| Table 6.4: Summary of change in the parameters. ....  | 86 |

## Acknowledgements

I first want to thank Professor Mark Campbell for his efforts in helping me complete this project. Without his foresight, guidance, expertise, and never-ending fountain of advice, I would not have finished this degree in one year. He always seemed to know how to push me in the right direction when I was stopped with a problem. I only hope the future usefulness of the device I constructed will be worth the time and effort Mark expended to help me finish on time.

I also need to thank Greg Lipski and Dennis Peterson for their advice in the construction phase of this project. Greg extended his expertise to help me design and build electronic drives on the structure, and he also gave me advice when I set up the modal analysis test equipment. Furthermore, without Dennis Peterson's guidance, the machining process would have consumed even more of my precious time. Thanks also to Dr. Juris Vagners for agreeing to be on my supervisory committee with such short notice.

Thanks to Thomas, Shane, Brian, Geir, and Shelby. Your humor, companionship, and advice did not go unnoticed. Good luck to you as finish your degrees and start new jobs. I also need to thank Amanda for her companionship and patience over the last year. When I would study too much, she would make me walk in the sun. When I spent too much time in the lab, she would take me to climb mountains. She keeps me focused on what is important. Finally, I need to thank my parents, Mel and Lola. They have been a constant source of inspiration and encouragement, and another reminder of what is truly important.

## **Chapter 1: Introduction**

### **1.1 Motivation**

Many innovations are responsible for continued advancement in the utility of spacecraft for defense, commercial, and scientific missions. They include micro-electromechanical systems or MEMS that will allow spacecraft to be smaller, lighter, cheaper, and better performing than ever before; advances in artificial intelligence and autonomous control that will make multiple spacecraft formation flight possible; and electric propulsion systems that will harness the power of the sun to maneuver spacecraft, further than ever before without the limitations of finite on-board fuel cells. Vibration isolation and precision pointing technology--the motivation for this thesis--is another key technology that will increase the pointing accuracy of spacecraft payloads by many orders of magnitude. Because of the strides made in these key technologies and others, the world will soon see space projects unimaginable when the Space Age took off in the 1950's and 60's.

The performance of multiple satellite clusters, applicable to communications and Earth and space science, will ultimately be limited by the ability to upgrade from RF to optical cross-links. This upgrade comes with an increased set of pointing requirements 10,000 times more precise than RF communications. Science and commercial spacecraft will benefit from the precision pointing technologies largely developed by the American Department of Defense (DoD) in the last two decades, because next generation spacecraft must incorporate a combination of vibration isolation and advanced active control to satisfy these stringent pointing requirements. In its efforts to develop high-energy-laser weapon systems, the military found that the efficiency of a laser weapon system depends heavily on controlling pointing jitter caused by small disturbance inputs. Military researchers spent the last two decades inventing methods and components to precisely point lasers and other instruments to minimize the loss in the laser's "on-target" power due to beam jitter [20]. Much of this precise pointing technology can now be leveraged for non-military use. Thus, the future will soon see civilian organizations incorporating

active vibration isolation and precision pointing techniques with laser technology for both scientific and commercial space missions.

Precision pointing technology developed for use by the armed forces is now found in many scientific and commercial project designs slated for the turn of the century, because much of the technology is naturally suited for these missions. In missions such as NASA's Space Technology 3 (ST3)[16] and Stellar Interferometry Mission (SIM)[19], advances in precision pointing will allow astronomers to measure objects in the heavens hundreds of times more accurately than ever before [19]. This increased accuracy will allow astronomers to detect Earth-like planets in orbit around the stars nearest our solar system. Advanced precision pointing techniques will also allow communication visionaries such as Bill Gates and Craig McCaw to use high-data-rate laser-communication intersatellite links to create their orbiting "Internet in the Sky." They call their high-speed networked system of 288 Low Earth Orbiting (LEO) satellites Teledesic [13]. Teledesic's optical intersatellite links will only be possible because of precision pointing technology. Early next decade, Teledesic will bring the Internet to users in places where regular telephone and fiber-optic lines do not exist. Finally, the world will also see new remote sensing missions demand stringent pointing requirements for payloads [20]. Precision pointing will allow missions such as NASA's Landsat Co-Flyer to produce images and maps of the entire Earth with unprecedented accuracy. The Landsat mission depends on precision pointing technology to point its cameras [10].

The scientific and commercial missions briefly described above share a commonality with laser weapon systems. Their effectiveness largely depends on effective line-of-site jitter minimization. For most precision pointing missions, major sources of jitter include momentum transfer devices such as momentum or reaction wheels, solar array drive mechanisms, fluid slosh disturbances, and specialized devices with moving or rotating mass such as cryocoolers [17]. Often, devices such as cryocoolers must be collocated with a payload to minimize heat flux or the amount of fluid needed to travel through long pipes. With disturbances such as these, an actively controlled device must cancel out their effects on a sensitive camera or laser transmitter. To reduce performance degradation that accompanies jitter from outside disturbances,

most new systems will use a device that both separates a sensitive payload from a noisy spacecraft and allows for precise pointing control of the payload. One current solution to the jitter problem is the six-axis active vibration isolation mount with precision pointing capability.

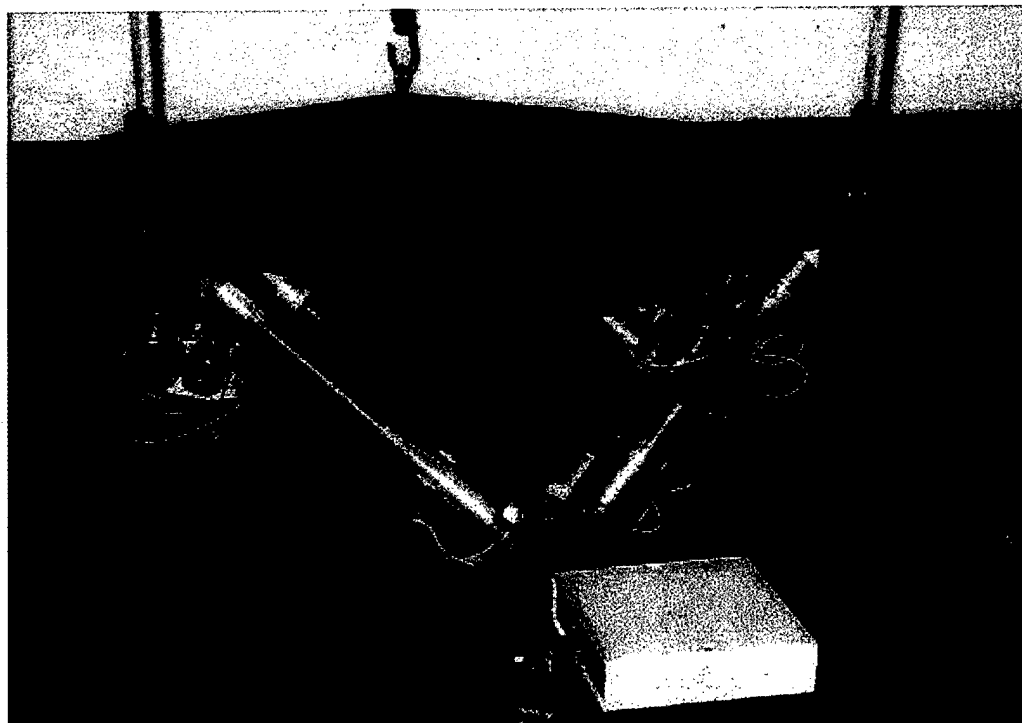


Figure 1.1: First generation Hexapod test-bed setup.

Over the last few years, several companies and agencies developed their own versions of the six-axis active isolation device. The University of Washington (UW) currently conducts isolation and pointing research with a type of isolation mount developed in cooperation with Hood Technology Corp., similar to that at the Jet Propulsion Laboratory (JPL). This device is referred to as a "hexapod" because it incorporates six spring-mass damper struts that can be actively controlled. Until the spring of 1999, the base plate of the UW hexapod sat on a foam pad, while the top plate was suspended from the laboratory ceiling with three long springs. Figure 1.1 shows the first generation hexapod test-bed setup. All isolation and pointing research was accomplished by exciting the base plate with large shakers. While knowledge gained from past hexapod research at the UW is indeed useful, more insightful results could be found by conducting experiments on a test-bed that actually mimics the dynamics and

disturbances of a typical spacecraft. This thesis describes new science and commercial missions that will incorporate vibration isolation technology, but it focuses on the design, analysis, fabrication, and model development of a spacecraft test-bed for use with the UW hexapod.

## 1.2 Previous work

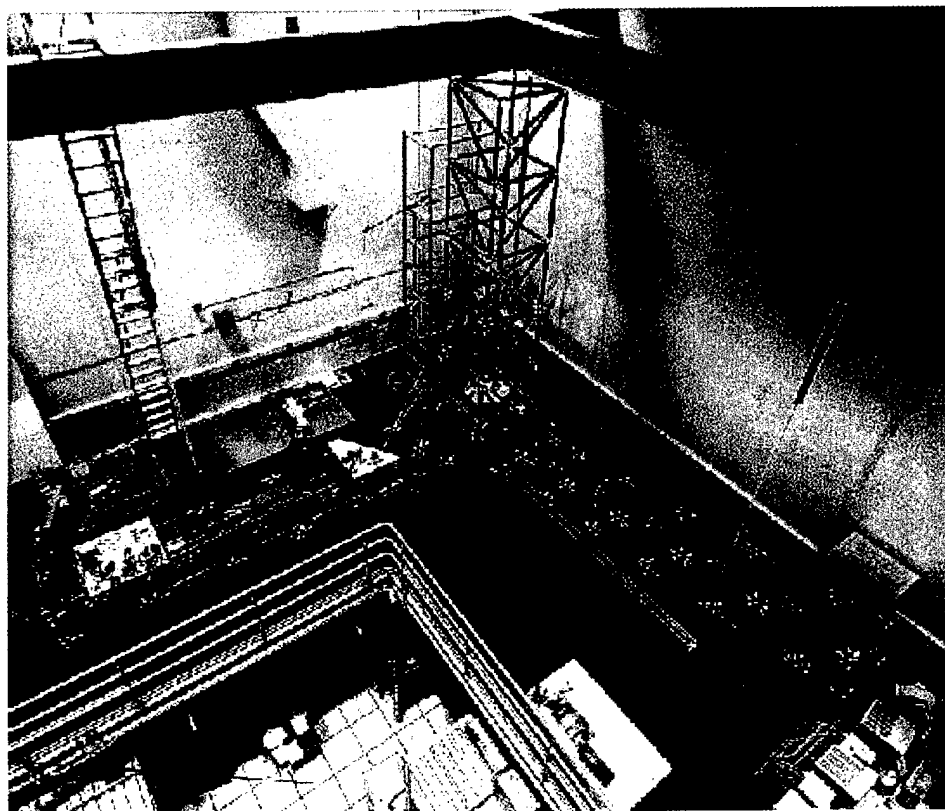


Figure 1.2: Bird's eye view of the Micro Precision Interferometer test-bed.

Test-beds for isolation and pointing devices have been constructed in the past. In 1993, JPL built the Micro Precision Interferometer test-bed, shown in Figure 1.2, as a full-scale model of a future space-based interferometer, containing all of the systems necessary for astrometric measurement [11]. It was designed specifically to incorporate six-axis vibration isolation, structural quieting, and other technologies needed for space interferometry missions. All the subsystems are contained on a 7m x 7m x 6.5m softly suspended truss structure. Researchers at JPL use the test-bed as to provide a realistic end-to-end problem to evaluate and integrate new interferometer technologies [12].



Honeywell Space Systems constructed a similar test-bed to demonstrate vibration isolation and pointing technology's importance for laser communication systems. The Honeywell Satellite Control test-bed, shown in Figure 1.3, is set up to evaluate passive, active, and hybrid vibration isolation devices for on orbit disturbance reduction. The goal is to use a six-axis active vibration isolation device to reduce the disturbances on the structural bus that cause the payload to jitter. Honeywell's efforts are driven by the competitive communication satellite market, where controlling structural vibrations over the 15 year life of a communications satellite is imperative to commercial success [8].

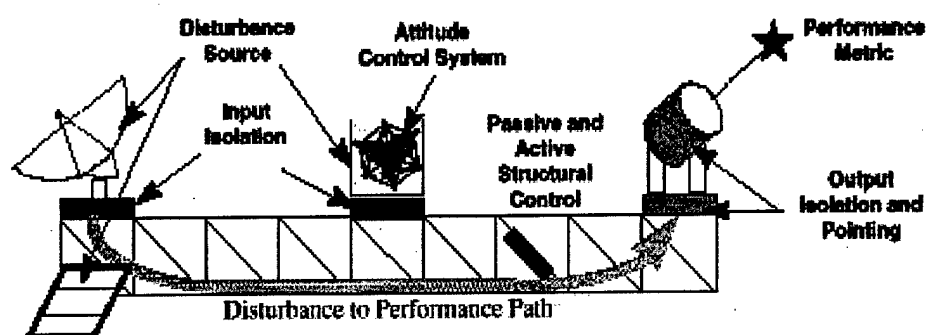


Figure 1.3: Topography of the Honeywell Satellite Test-bed [8].

The two test-beds discussed above are very large in comparison to the one built for the UW Hexapod. Even so, ideas from these test-beds are incorporated into the smaller scale UW design. These include the aluminum tubes, plates, and nodes that serve as the foundation for attaching solar arrays, drive motors, fuel tanks, electromagnetic shaker motors, and the UW Hexapod. Like the JPL and Honeywell designs, the next generation UW test-bed is suspended from the ceiling by soft springs to simulate a free-free boundary condition environment so that experiments can be conducted in a simulated 0-g environment.

### 1.3 Organization

Chapter 2 presents background information on several future space systems that will incorporate six axis isolation and steering devices. Chapter 3 details the design and construction of the satellite/hexapod test-bed. Chapter 4 presents the details of a finite element model of the satellite test-bed structure, and shows how it was converted from an ANSYS database to an input-output state-space model in MATLAB. Chapter 5 describes

the electronic hardware used to conduct modal analysis on the structure and also includes the results of the experimental modal analysis. Transfer functions from the model are overlaid on the experimental data in Chapter 5. Chapter 6 presents a model updating procedure used to improve the accuracy of the finite element model and shows the results of the procedure. The final chapter presents conclusions and summarizes recommendations for future work on the satellite test-bed.

## Chapter 2: Background Information

### 2.1 Future Systems Overview

The next decade's space telescopes, communication spacecraft, and remote sensing spacecraft will require active isolation devices with fine pointing capability to be successful. This is true because spacecraft bus structures often house noisy components such as reaction wheels, fluid pumps, solar array drives, fuel tanks, and other machinery that transmit vibration to sensitive payloads. Active vibration isolation and pointing mounts aid in meeting specified pointing requirements by attenuating disturbances before they reach the payload. Specifically, separated space telescopes called interferometers will depend on active isolation and pointing devices to steer mirrors, lasers, and other optics as well as separate them from the noisy spacecraft main bus. Constellations of communication satellites will depend on active isolation and pointing devices to accurately point lasers to establish high data-rate optical intersatellite links throughout the constellation. Finally, many remote-sensing missions will require stable and precisely controlled platforms for cameras, while others will depend on extremely accurate formation flight to achieve mission goals. In each case, active isolation and pointing devices will help insure the success of these missions by cushioning and pointing sensitive payloads. This chapter specifically addresses the need for vibration isolation devices in future space telescopes and communication satellites. It briefly describes vibration isolation in Earth observation missions and then summarizes the pointing requirements levied on the specific systems in tabular format.

### 2.2 Interferometry

Space based interferometry represents mankind's next step toward fully understanding the origins of our solar system and universe. In order to accomplish the feat of finding and studying Earth-like planets around nearby stars, astronomers must take advantage of the increased resolution offered by interferometers which are free of the Earth's atmosphere [6]. NASA's *Origins* program is one such investigative venture that incorporates interferometry in missions to explore the universe. One *Origins* goal is

to discover how galaxies and solar systems form. Another is to discover other inhabitable planets outside the solar system, and ultimately take images of these planets [6].

The *Origins* program consists of three generations of spacecraft. The first generation includes Space Technology 3 (ST3), the Space Interferometry Mission (SIM), and the Next Generation Space Telescope (NGST) [6]. The ST3 and SIM missions are both optical interferometers, and the NGST mission is a larger version of the Hubble Space Telescope. All should be operational by 2008. *Origin's* second generation consists of a single spacecraft called the Terrestrial Planet Finder (TPF). The TPF is an infrared interferometer designed to detect Earth-size planets outside the solar system that possess an Earth-like atmosphere [6]. The TPF is tentatively scheduled for launch in 2011. The third generation of *Origins* is the Planet Imager (PI). Like the Planet Finder, it is an infrared interferometer that ambitiously combines several TPF-type spacecraft flying in formation [6]. The Planet Imager is little more than a vision at this point because the advances in technology required to make the PI viable are so enormous [6].

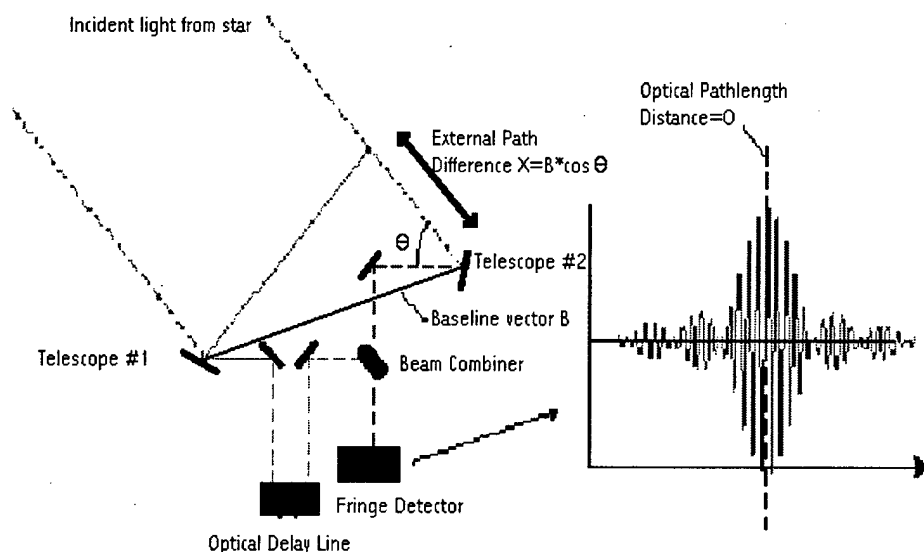


Figure 2.1: Interferometry Diagram [19].

To understand why active vibration isolation is a necessity in space telescope missions, one must first understand interferometry. Spaceborne optical interferometers employ two or more separated small telescopes to collect and project light from a single

target star to a "combiner" aperture. The distance between the "collector" telescopes is called a baseline. Increasing the baseline increases the interferometer's resolution much like increasing the diameter of a telescope lens increases a telescope's resolution.

Because the light from the star reaches one of the interferometer's collecting telescopes slightly before reaching the other, there is an external path difference between the two, as shown in Figure 2.1. If one knows the baseline distance and can measure the external path difference, then light from the two collectors can be combined with zero path difference by using an optical delay line. This combination, or interference, creates a fringe pattern from which star data can be extrapolated. Multiple baselines are imaged to create a type of "digital" picture of the star [19].

Measuring the external path difference is one key to interferometry. An interference pattern is formed at the collector aperture by combining the light beams collected from two small telescopes. From this interference pattern, the path difference can be measured. The system adjusts an internal optical delay line until it matches the external path difference, as shown in Figure 2.1. In order to detect when the internal optical delay line distance matches the external path difference, a sensor detects when the interference pattern is at maximum strength. With the external path difference and baseline knowledge, the angle  $\theta$  can then be computed. Astronomers use the angle  $\theta$  to determine the size of a star. Using the same technique, astronomers can also detect the telltale wobbling motions of a star, which are only present when a planet, possibly life sustaining, is close by [19].

Measuring the external path difference is a difficult task. For an interferometer to be effective, its structure must remain stable enough so that the internal optical path lengths can be controlled to 10nm or less [19]. A nanometer represents a distance equal to 10 times the diameter of a hydrogen atom. Thus, there is little tolerance for disturbance in the optical paths. Any significant vibration from reaction wheels, solar array drives, fluid slosh, or cryocooling devices can wreak havoc on the accuracy of an interferometer's metrology systems. NASA's two interferometry missions planned for the next decade both require active isolation technology to meet their stated goals.

### 2.2.1 Space Technology 3

NASA's first space interferometry mission is slated for launch in 2003. Space Technology 3, previously known as the New Millennium Interferometer and Deep Space 3, is the first mission in the first generation of the *Origins* program [6]. It has recently been re-designed to incorporate only two formation flying spacecraft. However, this chapter describes the old design architecture to introduce the need for vibration isolation and pointing devices in interferometry. The old design consists of a constellation of two light "collection" satellites and one light "combiner" satellite. The primary purpose of the mission is to demonstrate advanced technologies for future spacecraft and instruments. Most importantly, Space Technology 3 will demonstrate formation flight of multiple spacecraft and operate a space-based version of a Michelson Interferometer at long baselines [16]. The ST3 project will also validate many software and hardware components, which are similar to those to be used later in the Stellar Interferometry Mission [3]. Figure 2.2 shows the old ST3 constellation deployed in an Earth-trailing heliocentric orbit.

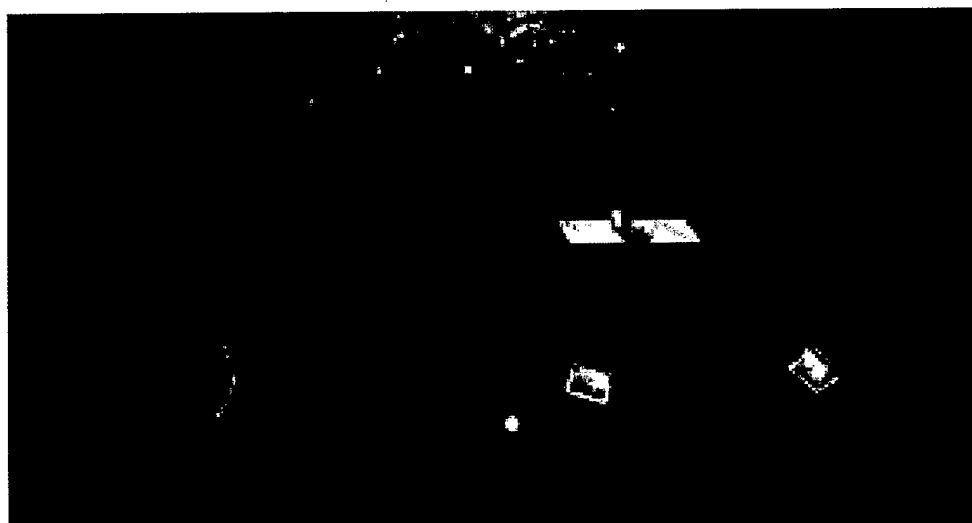


Figure 2.2: Old Space Technology 3 system deployed.

The requirements that ST3's subsystems must meet are extremely stringent. The trio of spacecraft must fly in an equilateral triangle formation at baselines of 100 m to 1 km in order to provide angular resolutions from 5 to 0.5 nanoradian, or equivalently 1 to 0.1 milliarcsec [3]. ST3 requires formation flying accuracy to  $\pm 0.01$  m relative distance

and  $\pm 0.3$  milliradian relative angle. It meets these requirements by using a sensor that incorporates Global Positioning System (GPS) technology—not the actual GPS constellation—and counter propagating lasers [3]. The combiner spacecraft uses two optical delay lines (ODL's) equipped with fast steering mirrors to direct the light beams from the two collector spacecraft to the combiner aperture. The ODL's allow 0.02 m in delay adjustability with 10 nanometer resolution [3]. The absence of a rigid truss structure to connect all the elements of the interferometer means that structural rigidity is actively achieved using a laser metrology system. The metrology lasers use the same mirrors as the collected starlight to measure inter-spacecraft distances to within 2 mm. Then the mechanical optical delay lines can perform a fringe interference search with 10 nm nanometer accuracy [3]. Obviously, nanometer resolution is not possible if sources of vibration push the pointing accuracy of the mirrors outside of these requirements.

The inclusion of active vibration isolation and pointing capability on ST3 depends on whether reaction wheels are a part of the attitude control system. Currently there is a debate as to whether ST3's attitude control system should use both reaction wheels and Pulsed Plasma Thrusters to control angular orientation. The constellation must use thrusters to maintain formation flight, while reaction wheels may be required to point the constellation in the required direction with high enough accuracy. Combined with the effects of the solar array drives and disturbances from thruster misalignment, the problems created by reaction wheel imbalances will substantiate the need for active vibration isolation. If ST3's designers choose to keep reaction wheels as part of the design, active vibration isolation will most likely be used in the final design in order to reduce vibration to achieve nanometer resolution in the optical delay line.

### **2.2.2 Stellar Interferometry Mission**

The Stellar Interferometry Mission (SIM) will be NASA's second space-based optical interferometer, but the first designed specifically for precision astrometry. SIM is designed as a 10m baseline Michelson interferometer operating in the visible waveband. Figure 2.3 shows an artist's concept of the SIM spacecraft. Unlike Space Technology 3, SIM is a single spacecraft that requires no formation flight capabilities. However, the

observational capabilities of SIM are much better than ST3, and two orders of magnitude better than the latest astrometry device Hipparchos, a satellite maintained by the European Space Agency [19]. In its narrow-angle astrometry mode, SIM will be able to measure differential positions between stars with 1-micro arcsecond ( $\mu\text{as}$ ) accuracy [19]. To visualize what 1- $\mu\text{as}$  resolution means, consider a person standing on the surface of Mars with a flashlight in one hand. If a telescope on Earth could detect when the person shifts the flashlight from one hand to another, it could measure position with 1- $\mu\text{as}$  accuracy [6].

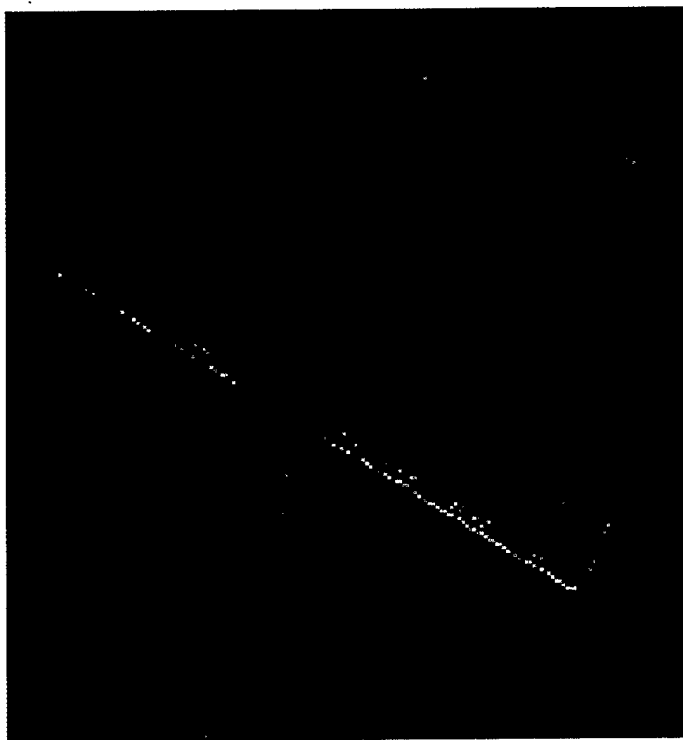


Figure 2.3: Stellar Interferometry Mission.

The Stellar Interferometry Mission faces many of the same problems as Space Technology 3. While SIM's short baseline of 10 m appears to simplify the metrology as compared to ST3's 100 m or 1 km baselines, SIM has three interferometers on board rather than one. Also, because SIM's measuring capabilities are so precise, the optical system's performance requirements are ten times more stringent than for ST3 [19]. Nanometer level stabilization and control of the optical path lengths in SIM's three interferometers is required in order to avoid blurring the interference fringe. Simulations



conducted at the Jet Propulsion Laboratory suggest that in the unattenuated spacecraft environment, the optical path length variation is a factor of 100 above the 10nm requirement [12]. The system must not only control the path lengths at the nanometer level, but also produce a measurement to subnanometer levels in order to achieve the desired astrometric accuracy. SIM's 10m baseline necessitates 50 picometer (pm) measurement capability to achieve 1- $\mu$ as accuracy [19]. A picometer is 1/100<sup>th</sup> of the diameter of a hydrogen atom.

The limited background information presented thus far on interferometry, Space Technology 3, and the Stellar Interferometry Mission, clearly indicates that a stable optical path is key to the success of space based interferometers. Jitter at the origin of the lasers in the metrology system or in the mirrors of the adjustable optical path lengths limits the accuracy of metrology and the quality of the resulting interference patterns. Active vibration isolation mounts can either separate disturbance sources, such as reaction wheels, from the main spacecraft bus, or separate a sensitive payload from a noisy bus. They also function as a mechanism that can precisely point the lasers, mirrors, or other optics required to achieve space borne interferometry. As a result, active vibration isolation devices are integral to the success of NASA's *Origins* program.

## 2.3 Space Communications

Space communication is another field where active vibration isolation technology is critical. The recent growth of large commercial constellations of Low Earth Orbit (LEO) communication satellites, such as Iridium, and the need for increased intersatellite link bandwidth, has led Teledesic, the next generation "Internet in the Sky" to baseline optical intersatellite links (OISL's) in its design. Integrating laser communication payloads with communication satellites drastically increases the precision pointing requirements of these spacecraft. As a result, disturbance vibration becomes a very important issue [8].

According to Teledesic Corporation's Vice President and Chief Scientist, "The Teledesic Network is a high-capacity broadband network that combines the global coverage and low latency of a LEO constellation of satellites with the flexibility of the

Internet and 'fiber-like' transmission quality [13]." The Teledesic constellation will orbit the Earth at an altitude of 1375 km. Twelve orbital planes--containing twenty-four satellites each--make up the 288 spacecraft in the constellation. In order to achieve the goal of "fiber-like" quality, Teledesic's satellites communicate with each other using laser intersatellite links to provide "internetting" of the constellation at bandwidths of over 4 Gbit/sec [8]. Major ground terminals act as an interface to both the satellite network and terrestrial end-users. Figure 2.4 shows how Teledesic would look from outside the constellation. The individual orbits are offset by several kilometers in altitude so that there is minimal chance for collision as the satellites cross over the North and South Poles.



Figure 2.4: Illustration of Teledesic Constellation.

Accurate beam positioning for Teledesic's intersatellite links is crucial for the laser communication system's capability of very high bit-rate data transfer with low error. Unfortunately, laser communication is adversely affected by satellite jitter, which usually is of little concern in radio or microwave communication systems. Low amplitude spacecraft vibration, or jitter, causes very small angular displacements of the source laser. Small displacements at the source laser develop large beam position errors at the end terminal when amplified by the thousands of kilometers between satellites [15]. In the Teledesic network, each satellite may be connected via intersatellite link with up to

eight other satellites in the same or adjacent orbiting planes. Distance between communicating satellites or nodes might range from 800 km to many thousands of km depending upon the final altitude picked for the constellation [13]. In order to accommodate the vast distance between Teledesic's spacecrafts' small optical apertures, optical intersatellite links must point with microradian ( $\mu\text{rad}$ ) accuracy. This is a stark contrast with RF communication links, where the pointing performance is measured in fractions of a degree--an increase of roughly four orders of magnitude [8]. Specifically, estimates derived from testing at Honeywell Space Systems imply the need for  $2.3 \mu\text{rad}$  pointing accuracy with  $\pm 0.5 \mu\text{rad}$  error tolerance [8]. The pointing accuracy applies only to the laser communication system, and not necessarily to the entire spacecraft.

Vibration isolation devices with fine pointing capabilities can help solve the problem spacecraft jitter creates for laser-communication systems. A lasercom terminal design that incorporates vibration isolation with the capability for fine beam steering can meet the sub- $\mu\text{rad}$  pointing error requirement Teledesic's terminals demand [8]. The low-pass filter characteristics of six-axis vibration isolation devices attenuate the high frequency disturbances created by reaction wheel imbalances, fluid slosh, or other mechanical disturbances. By coupling vibration attenuation with the fine-pointing capabilities of current six-axis isolators, designers create a very effective platform for pointing lasers.

## **2.4 Other Applications**

Certainly there are other space applications where six axis vibration isolation and pointing devices help accomplish mission goals. Earth-observing satellites use the isolating capabilities of the hexapod for attenuating noise from the spacecraft bus as well as for fine pointing of optical or infrared cameras. A hexapod can also suppress narrow band disturbances on the payload side caused by a Cryo-cooler, collocated with an infrared camera in order to keep it cool. For example, the Ballistic Missile Defense Organization's Space Technology Research Vehicle (STRV) 2 utilizes a six-axis isolator to isolate and steer an experimental mid-wavelength infrared (MWIR) camera [17].

Many missions that incorporate constellations of spacecraft that fly in formation will also benefit from isolation technology. The constellations may determine their angular position using Kilometric Optical Gyroscopes (KOGs) [10]. KOGs use counter propagating laser beams to measure angular displacements of a satellite formation separated by long distances. Stability and control of the path length between satellites and the source lasers that make up the KOGs can only be achieved using a combination of isolation and active control. Many NASA separated spacecraft missions may incorporate this new technology. They include Earth orbiting imaging missions such as TOPSAT [10], the New Millennium EO-1 Landsat Co-Flyer [10], gravity mapping missions such as GRACE [10], deep space sparse-aperture RF telescopes like ALPHA [10], and others. Figure 2.5 illustrates conceptual versions of the Landsat EO-1 and ALPHA missions.

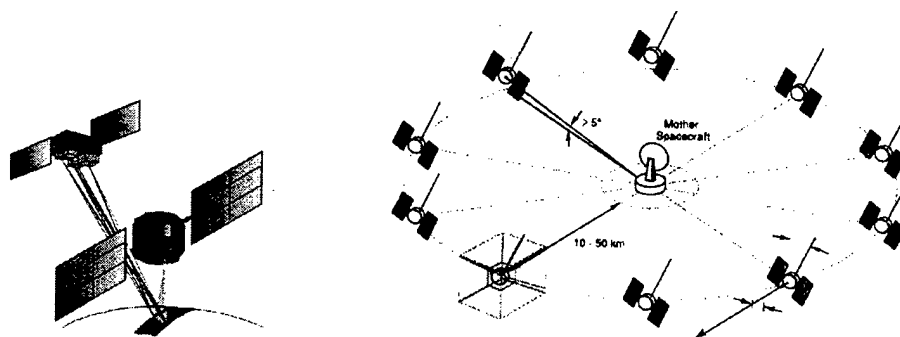


Figure 2.5: Illustration of the LandSat Co-Flyer (left) and ALPHA (right) missions [10].

## 2.5 Summary of Pointing and Control Requirements

Table 2.1 on the next page summarizes the most stringent pointing and measurement requirements for ST3, SIM, and Teledesic. The table also summarizes how vibration isolation and pointing devices can help designers meet the strict mission pointing requirements levied on these missions. The reader will notice that the function of the isolation and pointing device is nearly the same for each mission. Earth observing missions are not included in Table 2.1 because there is less specific information available for most of these missions.

Table 2.1: Summary of pointing and measurement requirements.

| Mission                        | Position Measurement Requirements  | Pointing Requirements   | How vibration isolation and pointing devices can help   |
|--------------------------------|--|---|---|
| Space Technology 3             | <ul style="list-style-type: none"> <li>• 10 nm control of optical path lengths</li> <li>• 1 nm measurement accuracy of optical path lengths</li> <li>• <math>\pm 0.01</math> m relative position of constellation</li> </ul> | <ul style="list-style-type: none"> <li>• milli-arcsec angular resolution when imaging objects</li> </ul>  | Fine pointing and disturbance attenuation <ul style="list-style-type: none"> <li>• Cushion an point mirrors and source lasers in the optical path lengths</li> <li>• Separate spacecraft from reaction wheels to attenuate disturbances in optical paths</li> </ul> |
| Stellar Interferometry Mission | <ul style="list-style-type: none"> <li>• 10 nm control of optical path lengths</li> <li>• 50 pm measurement accuracy of optical path lengths</li> </ul>  | <ul style="list-style-type: none"> <li>• 1 <math>\mu</math>as angular resolution when imaging objects</li> </ul>  | Fine pointing and disturbance attenuation <ul style="list-style-type: none"> <li>• Cushion and point mirrors and source lasers</li> <li>• Separate spacecraft from reaction wheels to attenuate disturbances in optical paths</li> </ul>                            |
| Teledesic                      | <ul style="list-style-type: none"> <li>• N/A</li> </ul>  | <ul style="list-style-type: none"> <li>• <math>\pm 0.5</math> <math>\mu</math>rad jitter error in laser com system</li> <li>• 2.3 <math>\mu</math>rad overall accuracy for lasercom system</li> </ul> | Disturbance attenuation and fine pointing <ul style="list-style-type: none"> <li>• Separate source lasers from spacecraft bus</li> <li>• Pointing control for source lasers</li> </ul>  |

## Chapter 3: Test-Bed Design

This chapter briefly describes the configuration of the UW Hexapod as well as how it works. The chapter also describes the first generation hexapod test-bed and outlines the problems associated with it. Additionally, it contains a presentation of the second generation test-bed, including the design of the main truss structure, the solar arrays and drive mechanism, and the overhead suspension system.

### 3.1 UW Hexapod

While this thesis primarily addresses the design, construction, and analysis of a spacecraft test bed for use with the UW hexapod, it is important that the reader understand how the hexapod works. The University of Washington Control System Laboratory teamed with A. Von Flotow and Hood Technology to design and build an improved hexapod [18]. The completed UW hexapod is shown below in Figure 3.1. The top and bottom plates are steel and the mounts for the struts are all aluminum. The struts all form 90° angles with one another and allow for precise six degree-of-freedom control of the top plate's position.

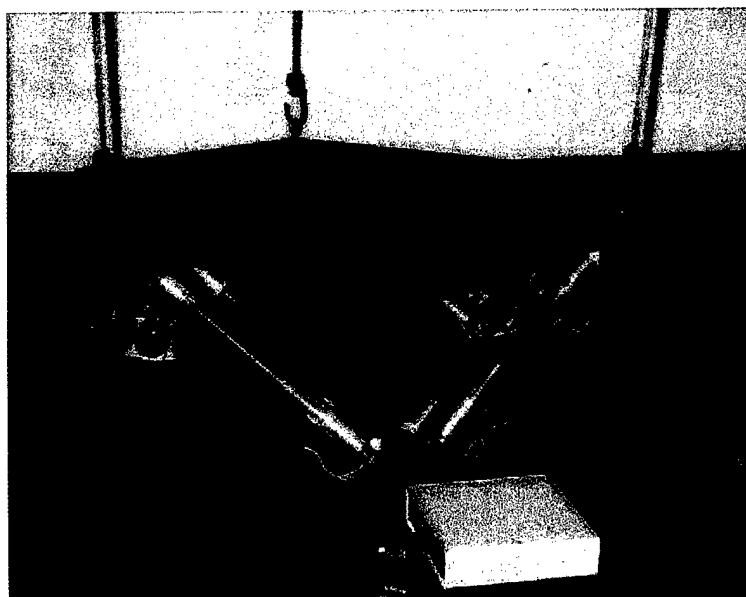


Figure 3.1: UW Hexapod configuration

The individual struts of the hexapod incorporate a number of sensors and actuators to explore active isolation and pointing architectures. Each strut has a three-axis load sensor, one Linear Variable Differential Transformer (LVDT) sensor, two velocity sensors at the top and bottom of each strut, and one voice coil actuator. Figure 3.2 shows a strut with the primary parts labeled. The primary and secondary flexures function as the passive isolation part of the device, while the voice coil and associated sensors give the hexapod vibration suppression and fine pointing capability. The system is coupled to an AC100/C40 Real time control system from Integrated Systems (ISI). The system uses a graphical interface to allow the user to control different inputs and outputs to the system. The user can directly input controllers for the system or import them from another program such as MATLAB [7].

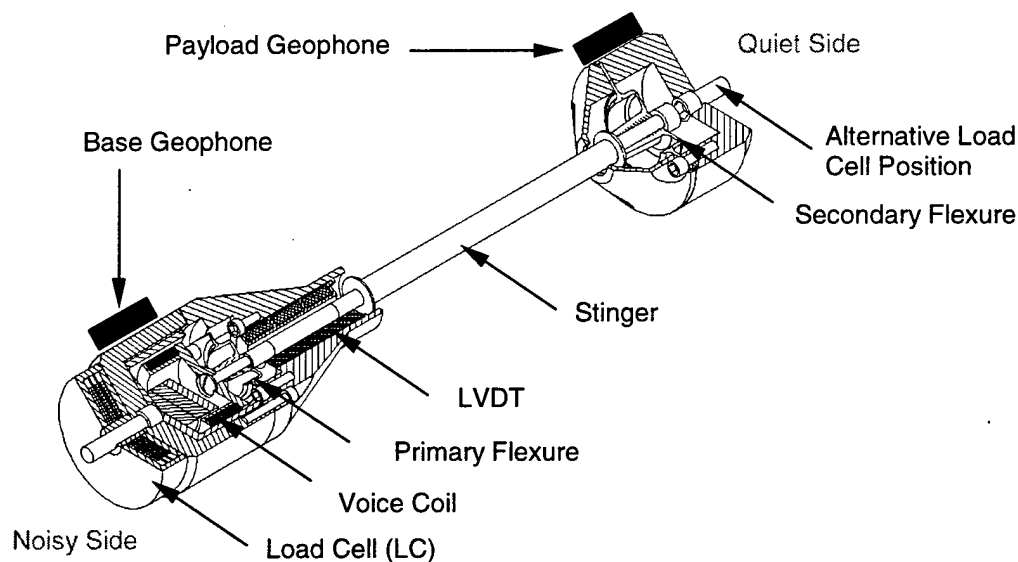


Figure 3.2: UW Hexapod strut design [7].

### 3.2 First Generation test-bed setup

The hexapod cannot support its own weight in a 1-g environment because of the use of very soft flexures to reduce the pass frequency. Thus, long metal springs with low stiffness were used to off-load the weight of the hexapod's top plate. The bottom plate was separated from the ground with a stiff foam pad. The foam pad gave the bottom plate near-rigid behavior, but still allowed for disturbance inputs from large shakers. The primary advantage of the first generation test-bed setup was simplicity and ease in

applying disturbances. By moving shakers to different positions around the base plate, the system could be excited in different degrees of freedom.

The primary disadvantage of the first test-bed is that the near-rigid characteristic of the hexapod's bottom plate is not representative of a real spacecraft structure, where free-free boundary conditions are usually present. Also, the foam pad under the bottom plate introduced non-linearities into the system, presenting difficult problems when trying to model the system based on linear methods. Finally, building vibrations and other unwanted disturbances were easily transmitted from the ground to the hexapod base plate. The objective of this work is to design and construct a new test-bed where the hexapod rests on top of a model spacecraft completely suspended from the ceiling, thus addressing many of these shortcomings.

### 3.3 Second Generation Test-Bed Design and Construction

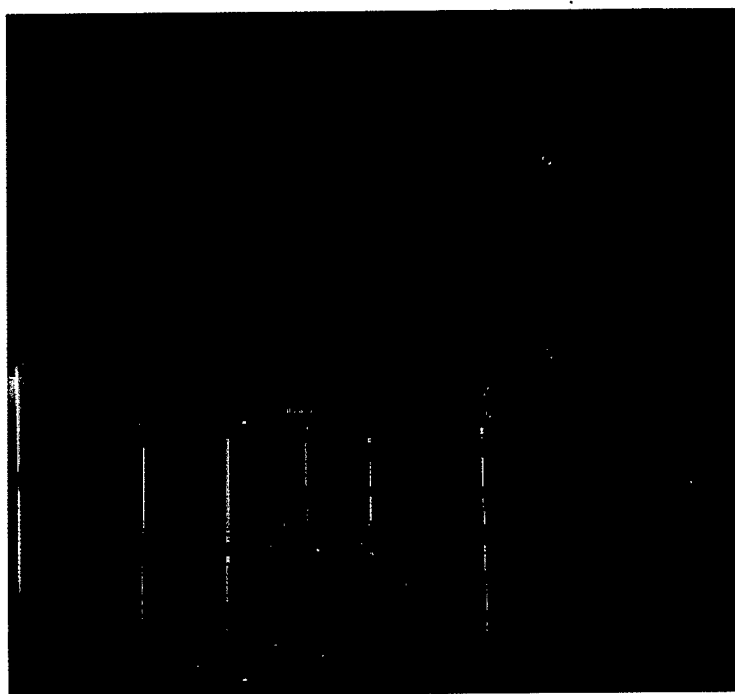


Figure 3.3: The second generation test-bed (including the hexapod) suspended from the overhead truss. Note that the long springs are made up of several short springs connected in series.

While the second generation test-bed is not designed for use in space, the structure incorporates many major space design considerations to make the system



realistic. The main truss structure's first fundamental frequency is deliberately designed to be above the published vibration load data for all launch vehicles. The model solar arrays have enough area to produce power for a medium sized spacecraft; they can rotate 360°; and they capture the low frequency dynamic characteristics of real space arrays. The structure also has the capability to accept small fuel tanks to simulate fluid slosh and small electromagnetic shakers to simulate reaction wheel disturbances. Finally and maybe most importantly, the test bed is completely suspended from the ceiling to offload gravity. The following sections of this chapter detail the design of specific components of the test bed, including the main truss, solar arrays, solar array drive, and the suspension system.

### 3.3.1 Main Truss Structure

The main structure of a real spacecraft must meet specific strength and stiffness requirements, usually driven by the launch environment. In general, the vibration environment experienced during launch translates into a need for a stiff main structure. Mechanical vibration from the launch system's engines and acoustic vibration transmits to the payload through the payload interface or through the launch shroud for the duration of the flight. Table 3.1 lists the first fundamental frequencies for common launch systems. A spacecraft structure must be stiff enough such that it does not couple with the fundamental frequency the launch vehicle excites, which would create large vibrations near resonance. The main truss of the test-bed structure was designed to have a first fundamental frequency above 50Hz to observe this important design consideration.

Table 3.1: Fundamental frequencies for typical launch systems [9].

| Launch System   | Fundamental Frequency (Hz) |         |
|-----------------|----------------------------|---------|
|                 | Axial                      | Lateral |
| Atlas II, IIA   | 15                         | 10      |
| Ariane 4        | 18                         | 10      |
| Delta 6925/7925 | 35                         | 15      |
| Long March 2E   | 26                         | 10      |
| Pegasus         | 18                         | 18      |
| Proton          | 30                         | 15      |
| Scout           | 18                         | 20      |
| Space Shuttle   | 13                         | 13      |
| Titan II        | 24                         | 10      |

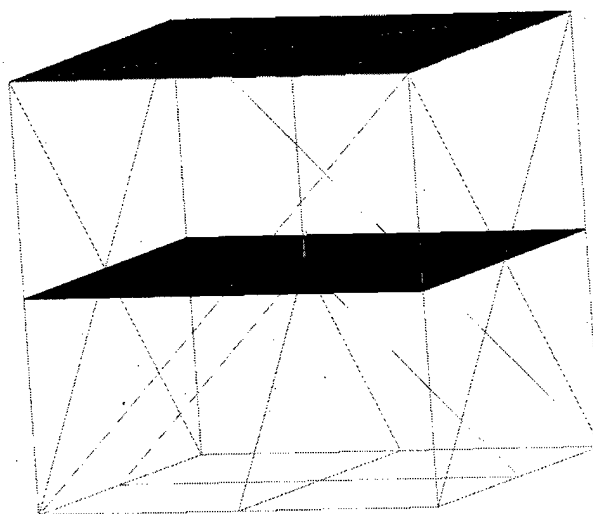


Figure 3.4: Final design of the test-bed main truss.

The final configuration of aluminum nodes, tubes, and plates for the truss is the product of an iterative finite element analysis. Using a simple finite element model in the program *Visual Analysis* [21], a civil engineering finite element modeling code, several potential configurations were investigated. All potential configurations fit within a 1m cube. The goal was to minimize the number of nodes and tubes needed to set the first fundamental frequency above 50 Hz. The parameters varied in the analysis include the diameter and wall thickness of the truss's aluminum tubes, the thickness of the middle and top plates, and the number and placement of tubes in the truss. Figure 3.4 shows the final iteration of the main truss structure model, converted from *Visual Analysis* to an ANSYS database. Once a design converged that met the 50Hz stiffness requirement and was small in mass, the iteration was complete. The final model helped determine the amount of material to purchase from MERO Structures Inc., a supplier of aluminum tubes and nodes designed specifically for the construction of civil space trusses. The volume of the FEM was constrained to be  $1 \text{ m}^3$  for two reasons. First, MERO Structures offers standard size truss members in 0.5m, 0.707m, and 1.0m lengths. Using these three lengths allows for a lot of combination flexibility without the need for special-order parts. JPL's initial size estimate for the ST3 collector spacecraft was  $1 \text{ m}^3$ , so this was another reason to limit the volume of the test-bed. The following is a description of the finite element model setup used for this initial study.

The FEM consists entirely of PIPE16, SHELL63, and MASS21 elements, which are standard elements offered in the commercial ANSYS code [1]. All of the elements were assigned the same material properties, namely:  $E=72\text{e}9\text{Gpa}$ ,  $\rho=2800\text{kg/m}^3$ , and  $\nu=0.33$ . The truss members were modeled with PIPE16 elements, each approximately 10cm in length. The PIPE16 element is based on Euler beam theory, and allows the user to input an outer diameter and wall thickness to define the cross section of the beam, rather than  $I_{yy}$  and  $I_{zz}$  (see Chapter 4 for a more detailed description of the elements referenced in this section). Two options for the pipe cross section were available from MERO Structures: 22mm diameter x 1.0mm wall or 30mm diameter x 1.5mm wall. Only these two options were investigated in the FEM. The plates were modeled with SHELL63 elements, each approximately 10cm square. The SHELL63 element requires only that a thickness be defined at each of the 4 nodes. The thickness of each plate could be set to any value during the iterations. Thick solid aluminum plates are atypical in space design but needed here to help support the weight of the steel hexapod base plate. MASS21 elements were used to add mass at the connections. A specified mass value is added to the finite element nodes meshed with this type of element. Since MERO Structures offers only 1 type of aluminum node, weighing 0.08 kg, the mass of these elements remained constant throughout the iteration process. Table 3.2 summarizes the characteristics of the elements used, the part of the structure the elements modeled, and the number of each type of element used in the analysis. The number of elements shown in the table is based on the final iteration. Different configurations required more PIPE16 and MASS21 elements than other configurations, because different numbers of truss members were used in the iteration process.

Table 3.2: Summary of the elements used to model the main truss structure.

| Type of Element | Degrees of Freedom<br>(# of nodes)  | What the element<br>modeled | # of elements used. |
|-----------------|-------------------------------------|-----------------------------|---------------------|
| PIPE16          | Ux, Uy, Uz, Rotx, Roty,<br>Rotz (2) | Truss members               | 230                 |
| SHELL63         | Ux, Uy, Uz, Rotx, Roty,<br>Rotz (4) | Middle and Top<br>Plates    | 200                 |
| MASS21          | Ux, Uy, Uz<br>(1)                   | Connection nodes            | 23                  |

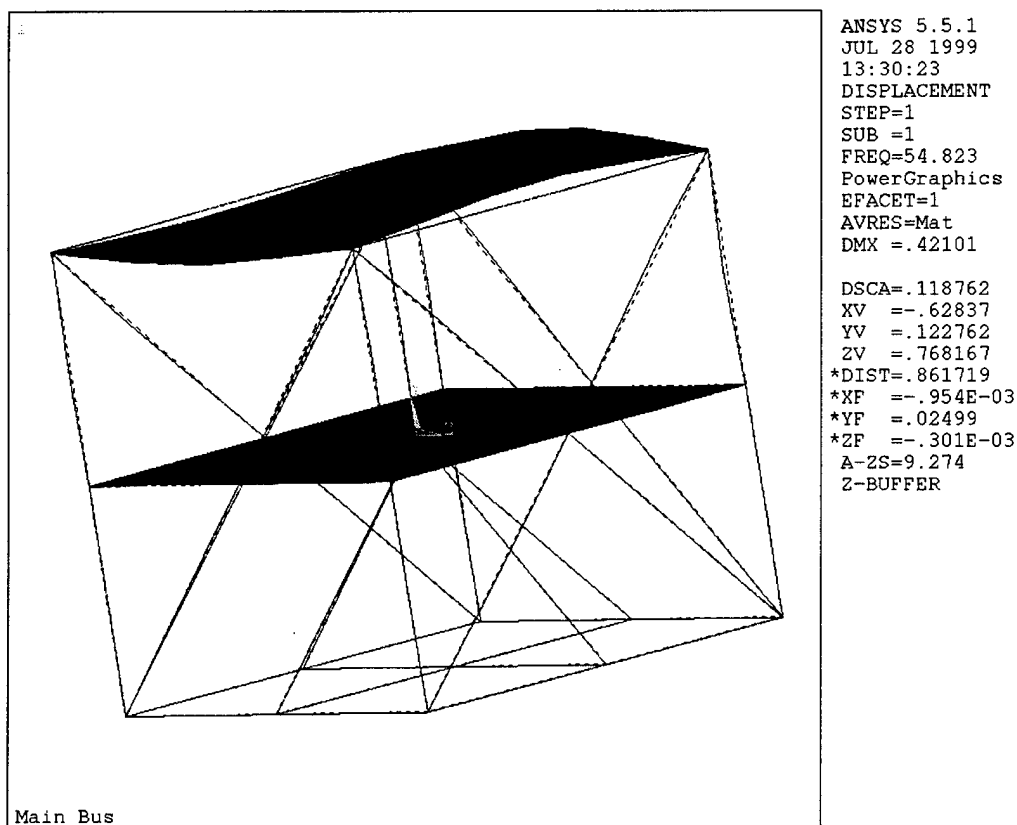


Figure 3.5: First mode shape of main truss. The only meaningful output in the legend to the right of the figure follows the word FREQ. This is the frequency of the first mode.

Results from both ANSYS and *Visual Analysis* indicate that the first natural frequency of the structure shown in Figure 3.5 is approximately 55 Hz. Figure 3.5 shows the ANSYS output for the first mode shape. The dotted lines in Figure 3.5 show the non-deformed shape of the truss superimposed on the deformed shape. The figure shows that the first mode is dominated by the dynamics of the heavy aluminum plate on the top of the structure. Because modeling joints plays such an important role in the FEM process, it is important to note how the plates are connected to the main truss. The plates are attached to the structure in the FEM at major node intersections. The middle plate is attached at 9 points, and the top plate is only attached at 5 points. Figure 3.6 shows that the dimensions of the two plates are equal in the finite element model. The figure also shows where the plates attach to the truss structure in the FEM. The middle attachment in each plate stiffens the plate considerably.

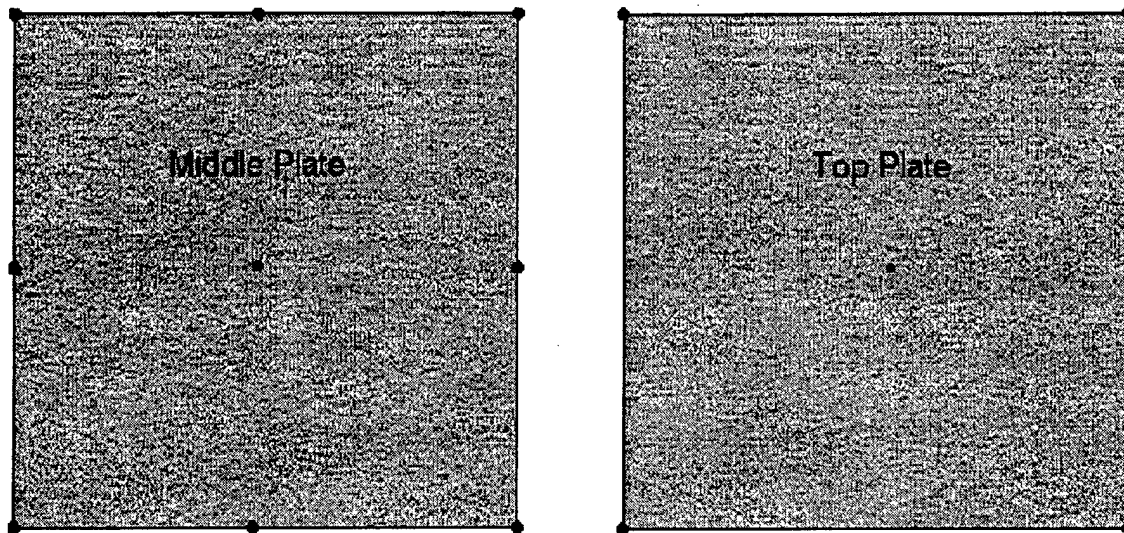


Figure 3.6: Top view of the two structural aluminum plates. The black dots correspond to connection points between plate and truss in the model.

The as-built final test-bed truss is very simple, and it is in part derived from information obtained from engineers working on preliminary models of ST3's collector spacecraft at the JPL. The size of the structure coincides with the JPL estimates of ST3's size: a 1.0-meter cube truss. Twenty-two 0.5m tubes, twenty 0.707m tubes, and four 1.0m tubes are the members that make up the truss. The tubes have a 30mm diameter with 1.5mm wall thickness. The tubes connect at 23 nodes. Each node has 18 threaded holes at 45° angles. There is a 0.95m x 0.95m x 5.6mm middle aluminum plate that supports the solar arrays, solar array drive, and fuel tanks. Another aluminum plate, 1.03m x 1.03m x 7.62mm thick, sits on the top of the structure to provide a platform for the hexapod bottom plate.

There is one major discrepancy between the design model and the physical structure. The middle connection of the top plate to the main truss shown in Figure 3.6 could not be made, because it interferes with the base plate of the hexapod. As a result, the final physical structure is much different than the final FEM design. A single connection in the middle significantly stiffens the top plate in the design FEM. However, the plate in the real structure will behave like a simply supported single large plate, with a much lower first fundamental frequency. This configuration does not meet the 50 Hz first fundamental frequency goal. However, since the test-bed will not have to survive a

launch sequence, it is more efficient to accept the available configuration than to modify the base plate of the hexapod to allow for a connection bolt in the center.

### 3.3.2 Solar Array Structure

Solar arrays provide a spacecraft with power needed to operate all of the electronic systems on board. The arrays are typically large in order to generate as much power as possible and are thus stowed until after launch. As such, they usually couple into the system at a very low fundamental frequency. On most spacecraft, the arrays must also rotate in order to stay perpendicular to the incident sunlight for highest efficiency. Another factor to consider is that over a period of ten years, the general efficiency of common solar cells deteriorates from about 15% to 8% [14]. This deterioration forces engineers to design arrays that generate more power (larger area) than required at the beginning of the spacecraft's life to meet the end-of-life requirements. There are some spacecraft that have arrays with many square meters of area and a first fundamental frequency as low as 0.5Hz in order to achieve power requirements. The test-bed arrays are based on the preliminary model of ST3 constructed at the JPL. Each array has an area of  $1.25 \text{ m}^2$  and rotates in synchrony with the other array. The fundamental frequency for the arrays is 6-10Hz in the JPL model. The goal of the test-bed array design was to achieve a first fundamental frequency of approximately 6-10Hz.

Finite element analysis also aided in the design of the solar arrays. It was known that square aluminum tubing would be used to construct the model arrays because of tubing's low cost. Some of the variables that could be changed in the design included the size of the tubing cross section, wall thickness, length and width of the array, and number of members to use. These parameters were easily varied after creating a model with the software tool *Visual Analysis* [21]. Each model in the design process was constructed with beam elements approximately 15cm long. Normally this meant that each long beam would be meshed with at least 5 elements, enough to easily estimate the first mode. A rigid constraint was attached to one end of the model to simulate attachment to the main spacecraft.

The final design is a result of many design iterations and is quite simple as well as easy to construct. It consists of 7 beams of 1-inch square aluminum tubing. The tubing has 1.4mm (0.055") wall thickness. Figure 3.7 shows the configuration of the solar arrays as well as the first mode shape of the array. The first array mode is approximately 8.5Hz according to both ANSYS and *Visual Analysis*.

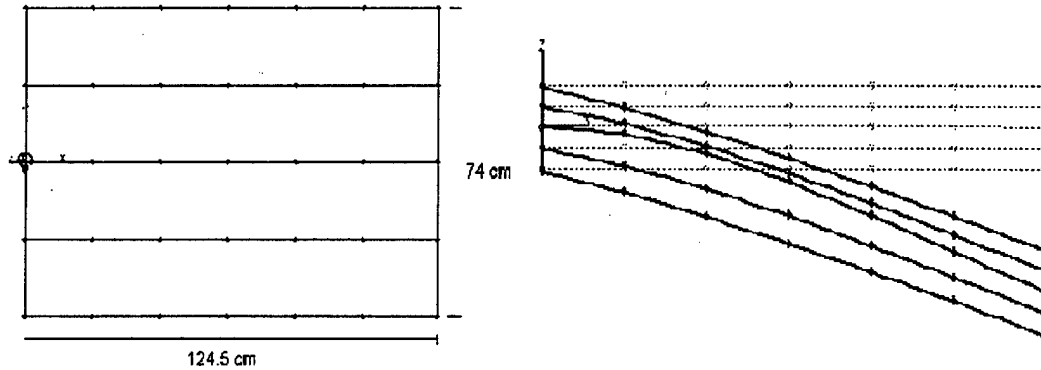


Figure 3.7: Solar array configuration (left) and first modeshape (right).

The accuracy of the FEA solution for the solar array is easily verified using a formula for the first bending mode of a beam with a concentrated mass on its end. The formula can be found in Blevin's text [2].

$$f_{array} = \frac{1}{2\pi} \left[ \frac{3EI}{L^3 (M + 0.24M_b)} \right]^{\frac{1}{2}} \quad (3.1)$$

In Equation 3.1,  $E$  is the modulus of elasticity,  $I$  is the moment of inertia for the entire array,  $L$  is the length of the array,  $M$  is the mass of the array,  $M_b$  is the concentrated mass of the vertical beam furthest from the spacecraft truss, and  $f$  is the natural frequency in Hz. The array is approximated as a single beam, where all of the moments of inertia along the axis with the least inertia are summed for the five 1-inch tubes. The point where the array attaches to the spacecraft is fixed, and the lateral beam at the end of the array is approximated with a single mass. The equation shows that the array's first natural frequency should be 8.65Hz.

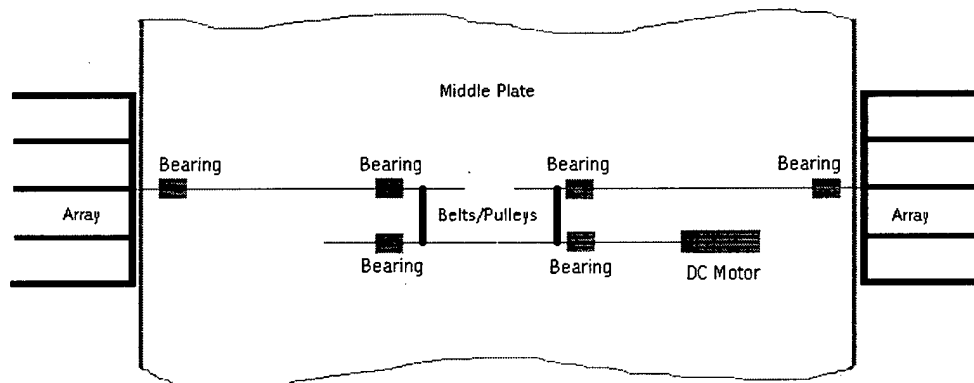


Figure 3.8: Top view, solar array drive mechanism.

Figure 3.8 shows a top view of the solar array drive mechanism. The solar arrays can rotate in either direction to simulate articulating space arrays. They are driven with a small 12-volt DC motor at a maximum of 12 revolutions per minute. A single drive shaft supported by two linear bearings is coupled to the array shafts with rubber belts and pulleys. The shafts are all made of hardened steel so that they can rotate in the linear bearings, and they have a  $\frac{1}{4}$  inch hole tapped in one end so that the arrays can be easily attached. The mass moment of inertia of each array is  $0.062\text{kg}\cdot\text{m}^2$ . The motor can supply a maximum  $0.7\text{ N}\cdot\text{m}$  (100 oz-in) of torque which translates into maximum acceleration of  $11.4\text{ rad/s}$  for the arrays. Clearly a stepper motor is more appropriate for a space design, but the DC motor is cheap and can provide a similar command/disturbance input when turned on for a brief period. Shaft collars prevent the solar array assemblies from slipping out of the bearings.

### 3.3.3 Suspension System

A major goal for the spacecraft test-bed was to allow the system to move in any direction with as much freedom as possible, so small disturbances can be measured anywhere on the structure. Any attachments to ground inhibit rigid body translation and rotation, thus preventing 0-g simulation; and should be minimized as much as possible. This goal is accomplished using a spring and damper suspension system to off-load gravity's acceleration from the test-bed. A stiff overhead truss, anchored to the walls of the laboratory, supports the suspension system. Ideally the suspension system's fundamental frequencies should be low enough to avoid interfering with the test-bed



modes of interest. Most texts recommend that the suspension modes be 10 times lower than the flexible modes of interest on the structure [5].

The truss that supports the test-bed's weight is made of steel angles and wooden 4x4's. The 4x4's are anchored to the walls of the laboratory, and each angle rests on top of a pair of 4x4's. A simple finite element analysis shows the deformed shape of the truss system's first mode at 22Hz. This analysis does not include the springs of the suspension system, but only the overhead truss with the load of the test-bed applied. Figure 3.9 shows the applied load case as well as the deformed shape. The black arrows on the left figure indicate boundary conditions and the applied loads resulting from the spacecraft test-bed. The dotted line in the figure to the right represents the non-deformed shape. The weight of the entire suspended system is nearly 300lb. The nodes on the 4x4's correspond to where the beams are bolted to the walls of the laboratory, and are assigned fixed boundary conditions. Unfortunately, at 22Hz, the first mode of the overhead truss is much lower than desired (100Hz would be better). However, the soft suspension system that separates the overhead truss from the test-bed prevents disturbances that excite the test-bed from exciting the overhead truss's modes of vibration. Experimental modal analysis verified this fact.

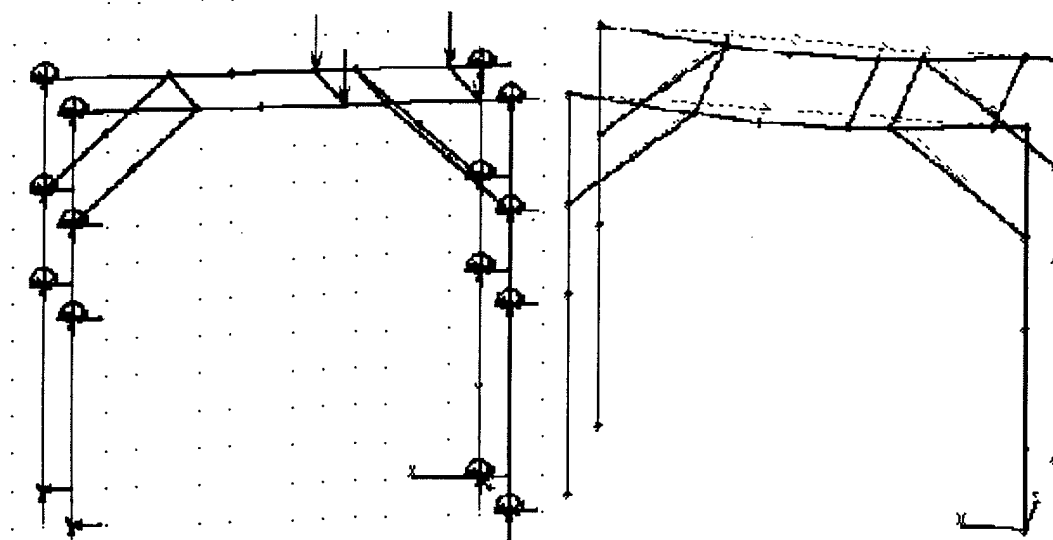


Figure 3.9: Suspension truss load case (left) and first mode shape at 22Hz (right).

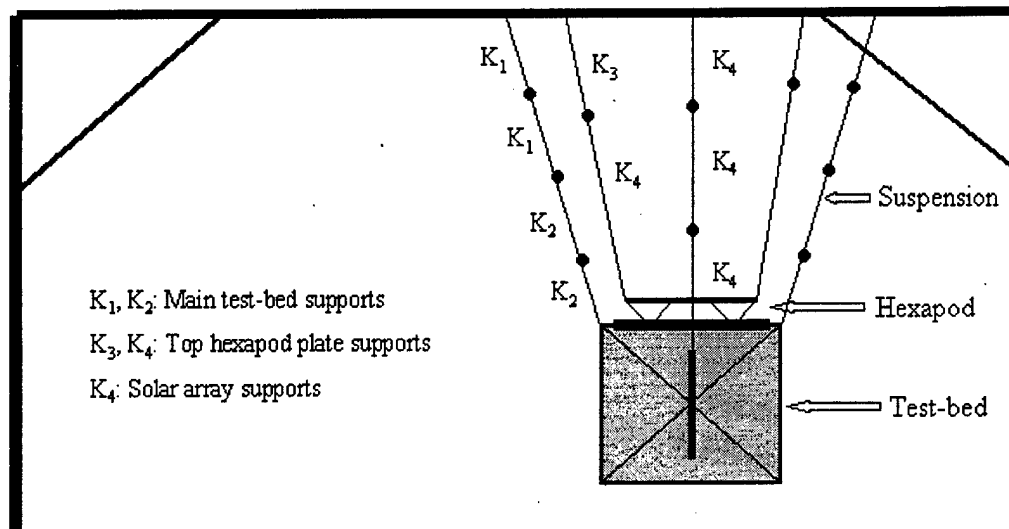


Figure 3.10: This is a side view of the test-bed suspended from the overhead truss. The different K subscripts indicate the different types of springs used. The nodes break up the lines to show how many short springs make up the system.

The test-bed is suspended from the overhead truss with a system of springs as shown in Figure 3.10. The main test-bed body and the hexapod top plate are both supported at four points. Springs also attach at the outer most point of the solar arrays to prevent them from sagging more than the rest of the test-bed. While the overhead truss's ceiling-hugging design keeps it out of the way inside the laboratory, it also allows the suspension system to have a very low bounce frequency—important for simulating 0-g. Low stiffness springs make use of the entire height of the room to get the lowest bounce and pendulum frequencies possible. The main body of the test bed weighs approximately 260lbs, and the top plate of the hexapod weighs approximately 40lbs. Table 3.3 shows how the springs selected for the final design deform under the weight of the structure.

Table 3.3: Spring deformation, spring constants, and bounce frequencies for each support.

| Spring Type                      | Unstretched Length | Stretched Length | Mass Supported | Spring Constant | Bounce Freq. |
|----------------------------------|--------------------|------------------|----------------|-----------------|--------------|
| Main Test-Bed Structure Supports | 1.36 m             | 1.95 m           | 29.5 kg        | 491 N-m         | 0.65 Hz      |
| Top Hexapod Plate Supports       | 0.74 m             | 1.78 m           | 4.5 kg         | 43 N-m          | 0.49 Hz      |
| Solar Array Supports             | 1.33 m             | 2.2 m            | 1.9 kg         | 21.4 N-m        | 0.53 Hz      |

The long springs that make up the suspension system are actually combinations of several smaller springs in series as indicated in Figure 3.10. The spring constants shown in Table 3.3 refer to the spring constant of the long springs rather than the individual ones that make up the series. Four small springs in series make up each of the main test-bed supports, two in series make up each hexapod top plate support, and three in series make up each solar array support. At each support point, a spring scale was inserted into the load path to determine how much weight the support carries. The "mass supported" column in Table 3.3 reflects the values measured by the spring scale. The total stiffness of each long spring support can be calculated using equation 3.2, which governs springs combined in series.

$$\frac{1}{K_{\text{series combination}}} = \frac{1}{K_1} + \frac{1}{K_2} + \frac{1}{K_3} + \dots \quad (3.2)$$

where  $K_1$ ,  $K_2$ , and  $K_3$  are the spring constants for the individual springs combined in series. The spring constant  $K_{\text{series}}$  is used in equation 3.3 to determine the bounce frequency for each of the test-bed supports.

$$f_{\text{bounce}} = \frac{1}{2\pi} \sqrt{\frac{K_{\text{series combination}}}{M}} \quad (3.3)$$

Table 3.3 also summarizes the bounce frequencies for each part of the suspension system. Equation 3.4 calculates the pendulum frequency for the entire system.

$$f_{\text{pend}} = \frac{1}{2\pi} \sqrt{\frac{g}{L}} \quad (3.4)$$

The distance ( $L$ ) from the middle of the test-bed to the overhead truss is approximately 2.25m. The pendulum frequency for the system is 0.35 Hz.

The suspension system is also extremely adjustable. Turnbuckles attach the suspension springs to the connection points on the main truss and the hexapod top plate. Each provides 2-4 inches of vertical adjustability. These adjustment points make it easier to line up the top plate of the hexapod with the bottom so that the struts can function

properly. The top plate suspension system can also translate in both horizontal directions of the plane parallel to the top plate, also simplifying the aligning process.

## **Chapter 4: Finite Element Model**

This chapter describes the tools used to construct a finite element model of the spacecraft test-bed structure. It describes the different types of elements used in the model, and shows the reader how physical properties are assigned to the elements. It also details how the FEM is set up to represent the physical test-bed structure. Several of the most important modes of the model are presented. These modes helped to identify modes of the physical system that are easily observed when the structure is excited at a particular frequency. Plots and descriptions of these modes are shown near the end of the chapter. The final two sections of this chapter describe the transfer of natural frequencies and modeshapes to MATLAB from ANSYS as well as the construction of an input-output state space system for the model. The FEM was converted from ANSYS to MATLAB so that the model could be validated with experimental data.

### **4.1 Objective and Tools Used**

The objective of the process discussed in this chapter is to capture the dynamics of the test-bed structure with a finite element model, and then validate that model using experimental data. ANSYS's modal analysis capability is used to extract the modeshapes and natural frequencies from the finite element model. Then the modeshapes and natural frequencies are used to create a state-space model in MATLAB. MATLAB is used to validate the model with experimental results, because it allows transfer functions from the model to overlay experimental data. Blevin's text [2] on natural frequencies and modeshapes was used as a tool to verify electronic analysis results with hand calculations in several cases. Note that the model described in this chapter excludes the hexapod. The hexapod was removed from the structure to simplify the model validation using experimental data. Once this is complete, the hexapod can be added to the system and modeled as well.

### **4.2 The Finite Element Model**

The finite element model of the test-bed structure--excluding the hexapod--is the result of an another iterative process. The finite element model was formulated in

ANSYS using a nominal set of assumptions. Then, experimental data was used to aid in the evaluation and improvement of the modeling assumptions. The model was revised until it could reproduce the physical modes discovered in preliminary vibration testing. There is no reason to cover all of the model iterations here. But one example where an assumption was revisited was the discrepancy between the modeled connection of the top plate to the structure and the actual physical connection. The model included five connections originally, but the real structure only had four as shown in Figure 3.6. While it is true that some experimental data was gathered prior to the completion of a realistic finite element model, for reading ease, the final finite element model is described first, followed by correlation with the experimental data.

The FEM contains five different types of elements, all standard within the ANSYS code. Each element type is assigned different “real constants” and “material properties” based on which part of the physical structure the element represents. The next section presents the different types of elements used in the model and describes the real constants and material properties assigned to elements representing particular parts of the structure. There are nineteen different sets of real constants and nine sets different material properties present in the model. The high number of different attributes allows a small part of the model to be changed without affecting the properties of the rest of the model.

#### **4.2.1 The Elements Used**

Of the 1117 element used to model the structure, 436 are ANSYS's BEAM4 elements. Figure 4.1 shows the geometry and node locations for a general BEAM4 element. It is a uniaxial element with tension, compression, torsion, and bending capabilities [1]. The element has 6 degrees of freedom at each node, including translations in the nodal x, y, and z directions as well as the rotations about those axes [1]. The element is defined with two nodes, the cross-sectional area, two area moments of inertia ( $I_{yy}$  and  $I_{zz}$ ), two thicknesses (TKY and TKZ), and the torsional moment of inertia. If the cross section is not symmetric, then the angle  $\theta$  sets the orientation about the element's local x-axis as shown in Figure 4.1. The default is to align the local y-axis with the global X-Y plane. The orientation angle  $\theta$  was not used in the model of the

spacecraft test-bed, because most members of the structure have symmetric cross sections. For those parts of the structure that do not have a symmetric cross section, the area moments of inertia were defined so that the default position would be the correct orientation for the BEAM4 element.

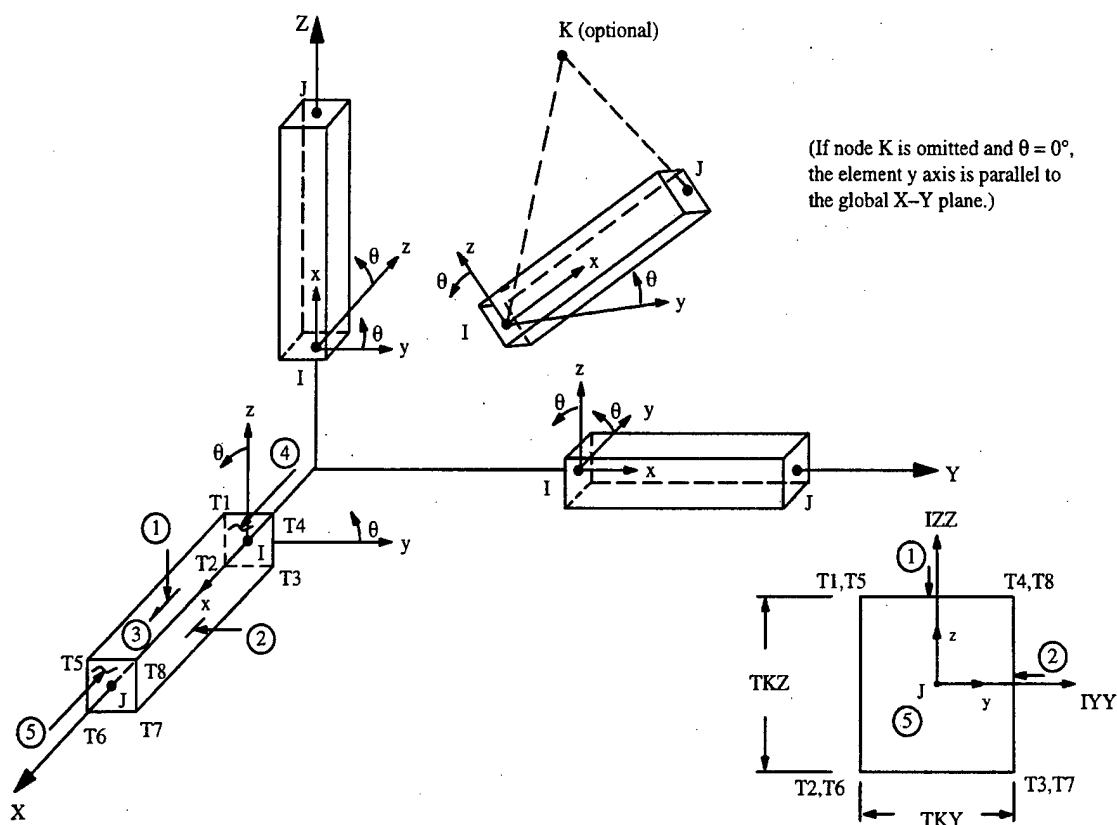


Figure 4.1: The BEAM4 element configuration. The node locations I and J define the element's position.  $TKY$ ,  $TKZ$ ,  $I_{yy}$ ,  $I_{zz}$ , and  $\theta$  must also be defined [1].

Numbering 435, the SHELL63 element is the next most numerous in the FEM of the spacecraft test-bed. Figure 4.2 shows the geometry, node locations, and local coordinate system for the SHELL63 element. It has both bending and membrane capabilities, and accepts both in plane and normal loads [1]. SHELL63 has six degrees of freedom at each of its four nodes, including nodal x, y, and z translation as well as rotation about all three axes [1]. The element is defined with 4 nodes, a thickness at each node, and orthotropic material properties. The rotation angle  $\theta$  is ignored for this model because all of the plates align with one of the global coordinate planes.

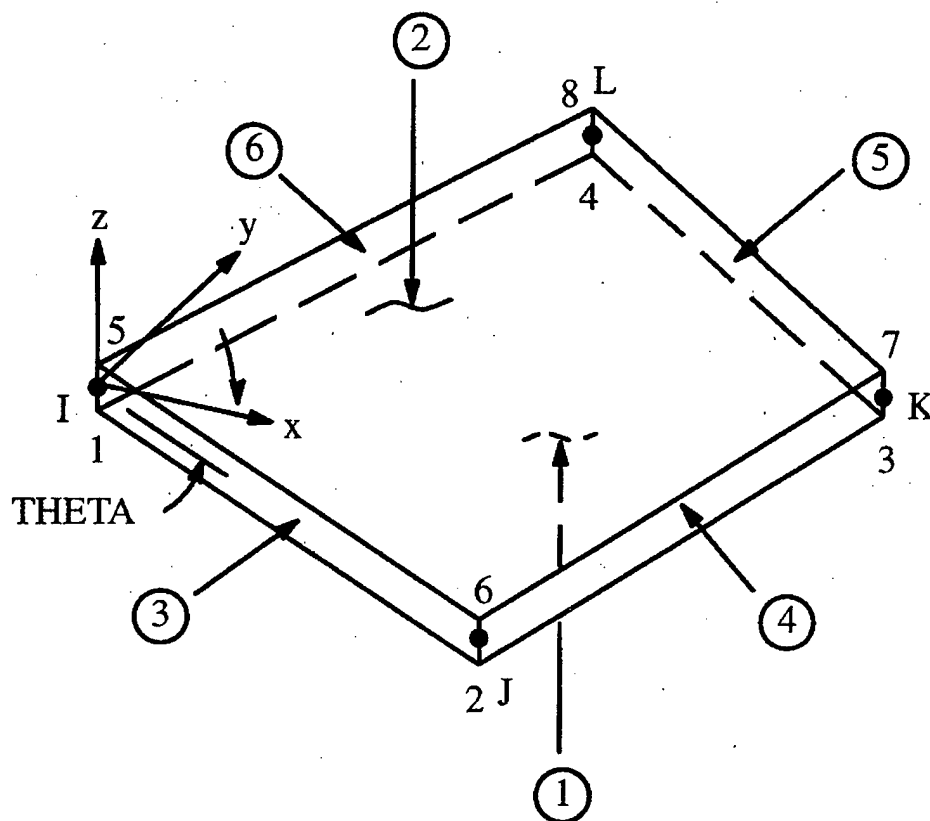


Figure 4.2: SHELL63 element configuration. The letters I, J, K, L define the node locations. Thickness values are input for each node as well. THETA defines the orientation of the local coordinate system [1].

The truss members of the spacecraft test-bed are modeled with 240 PIPE16 elements. Figure 4.3 shows the geometry, node locations, and local coordinate system for the PIPE16 element. Like BEAM4, PIPE16 is a uniaxial element with tension, compression, torsion, and bending capabilities [1]. It has six degrees of freedom including x, y, and z translations as well as rotations about those axes [1]. The element is based on the three-dimensional beam element, but can accept simpler real constant information due to its symmetry and standard pipe geometry [1]. The element is defined with two nodes, the outer pipe diameter, and the wall thickness [1]. A flexibility factor can be defined which divides the cross-sectional moment of inertia. This produces a modified moment of inertia for the bending stiffness calculation [1]. The flexibility factor can significantly lower the stiffness of the truss, and was a useful parameter to vary when trying to match modal peaks. It helped to parameterize some of the uncertainty in



the joints even though this property is assigned to elements that do not directly make up joints in the model.

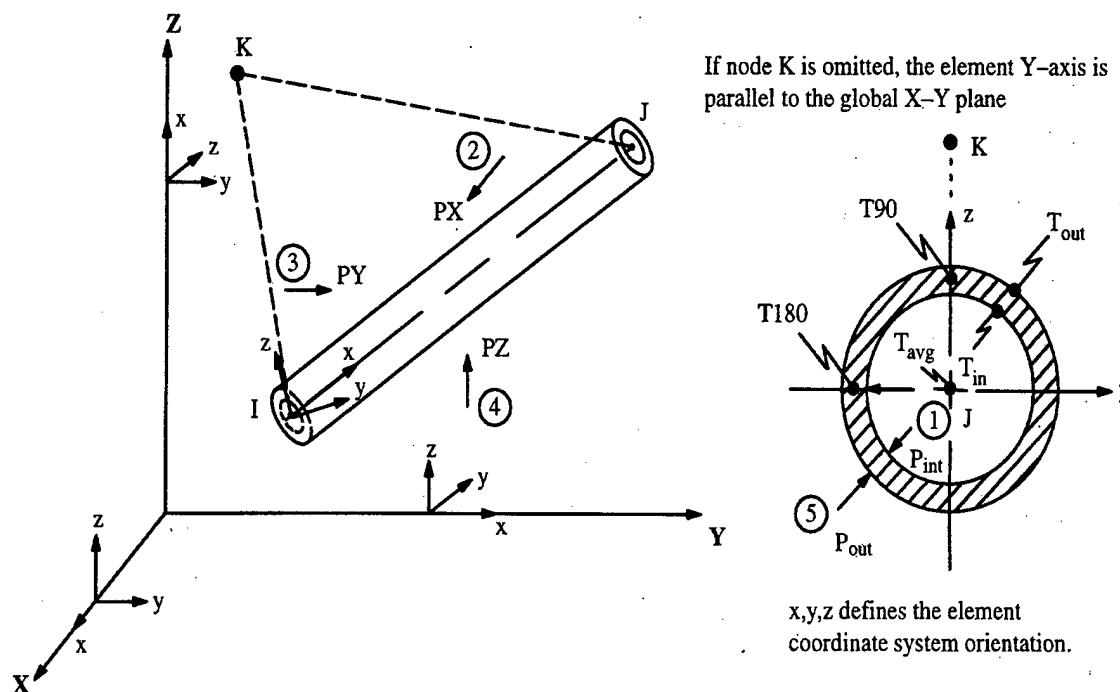


Figure 4.3: PIPE16 element configuration. The letters I and J define the node locations. A third letter K can be used to orient the local coordinate axis. Users must input the outer and inner radius to define the cross section.

Four COMBIN14 elements are used to model the main springs of the suspension system. Figure 4.4 shows the geometry, node locations, and the local coordinate system for the COMBIN14 element. The element has longitudinal capability in three dimensions [1]. It supports three degrees of freedom at each node including x, y, and z translations [1]. Each element is defined with node locations, the spring constant ( $k$ ), and the damping coefficient ( $C_v$ ). In the spacecraft test-bed FEM, the solar array supporting springs are excluded because the spring constant is so low. If they are included in the model, the ratio of the maximum to minimum stiffness coefficients in the model exceeds  $1.0 \times 10^8$ , producing severe round-off errors. Also, 3/16<sup>th</sup>-inch diameter shock cord is strung in parallel with the main test-bed support springs. The shock chord could be modeled by setting  $C_v$  equal to 10% of the spring constant, but the damping capability of the element is unused so that the frequencies and modeshapes exported to MATLAB will be real numbers (i.e. the normal modes of the system).

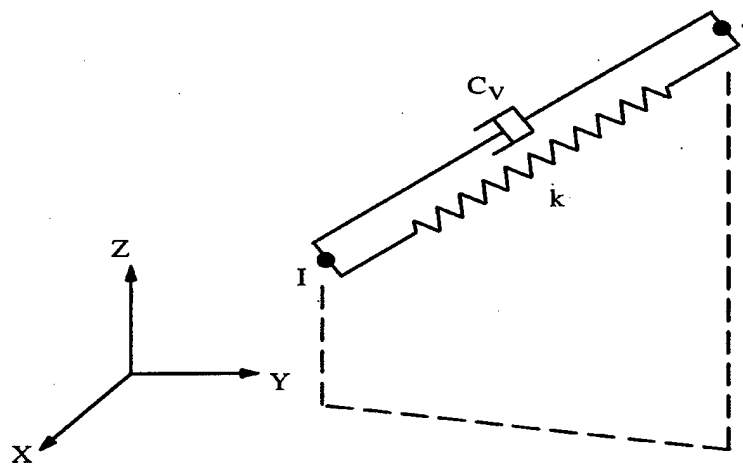


Figure 4.4: COMBIN14 element configuration. The letters I and J define the node locations. The variable  $C_v$  defines the damping constant, and  $k$  defines the spring constant [1].

Two MASS21 elements are used in the model simply to add mass at specific nodes. Figure 4.5 shows the geometry, node location, and local coordinate system of the MASS21 element. The element is defined with a node location and mass. The element can have rotational inertia, but that was assumed to be negligible in this FEM.

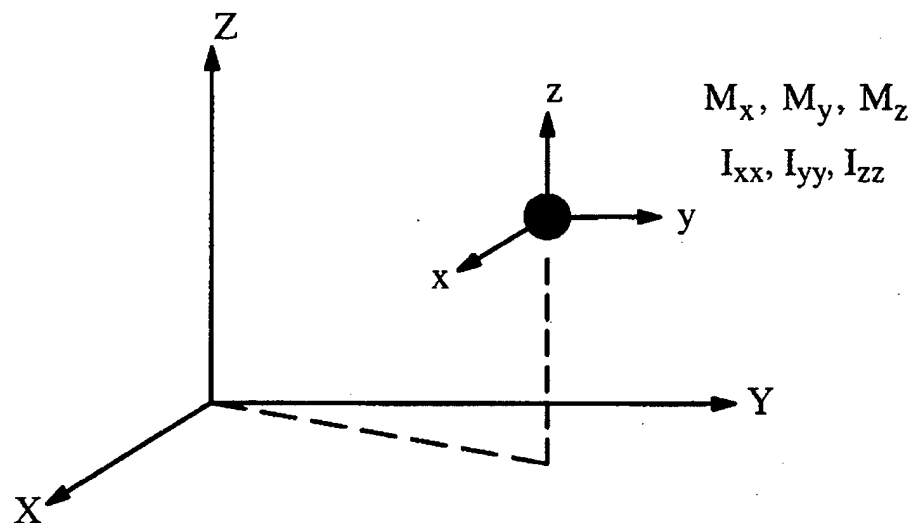


Figure 4.5: MASS21 element configuration. The element is defined with one node, and a single mass ( $M_x=M_y=M_z$ ) [1].

#### 4.2.2 Modeling the Structure

Figure 4.6 shows the entire finite element model as it appears in the ANSYS graphical user interface. The following paragraphs describe how specific parts of the structure were modeled. The description starts at the top of the structure with the spring

suspension system and ends with the disturbance-input node at the very bottom of the structure.

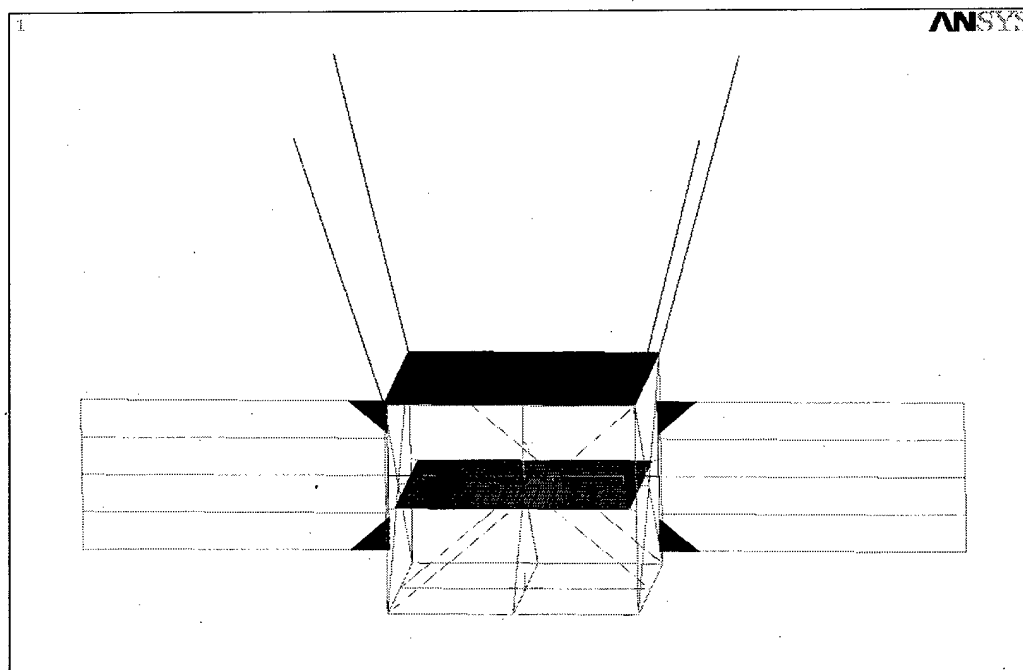


Figure 4.6: Image of the finite element model of the spacecraft test-bed structure in ANSYS.

The main suspension springs are modeled using the COMBIN14 element type. The distance between the nodes defining the ends of the elements corresponds to the undeformed length of the springs. The spring constant for each spring is 490 N/m. The damping coefficient is set to 0, even though the shock chord probably adds 10% damping to the springs. The eigenvalues and eigenvectors of the system remain real if no damping is included in the FEM. Damping is subsequently added in MATLAB.

The top plate of the structure is a 7.82mm thick aluminum plate. The plate is modeled using SHELL63 elements as shown in Figure 4.7. The element thickness is set to 7.82mm at each node. The elastic modulus ( $E$ ) is set to 72Gpa, the density ( $\rho$ ) is set to 2800 kg/m<sup>3</sup>, and poisson's ratio ( $\nu$ ) is set to 0.33. These are all typical values for aluminum. The plate is connected to the truss system at each of its four corners. The plate is raised 5mm above the truss system to prevent accidental coupling of DOFs at places other than the real connections. This requires that an element be added to couple the plate to the truss.

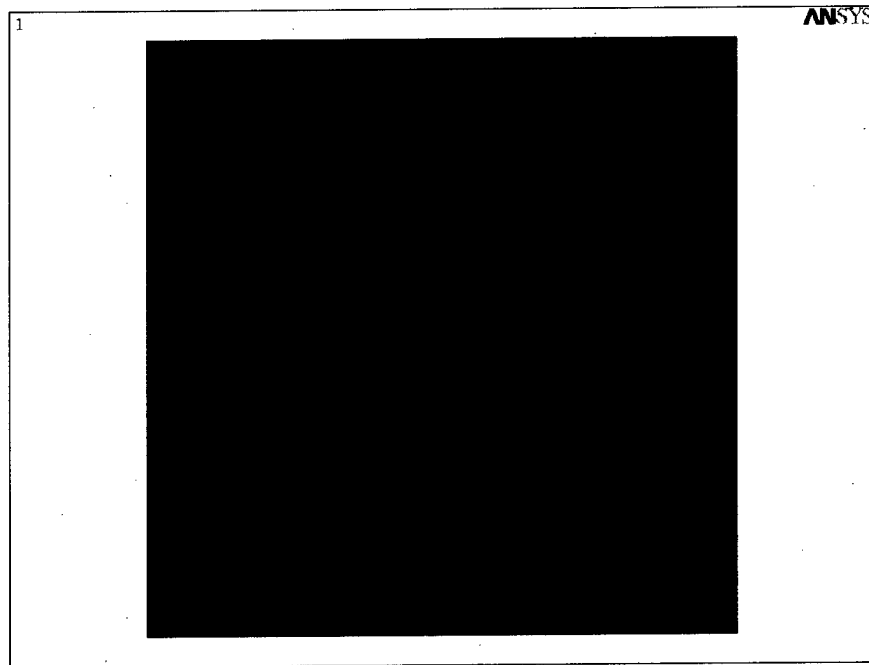


Figure 4.7: Element mesh of the top plate. The number (4) refers to the real constant set assigned to the elements in the model. The material properties are:  $E=72\text{Gpa}$ ,  $\rho=2800\text{ kg/m}^3$ ,  $\nu=0.33$ .

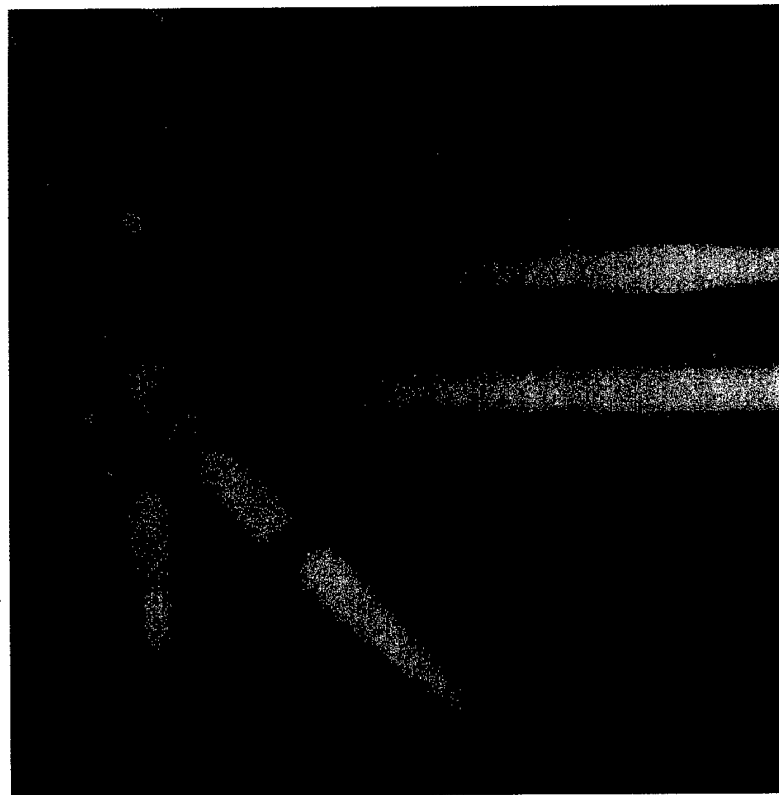


Figure 4.8: Photo of the actual connection between the top plate and the truss.

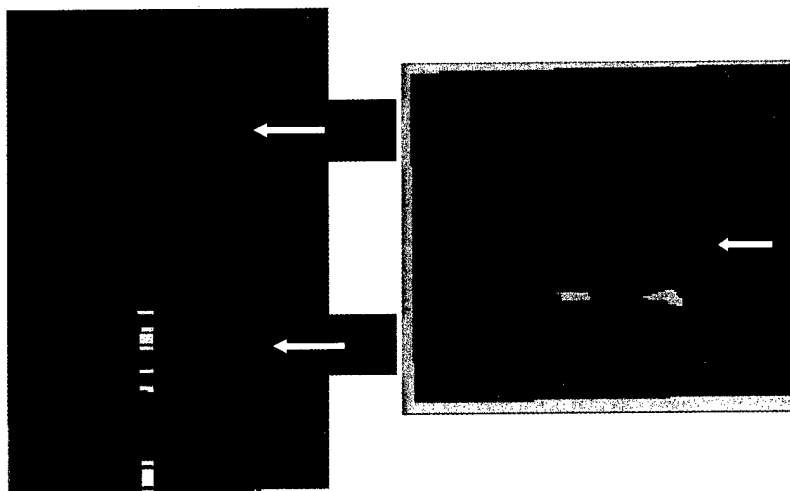


Figure 4.9: Picture of the truss tube ends and the aluminum nodes. The numbers indicate which parts of the joint correspond to the numbers in Figure 4.10.

Figure 4.8 shows a photo of the joint connecting the plate to the truss, and Figure 4.10 shows the modeled connection. Figure 4.9 shows the reader a close-up of the nodes and the ends of the truss members. Because of the complexity in the connections it is difficult to accurately represent the dynamics of the actual joints with these simple models. The model is highly parameterized near the joints to help control the uncertainty.

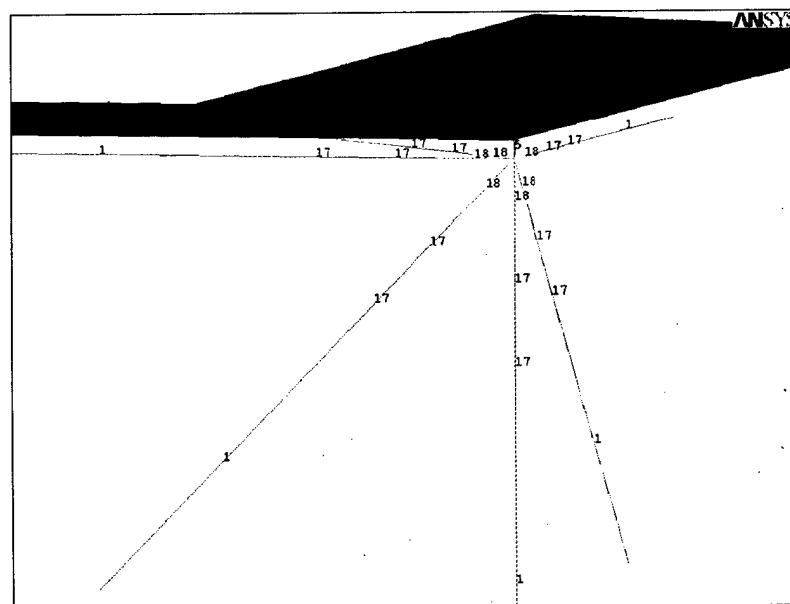


Figure 4.10: Modeled connection between the top plate and the truss at one of the corners. The element marked by the real constant number (5) is the connection element.

Modeling the joints was the most difficult part of the process, and is also the area where the most uncertainty still exists. Figure 4.10 shows five different sets of real constant numbers around the joint that couples the truss to the top plate. The connection element marked by the number (5) is simply a BEAM4 element with the properties of a 1/2" diameter steel shaft. It models the actual steel bolts that connect the top plate to the truss nodes and has the following material properties:  $E=210\text{Gpa}$ ,  $\rho=7800\text{ kg/m}^3$ ,  $\nu=0.3$ . The elements marked by number (18) model the aluminum truss node. The elements marked by number (17) model the length between the nodes and the point where the hexagonal connection bolts turn into the aluminum truss tubes. The elements marked by number (1) model the truss members once they become 30mm diameter hollow tubes. The nodes, truss member ends, and tubes all have the following material properties:  $E=70\text{Gpa}$ ,  $G=26\text{Gpa}$ ,  $\nu=0.33$ , and  $\rho=2800\text{kg/m}^3$ .

The aluminum nodes that comprise each main joint are modeled using the BEAM4 element. The elements have a circular cross section with an outer radius equal to 22.5mm and a wall thickness of 1.63mm. The actual wall thickness of the spherical nodes is 6.35mm. Where there are 4 or more truss members coming together at one joint, the combined material in the model roughly matches that of the actual structure. The nodes are assigned the same material properties as the top plate, although the material properties of the nodes can be changed independently without affecting the properties assigned to the rest of the structure. There is uncertainty in how well these elements represent the physical structure of the joints.

The hexagonal ends of the truss tubes are also modeled with BEAM4 elements. They have a circular cross section with an outer radius equal to 8.25mm and a wall thickness of 3.75mm. The actual wall thickness is about 3mm, but there is also a threaded aluminum bolt inside the hexagonal casing that adds stiffness when the connection is tight. The tube ends have the same material properties as the nodes, and the properties can be changed independently of the rest of the model. Again there is high uncertainty in how well these elements really represent the physical structure.

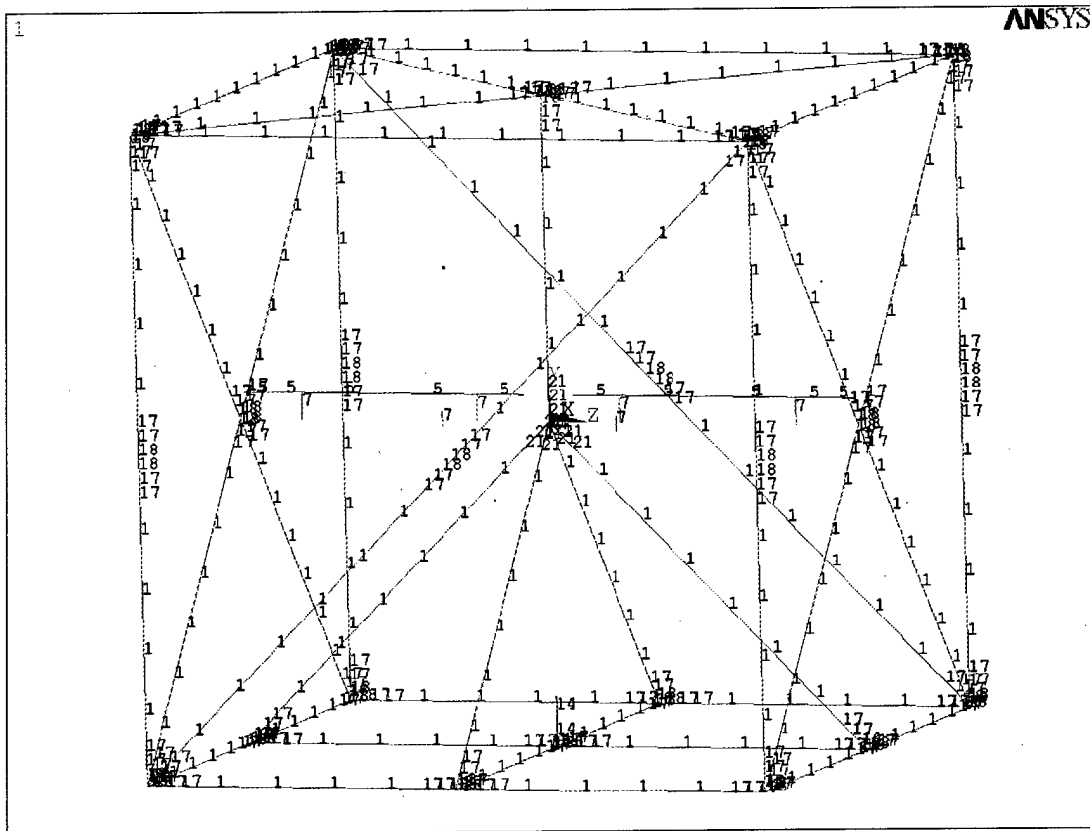


Figure 4.11: Picture of the truss model where the plates have been removed for clarity. The numbers (5), (7), and (14) denote the solar array drive shaft, bearing support blocks, and shaker support sleeve respectively.

Most of the truss is modeled with the PIPE16 element. Every (1) in Figure 4.11 denotes a PIPE16 element with 30mm diameter and 1.5mm wall thickness. The flexibility factor for all of the PIPE16 elements is set to 1.5, because it helped to lower the frequency of the first three modes to better match with experimental data. The material properties for the pipe element are set at  $E=72\text{Gpa}$ ,  $\rho=2800\text{ kg/m}^3$ ,  $\nu=0.33$ . All joints except for the one at the center of the truss use the combination of elements shown earlier in Figure 4.10 to model the truss member-to-node interaction. The connection in the center of the structure was assigned different attributes because of uncertainty in the interaction between the middle plate and the truss at that point. The plate has a hole in it to accommodate the truss member between the middle node and a node in the middle of the top of the truss. The plate is connected to the node using two small angles of aluminum that are bolted both to the plate and to the middle node. Figure 4.12 shows the

actual joint, and Figure 4.13 shows the model of the joint, but excludes the plate. The number (21) corresponds to the real constant set assigned to the elements immediately surrounding the joint. The connection is modeled with BEAM4 elements with a circular cross section, outer radius equal to 8.25mm, and a wall thickness of 1.75mm. They have the same material properties as the nodes.

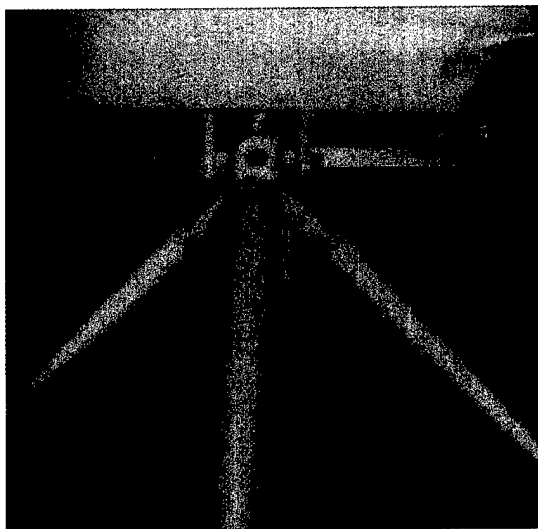


Figure 4.12: Photo of the actual middle joint under the middle plate.

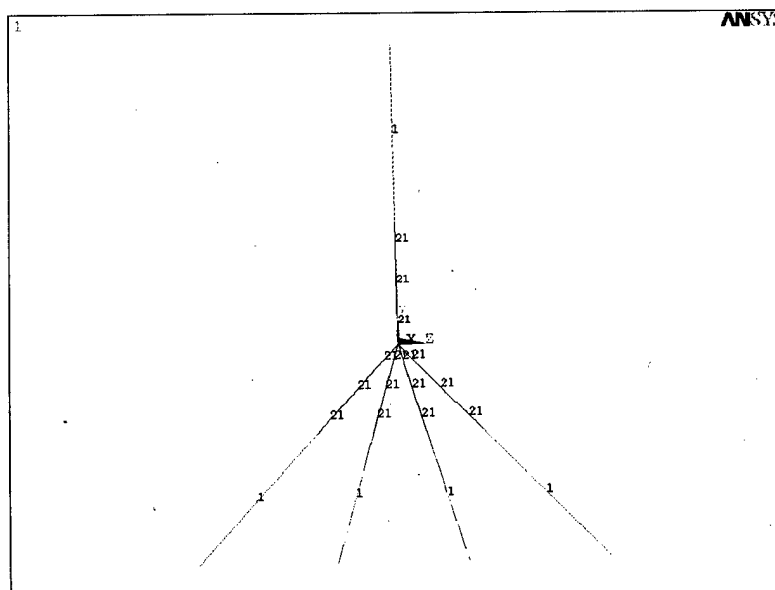


Figure 4.13: Configuration of the middle joint on the structure. This is the only joint where the nodes and the truss member ends are not assigned real constant sets (18) and (17) respectively. The number (21) denotes a different set of real constants for the elements in the joint.



The middle plate of the structure is a 5.72 mm thick aluminum plate. Figure 4.14 shows the plate modeled using SHELL63 elements. The shell thickness is set to 5.72mm at each node. The elastic modulus (E) is set to 72Gpa, the density ( $\rho$ ) is set to 2800 kg/m<sup>3</sup>, and poisson's ratio ( $\nu$ ) is set to 0.33. The plate is connected to the truss system by aluminum angles that connect both to the plate and the nodes. The number (15) denotes the BEAM4 elements used to model the connection between the middle plate and the truss structure. These short beams are assigned a rectangular cross section of 6.35mm x 25.4mm. Since the cross section is not symmetric, care was taken to insure that the elements local y-axis would align with the global X-Y coordinate plane. The short beam elements have the same material properties as the plate, although they can be changed. The number (20) denotes shell elements that are simply thinner than the ones marked with a (3). The thinner elements around the middle node connection model the decreased stiffness due to three large holes that were drilled in the plate.

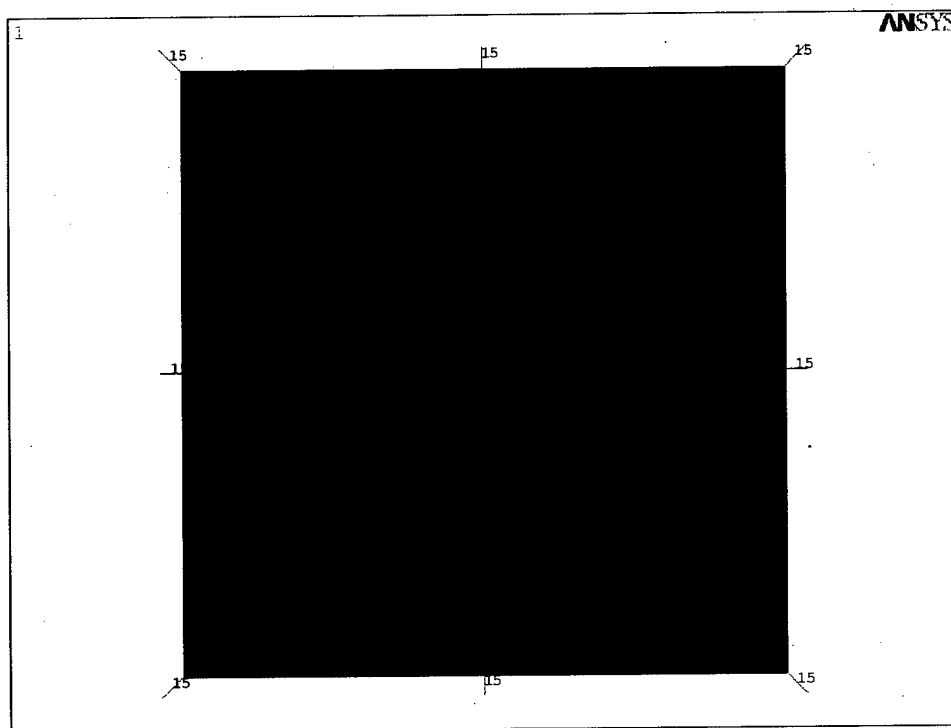


Figure 4.14: Element mesh of the middle plate. The numbers (3), (15), and (20) refer to the real constant sets assigned to the elements in the model. The material properties are:  $E=72\text{Gpa}$ ,  $\rho=2800\text{ kg/m}^3$ ,  $\nu=0.33$ .

The solar arrays are modeled primarily with BEAM4 elements. Figure 4.15 shows the configuration of the right side solar array model. The numbers (2), (5), and (8) denote different real constant sets for the elements. Set number (2) has a cross section of 25.4mm x 25.4mm x 1.4mm wall thickness, and is assigned the material properties of aluminum. Set number (5) has a 12.7mm-diameter solid circular cross-section, and is assigned the material properties of steel, because the solar array drive shaft is made of steel. Set number (8) has the same cross section as set (2), and is assigned the properties of steel to help model the increased material in the area where the drive shaft meets the solar array.

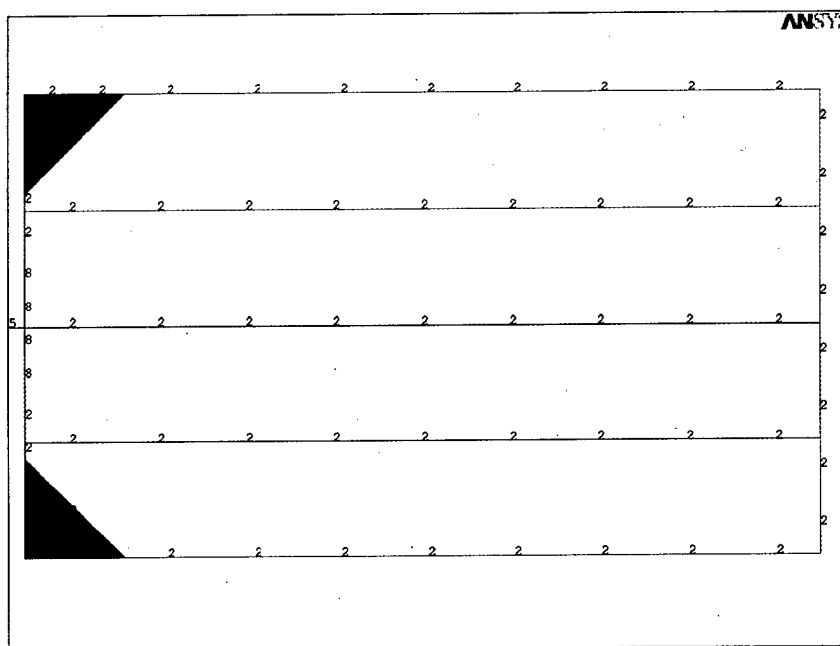


Figure 4.15: Mesh of the model solar array. The numbers (2), (5), (8), and (9) refer to the real constant sets assigned to the elements in the model.

The last part of the model that needs description is the node where the electromagnetic shaker mounts on the structure. The shaker fits in a square aluminum housing that has been machined so that the shaker fits snugly, as shown in Figure 4.16. There are two threaded holes in the housing—one on the bottom and one on the side. The shaker can be oriented for input disturbances in the global X, Y, and Z directions. It attaches at the bottom middle node of the structure, and Figure 4.17 shows how the coupling is modeled. The number (14) denotes the elements that model the shaker and

it's housing. The BEAM4 elements are assigned a cross-section that is 76.2mm x 76.2 mm of solid aluminum. Because the actual shaker assembly has more mass than the elements that model it, a MASS21 element is added to the connection node in the model to get the mass correct. The MASS21 element is set at 0.8kg.

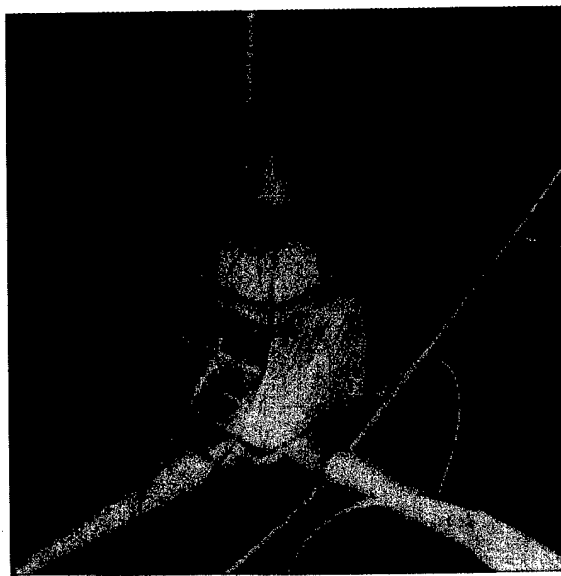


Figure 4.16: Photo of the shaker mounted on the disturbance node.

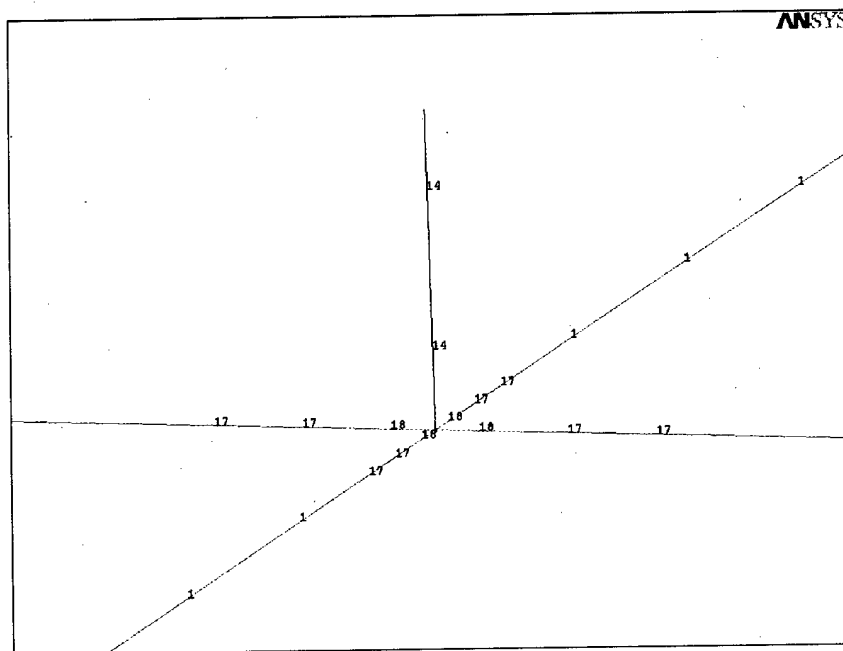


Figure 4.17: Mesh at the disturbance node. The number (14) denotes the real constant set that models the shaker and its housing.

The following boundary conditions and loads are applied to the model before the modal analysis. Experimental data is collected in a 1-g environment, so the effect of gravity is applied to the structure in the global Y-direction. The spring-damper elements that represent the main test-bed suspension system are pinned at the ends that connect to the overhead support truss. The springs supporting the solar arrays are omitted in the model. Figure 4.18 shows the applied boundary conditions and loads as they appear in the ANSYS graphical user interface.

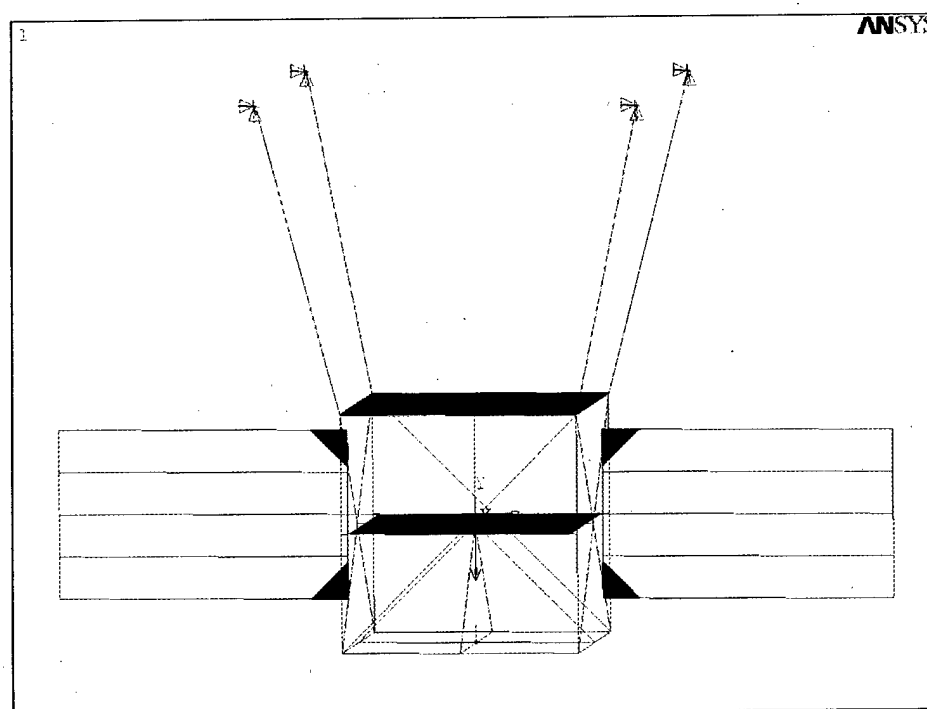


Figure 4.18: Pinned boundary conditions and 1-g acceleration applied to the model.

### 4.2.3 The FEM's Significant Modeshapes

The modal analysis tool in ANSYS allows users to view modeshapes of the model once the eigenvalues and eigenvectors of the system are calculated and stored. Animating the modeshapes helps visualize the actual structure's physical modeshapes motion. While eighty modes were extracted from the model, only a few were helpful in gaining insight into the behavior of the physical structure. These modes are the most observable in both the ANSYS model and the physical structure. The model described in the previous section is the result of varying parameters in the FEM so that the frequencies

of the model would come close to matching the modes shown in the experimental data. The following paragraphs describe some of the low frequency modes as well as a few of the most important frequencies and modeshapes extracted from the ANSYS model.

The first six modes extracted from the model were the low frequency bounce and pendulum modes of the suspension system. The bounce mode in the Y-direction is at 0.68 Hz. The next six modes correspond to the solar arrays. The first natural frequency of the solar arrays is much lower than predicted as Figure 4.19 shows. This is due to the approach used to physically attach the arrays to the structure. The drive mechanism for each array is a steel shaft, and it acts as a long beam with a 3kg mass (the array) at one end. The first mode for the arrays is 2.6Hz--rather than the designed 8.6Hz--even though there is little uncertainty in how the arrays are modeled. The solar array modes are difficult to validate with experimental data because the shaker used to input the disturbance does not excite the system very well below 10 Hz. Figure 4.20 shows another one of the six solar array modeshapes.

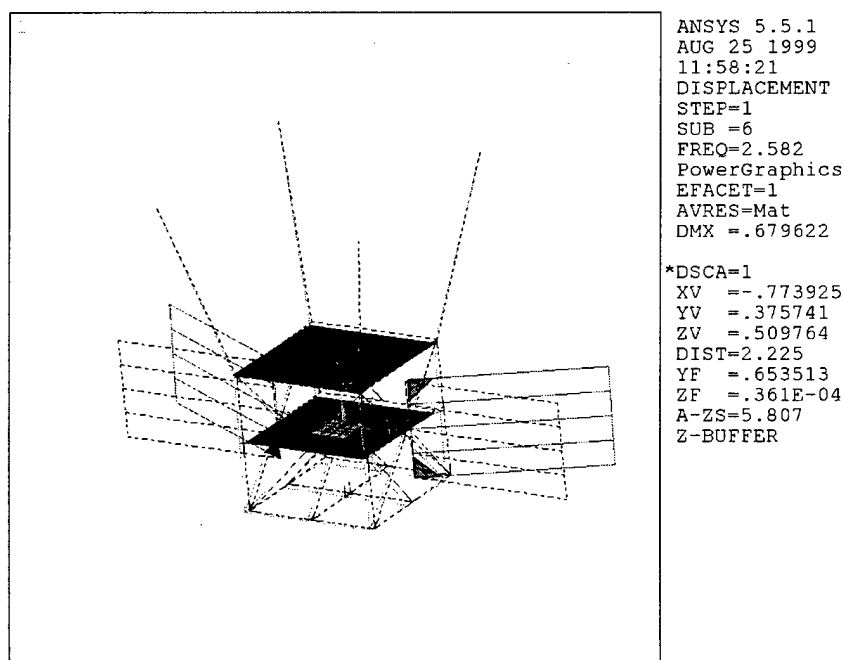


Figure 4.19: First mode of the solar arrays. The number following FREQ in the legend corresponds to the frequency of the mode (Hz). All other output in the legend refers to the scaling information used to plot the modeshape.

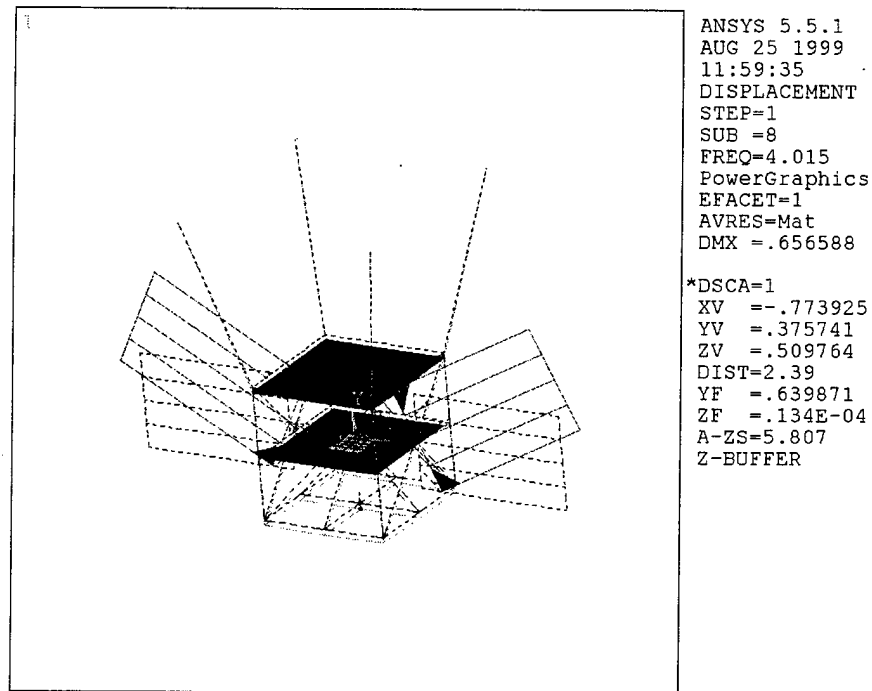


Figure 4.20: Another of six solar array modes.

There are three well-defined modes easily excited with a disturbance in the global Y-direction (straight up). The first of these modes is at 21.3 Hz in the model, and it is dominated by the dynamics of the top plate. Figure 4.21 shows the ANSYS output for this particular mode. A formula from Blevin's book provides an approach to checking this result [2]. The frequency for the first mode of a square plate, simply supported on all sides is governed by equation 4.1.

$$f_{11} = \frac{11.45}{2\pi a^2} \left[ \frac{Eh^3}{12\rho h(1-\nu^2)} \right]^{\frac{1}{2}} \quad (4.1)$$

In this equation,  $E$  is the elastic modulus,  $h$  is the thickness,  $a$  is the width,  $\rho$  is the density, and  $\nu$  is poisson's ratio. The frequency is in Hz, and the subscript refers to the number of half sine waves along each edge. According to this equation, the top plate should have a first fundamental frequency at 20.67. Another way to validate that the model is correct is to excite the physical system with a sine wave disturbance at 21 Hz. Doing so causes considerable vibration at the middle of the top plate, easily observed with the naked eye.

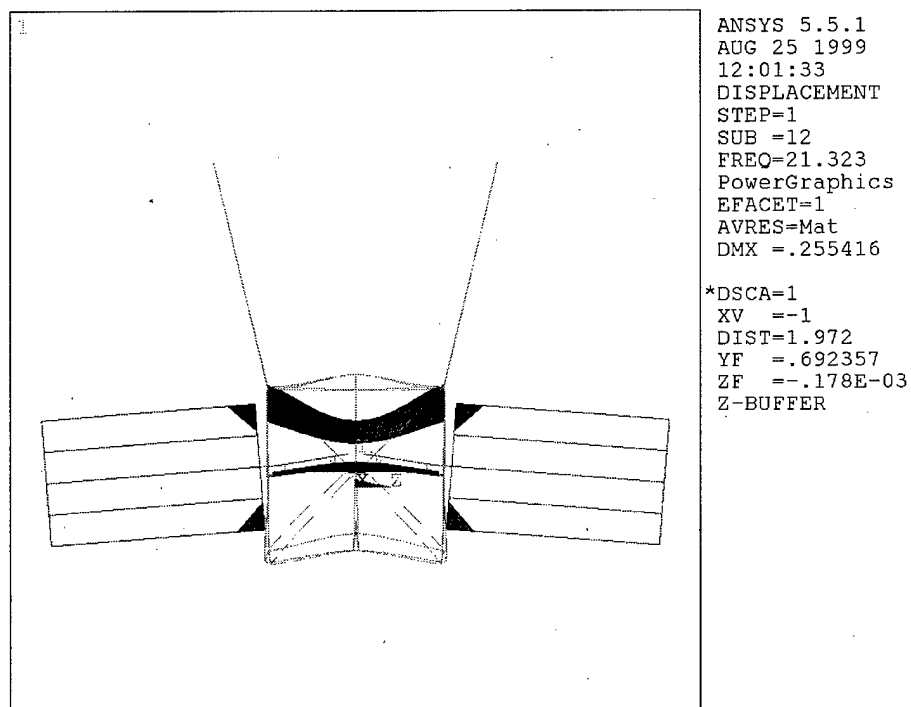


Figure 4.21: The first mode of the main truss at 21.3 Hz. The mode is dominated by the dynamics of the top plate.

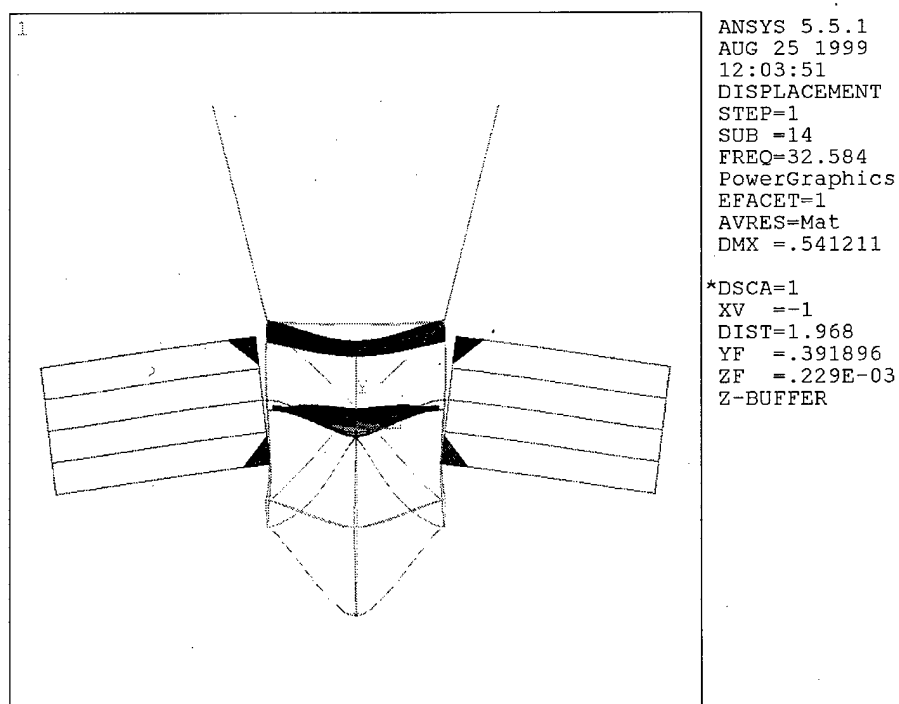


Figure 4.22: The second mode of the main truss where movement is primarily in the global Y-direction. The frequency is 32.58 Hz.

The second of these important modes is at 32.58 Hz, and it is dominated by the dynamics of the node supporting the shaker mechanism. Figure 4.22 shows the ANSYS output for this modeshape. Note that this mode is the result of the 2.8kg mass the shaker assembly adds to the structure. If the shaker were removed from the system, this mode would have a much higher frequency. Again the prediction of the model is verified by exciting the system at 32.5 Hz in the global Y-direction. The four truss members that share the node with the shaker assembly vibrate much more than the rest of the structure when excited at this frequency.

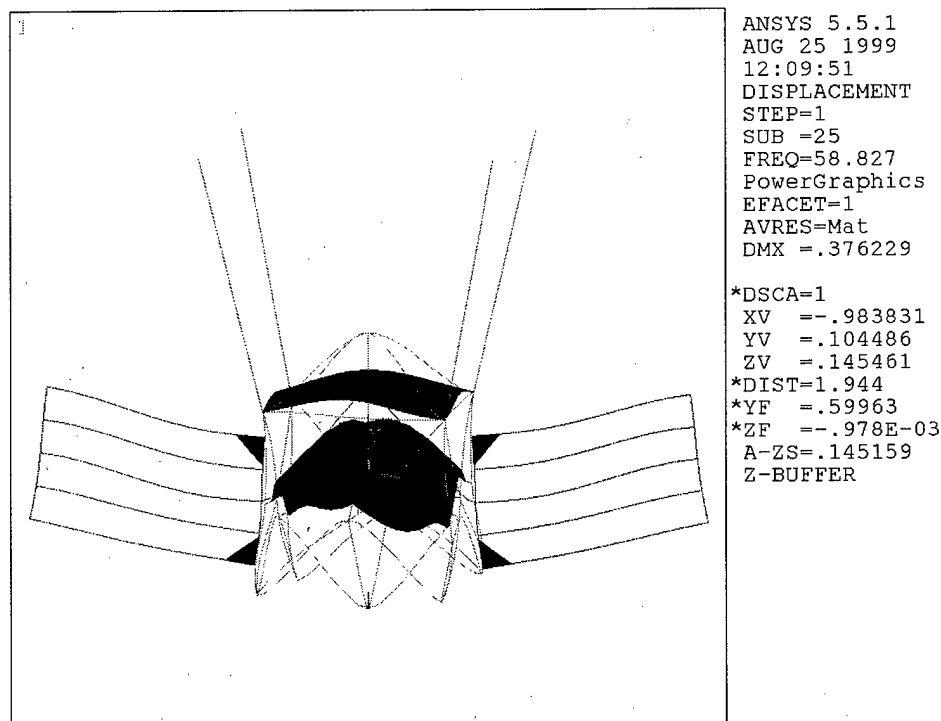


Figure 4.23: Third mode of the main truss where movement is primarily in the global Y-direction. The frequency is 58.8 Hz.

The last mode in the global Y-direction that can be easily correlated with observable movement on the actual structure is shown in Figure 4.23. This mode corresponds with the first fundamental frequency of the middle plate, although it would be difficult to show this with hand calculations because of all the connections on the plate. However, when the structure is excited in the global Y-direction at 56Hz, the middle plate vibrates with higher amplitude than the rest of the structure. This can be



observed simply by touching the middle plate and other parts of the structure at the same time.

There is one more mode in the model that corresponds well with the actual structure. Figure 4.24 shows the first modeshape where the vibration is primarily in the global Z-direction. The mode is at 30.79Hz. A similar mode on the actual structure can also be observed by touching the structure while exciting it with a 29Hz disturbance in the global Z-direction.

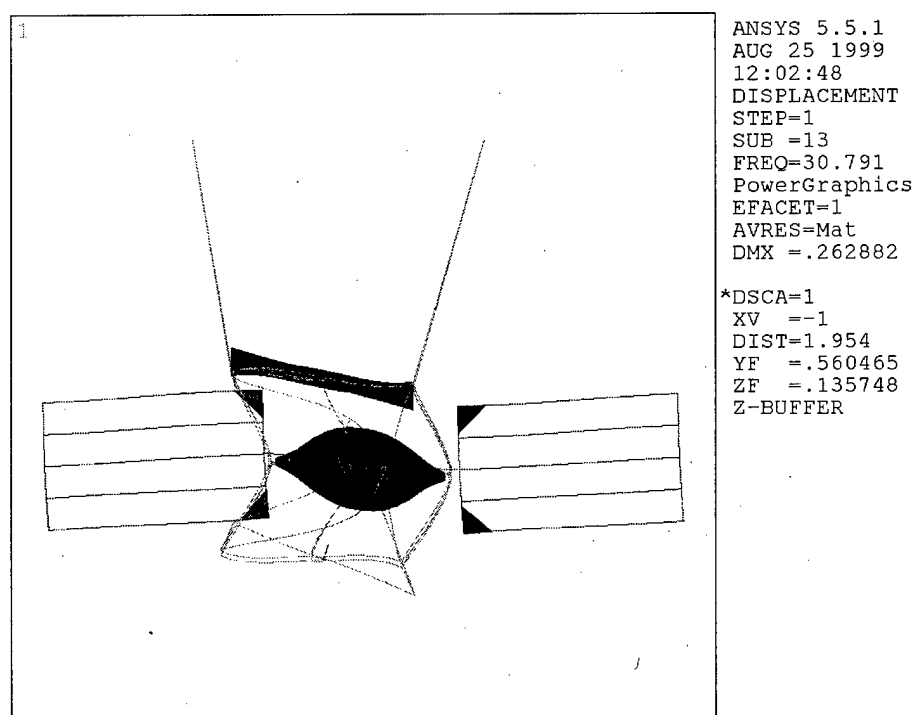


Figure 4.24: First mode where motion is primarily in the global Z-direction. The mode is at 30.79Hz.

### 4.3 Converting the Model from ANSYS to MATLAB

ANSYS is a powerful modal analysis tool, but its input/output modeling capabilities are limited. The only way to validate the FEM is to overlay experimental data on the model's predicted transfer functions. MATLAB is much better at creating transfer functions and input-output state space models than ANSYS, so the FEM needed to be converted to a form usable in MATLAB. To solve this problem, the natural frequencies and mass normalized modeshapes were exported from ANSYS to MATLAB.

The data that is stored in the mass  $[M]$  and stiffness  $[K]$  matrices in ANSYS can be approximated with the model's natural frequencies and modeshapes if enough modes are extracted. The following paragraph explains why this is true.

When ANSYS performs a modal analysis on a model, it sets up and solves for the eigenvalues and eigenvectors of the vector differential equation shown in equation 4.2.

$$[M]\ddot{\bar{x}} + [K]\bar{x} = 0 \quad (4.2)$$

The vector  $\bar{x}$  corresponds to the physical degrees of freedom for the system. If the user so chooses, ANSYS normalizes each mode shape (eigenvector) to the mass matrix so that  $\Phi^T [M] \Phi = [I]$ , where  $\Phi$  is the matrix of modeshape vectors and  $I$  is the identity matrix. Note that the modeshape vectors are the eigenvectors of the system, and are orthogonal. A DOF transformation can then be defined,

$$\bar{x} = \Phi \bar{\eta} \quad (4.3)$$

where  $\eta$  is the set of "modal" coordinates, so that 4.2 can be rewritten as shown in equation 4.4.

$$[M][\Phi \ddot{\eta}] + [K][\Phi \eta] = 0 \quad (4.4)$$

Each state variable is now a linear superposition of the modal coordinates. Pre-multiply equation 4.4 by  $\Phi^T$  to get the result shown in equation 4.5.

$$\Phi^T [M][\Phi \ddot{\eta}] + \Phi^T [K][\Phi \eta] = 0 \quad (4.5)$$

This is simply a similarity transformation, and the dynamics (eigenvalues) are completely equivalent to 4.4. The following two equations also hold:  $\Phi^T [M] \Phi = [I]$  and  $[K] \Phi = [M][\bar{\Lambda}] \Phi$ , where  $\Lambda$  is the vector of eigenvalues and the second equation is the standard eigenvalue problem. The problem can then be re-written as shown in 4.6.

$$[I]\ddot{\eta} + [\Lambda]\eta = 0 \quad (4.6)$$

If there is a forcing function  $w$  on the right hand side, then

$$[I]\ddot{\eta} + [\Lambda]\eta = \Phi^T \beta_w w \quad (4.7)$$

The  $\beta_w$  matrix defines the degree(s) of freedom where the disturbance  $w$  enters the system. Both equations 4.6 and 4.2 can be used to describe the unforced dynamics of the system, but 4.6 is much simpler because the system has been decomposed into modes. Using equation 4.6, all that is required to create a model in MATLAB, very similar to the one in ANSYS, is a set of natural frequencies and modeshapes large enough to capture an acceptable amount of the model's dynamics. Note that the eigenvalues are the square of the natural frequencies for the model. The output from the specific degree(s) of freedom is given by,

$$y = C_x \Phi \bar{n} \quad (4.7)$$

Transferring the natural frequencies and modeshapes to MATLAB from ANSYS is a simple process, but requires that all relevant ANSYS output be in text format. The frequencies for the extracted modes can be displayed in the "Results Summary" window of the ANSYS general postprocessor. This output must be saved as a text file. The "Nodal Solution" for each modeshape can be displayed in the "List Results" window of the ANSYS general postprocessor. Each modeshape must be saved as a separate text file. Two m-files, *get\_phi* and *get\_freqs*, were written to read the  $[\Phi]$  and  $[\Lambda]$  matrices into MATLAB. These two m-files are listed in Appendix A. The  $[\Phi]$  matrix is very large, so it is a good idea to run *get\_phi* only once. With frequency and modeshape information, an input-output state space model can be created in MATLAB. Then transfer functions are easily created with the input-output model.

#### 4.4 Creating the Input-Output State Space Model

The input-output state space model is created in MATLAB using the first eighty natural frequencies and modeshapes from the finite element model. The eightieth extracted mode is at 168 Hz, and there are 6744 degrees of freedom in the model. Proportional modal damping is added to the model in MATLAB. The damping matrix is the second term in equation 4.8. Adding the damping term forces the eigenvalues of the system to be complex and more representative of the physical system. The damping ( $\zeta$ ) for each mode was initially set at one percent. The damping ratios for modes between 10

and 110Hz could be estimated from the experimental data using half power-bandwidth. However, it was not possible to correlate damping ratios for the model's modes with the experimental data's modes until the modal frequencies were a close match.

$$[I]\ddot{\eta} + [2\zeta\omega_r]\dot{\eta} + [\Lambda]\eta = \Phi^T \beta_w u \quad (4.8)$$

A first order set of state space equations that represent the system is developed so that manipulation in MATLAB is convenient. First, define the state vector shown in equation 4.9, where  $\bar{\eta}$  is a vector of the modal position and velocity.

$$\bar{\eta} = \begin{bmatrix} \eta \\ \dot{\eta} \end{bmatrix} \quad (4.9)$$

Then, differentiate it once and substitute in equation 4.8 for  $\ddot{\eta}$  to get equation 4.10.

$$\dot{\bar{\eta}} = \begin{bmatrix} \dot{\eta} \\ \ddot{\eta} \end{bmatrix} = \begin{bmatrix} 0 & I \\ -\Lambda & -2\zeta\omega_r \end{bmatrix} \begin{bmatrix} \eta \\ \dot{\eta} \end{bmatrix} + \begin{bmatrix} 0 \\ \Phi^T \beta_w \end{bmatrix} w \quad (4.10)$$

The desired output ( $y$ ) from the model is acceleration, because the experimental data from the physical system is measured with accelerometers. Equation 4.11 shows the output equation for the state space system as a function of modal position and velocity. The output equation is pre-multiplied by  $[\Phi]$  to transform the output back into global physical coordinates, and the  $C_{y\eta}$  matrix corresponds to physical degrees of freedom.

$$\ddot{y} = \begin{bmatrix} C_{y\eta} & \Phi \end{bmatrix} \begin{bmatrix} -\Lambda & -2\zeta\omega_r \end{bmatrix} \begin{bmatrix} \eta \\ \dot{\eta} \end{bmatrix} + \begin{bmatrix} C_{y\eta} & \Phi \Phi^T \beta_w \end{bmatrix} w \quad (4.11)$$

The matrices of equations 4.10 and 4.11 are A, B, C, and D, or the matrices needed to create a state space model in MATLAB. The actual input to the real system is simply a voltage from a Dynamic Signal Analyzer, which drives an electromagnetic shaker. The model for the shaker, important for model-data correlation, is discussed in the next chapter, because it is completely derived from experimental results. The block diagram below shows the model of the shaker. The model of the shaker and the model of the test-bed must be combined in series for the model to match the data.

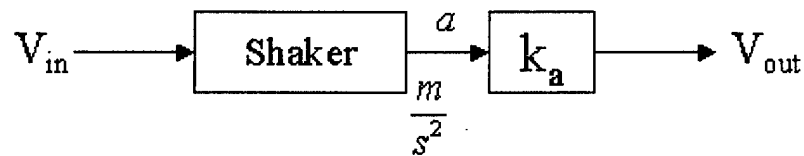


Figure 4.25: The shaker model block diagram.

In Figure 4.25,  $V_{in}$  is the input voltage from the DSA,  $k_a$  is the conversion constant for the accelerometer of 1 volt/g or  $1/9.8 \text{ m/s}^2$ , and  $V_{out}$  is the output voltage from an accelerometer on the shaker's proof mass. The output of the shaker model is a voltage, but the desired input to the test-bed model is force, as shown in Figure 4.26. The output of the shaker model needs to be multiplied first by the inverse of  $k_a$  and then by the size of the proof mass ( $M_p$ ) to get force, because  $F=ma$ . The size of the proof mass (0.07kg) divided by  $k_a$  is the scaling factor that must multiply the B and D matrices in the test-bed model to convert the input units to force. Then the output of the test-bed model (acceleration) must be multiplied by the accelerometer constant ( $k_a$ ) to put the output into the same units as the data. Appendix A lists the m-file (*model\_create.m*) written to create the input-output state space model in MATLAB.

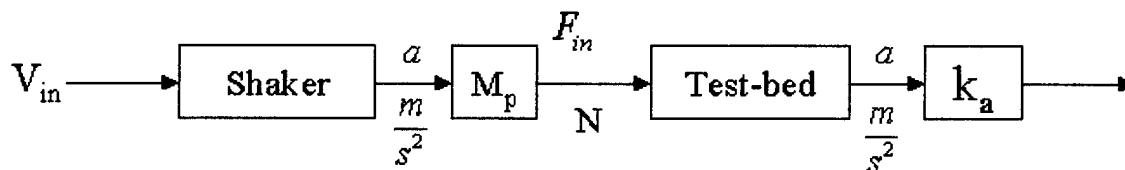


Figure 4.26: Shaker and Test-bed systems combined in series (data collection setup).

## Chapter 5: Data Collection and Model Correlation

This chapter briefly describes the tools and methods used to collect modal data from the physical structure. It also describes the need for an input-output state space model of the electromagnetic shaker, and shows how the model was developed. The chapter then briefly explains the m-files written to create the first generation state space model and overlay model bode plots on the experimental data. Several transfer function plots are included in the text.

### 5.1 Modal Analysis Setup

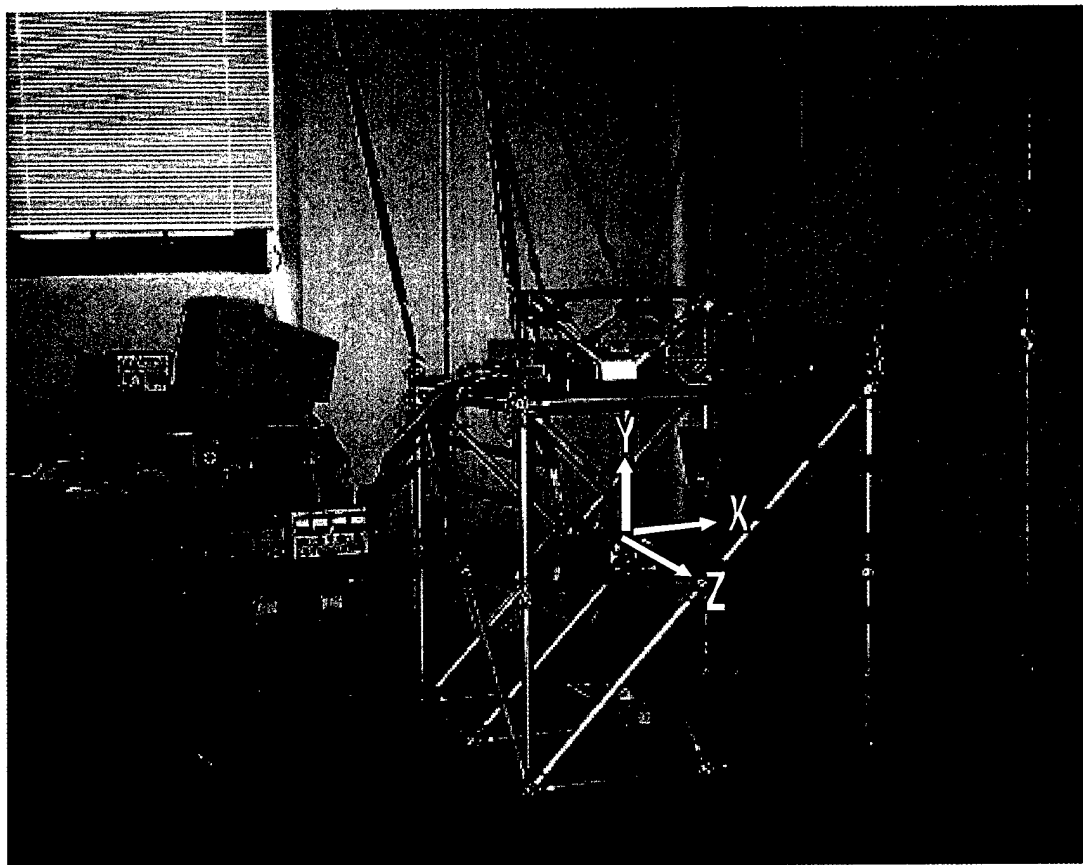


Figure 5.1: Modal analysis setup. A DSA inputs a random voltage to the shaker at the base of the structure. The measured outputs come from small Kistler accelerometers attached to the structure. The coordinate system in the figure above matches the global coordinate system used in the FEM.

The photograph above shows the hardware used to excite and collect modal data from the structure as well as the hexapod and test-bed. There is one Dynamic Signal Analyzer, an amplifier, a two-channel oscilloscope, a signal conditioner, two Ling

Dynamic Systems electromagnetic shakers with 70 gram proof masses, and eight small Kistler accelerometers shown in the photograph. Figure 5.2 shows the accelerometer type and signal conditioner used to collect the data. The accelerometer attaches to a point on the structure with a small ball of adhesive wax. The wax connection method facilitates easy movement of the accelerometer about the structure. Note that the hexapod was removed for the modal analysis, and only a single shaker excited the structure, rather than the two shakers shown in Figure 5.1. The coordinate system superimposed on the photo corresponds to the global coordinate system used in the finite element model.

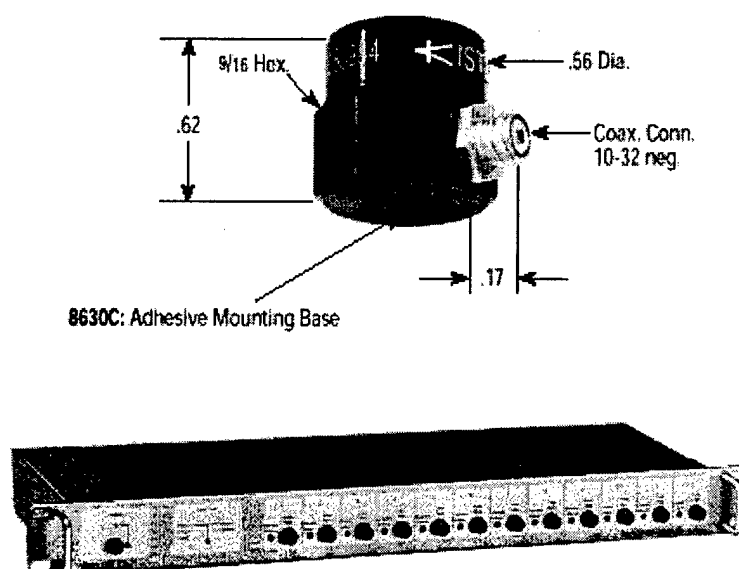


Figure 5.2: The Kistler accelerometer (type 8630C) and signal-conditioning unit used for modal analysis.

The following paragraph describes the data collection process. A schematic of the data collection setup is shown in Figure 5.3. The Dynamic Signal Analyzer (DSA) generates a random signal that drives the shaker and proof mass at the bottom of the structure. Small accelerometers measure the acceleration at designated positions on the structure (see Figure 5.4), and their signals feed through the signal conditioner back to the DSA. The DSA then generates a transfer function--from the shaker input voltage to the accelerometer output voltage--and displays it in a bode diagram. The complex transfer function data is then saved and converted to MATLAB format with an executable called

*sdftoml.exe*. All data was collected using the fast fourier transform (FFT) option on the DSA with a random signal input. The band-limited frequency range for the random signal was set between 10 Hz and 110Hz. The small proof mass on the electromagnetic shaker does not excite the system well below 10 Hz because of the modified corner frequency, so lower frequency data is unreliable. The accelerometers could be moved to any position on the truss structure. Figure 5.3 shows only one accelerometer for clarity, but 8 were available. The DSA has two channels, so only one signal could be analyzed at a time. Figure 5.4 shows the location of the sensors that produced the experimental data plotted in this chapter.

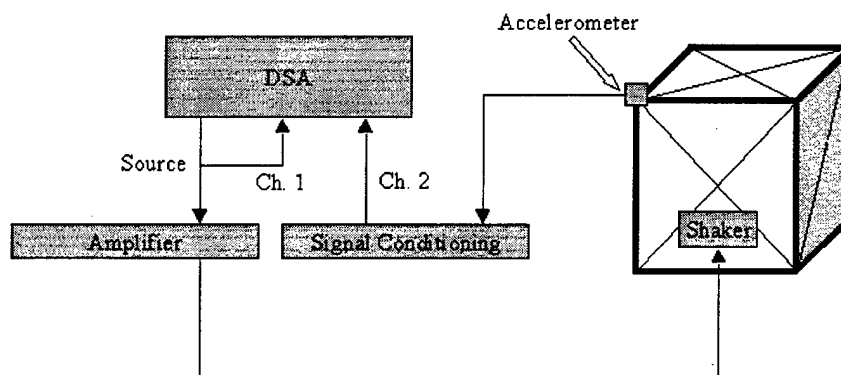


Figure 5.3: Schematic of the data collection setup up. The source signal is amplified before reaching the electromagnetic shaker, and the accelerometer's signal is amplified with the signal-conditioning unit before reaching the DSA.

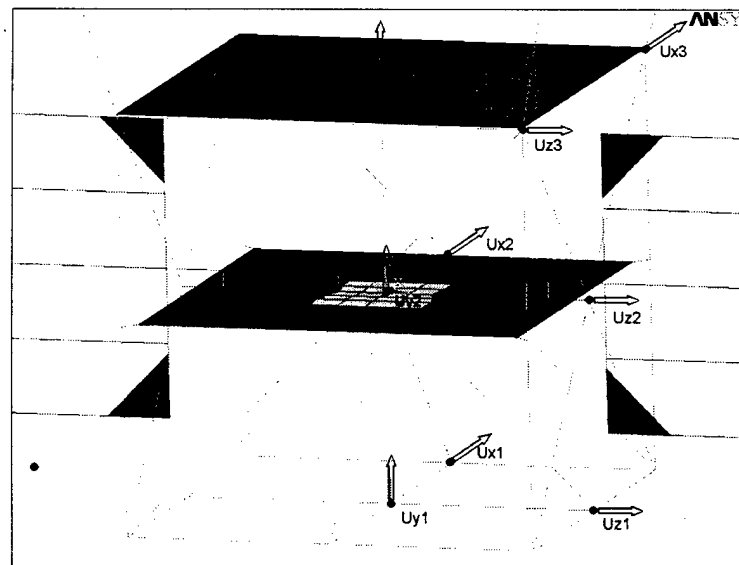


Figure 5.4: This figure shows the location of the accelerometers that produced the experimental transfer functions shown in this chapter. The arrows indicate the signal direction.



## 5.2 Electromagnetic Shaker model

The electromagnetic shaker is an electro-mechanical system independent of the spacecraft test-bed. As a result, the real disturbance input to the test-bed is not the DSA's source voltage, but the force exerted on the system by the proof mass the shaker actuates. A model of the shaker must be included in the system in order to correlate the model and experimental data transfer functions. The shaker has its own break frequency that varies with the size of the proof mass. The size of the proof mass (70 grams) was selected using the technical specifications for the Ling Dynamic Systems vibration generator (model 101/102). The equation for selecting the proof mass is,

$$L = \frac{(S - D)K}{0.01962} \quad (5.1)$$

where  $L$  is the maximum load in grams,  $S$  is the rated peak-to-peak armature travel in mm,  $D$  is the desired displacement in mm at low frequency, and  $K$  is the armature suspension stiffness in N/mm.  $S$  and  $K$  are given as 2.5mm and 3.15 N/mm respectively, and  $D$  was estimated to be 2.0 mm of displacement at low frequency. The maximum load for this estimate is 80 grams, so a 70-gram mass was chosen to avoid overloading the shaker.

A model of the shaker was developed and combined with the test-bed's MATLAB model by connecting the output of the shaker (force) to the input (force) of the test-bed. In order to develop the most accurate model possible, the model of the shaker was fitted to experimental data. The experimental transfer function between the input voltage to the DSA and the output voltage of an accelerometer attached to the proof mass is shown in Figure 5.5. The m-file written to match the model transfer function to the experimental one (*check\_shake.m*) is shown in Appendix A. The solid line in the frequency plot is the transfer function shown below in equation 5.2. It matches the data quite well,

$$\frac{V_{out}}{V_{in}} = 0.00005 \frac{s^2}{\frac{s^2}{220^2} + \frac{2 \cdot 0.17 \cdot s}{220} + 1} \quad (5.2)$$

where  $V_{in}$  is the input voltage,  $V_{out}$  is the output voltage from an accelerometer on the proof mass. The output of this model is converted to units of force by multiplying by the size of the proof mass and  $1/k_a$  so that the new transfer function looks like,

$$\frac{F_{out}}{V_{in}} = 0.00005 \frac{s^2}{\frac{s^2}{220^2} + \frac{2 \cdot 0.17 \cdot s}{220} + 1} \cdot \frac{M_p}{k_a} \quad (5.3)$$

where  $F_{out}$  is the force out in newtons,  $M_p$  is the size of the proof mass in kg, and  $k_a$  is the conversion constant for the accelerometer in  $V/m/s^2$ . The mass is 0.07kg and the constant  $k_a$  is 1/9.8.

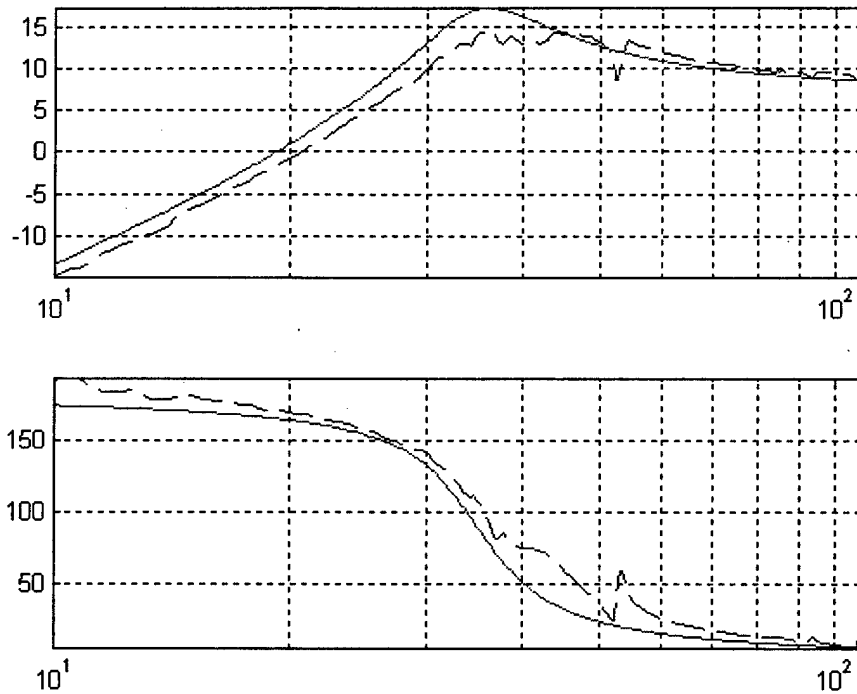


Figure 5.5: Experimental and modeled transfer function from the voltage in ( $V_{in}$ ) to an accelerometer on the proof mass between 10 Hz and 110 Hz. The data was taken on a rigid base. The dotted line is experimental and the solid line is the model.

### 5.3 Data collection and model correlation

Data was collected with the shaker exciting the system in each of the global directions shown in Figure 5.1. The accelerometers were oriented to measure the response of the system in the same global direction as the disturbance. There are 32 sets

of data for a y-disturbance to y-output. There are 9 sets each for the x- and z-disturbance to x- and z-output. Many more sets of data were collected in the y-direction to help characterize the modes of the top and middle plates, but these are not shown in this thesis.

The m-file *model\_create.m* overlays the model's transfer functions on the collected experimental data. The m-file is shown in Appendix A. The code creates a modal damping matrix to add to the model, where the user can vary the value of the modal damping. It also allows the user to input a phase correction factor and a feed through correction value. The phase correction is needed because the orientation of the accelerometer of interest may vary by 180 degrees (upside down) for some of the data sets. The feed through correction is needed to make up for the truncation of the higher frequency modes. The code creates a state space model for the electromagnetic shaker and one for the spacecraft test-bed. Then the two models are combined in series. The feed through correction is added to the D matrix of the final state space model. In every nearly every case, the same feed through value (0.015) is required for the model transfer function to match the experimental data at low frequency. Two of the transfer functions required a correction term of 0.01. The m-file then plots each set of experimental data and the corresponding model transfer function on the same set of axes for easy comparison.

The reader should note that all data was collected at points on the main truss structure of the spacecraft test-bed. The solar arrays were included in the FEM, but no attempt was made to match transfer functions using sensors on the solar arrays. The primary reason for this is that the small proof mass on the electromagnetic shaker does not excite the system well at low frequency, where the array modes are most prevalent. One solution to this problem would be to use a large grounded shaker to excite the system with much more force at low frequency.

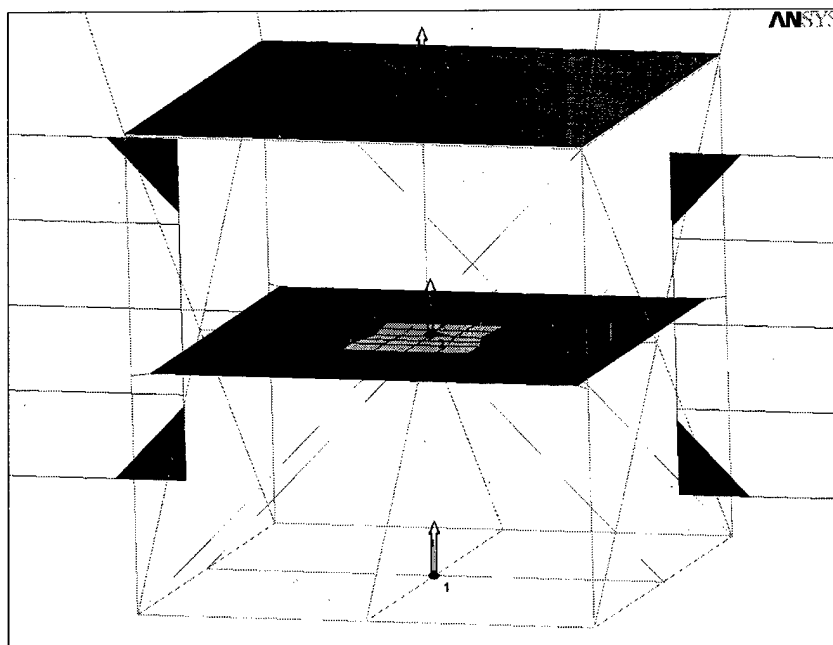


Figure 5.6: The dots with numbers show the location of the accelerometers that produced the output for the three transfer functions displayed below. The arrows indicate the orientation of the accelerometers as well as the shaker.

Three first generation model and data transfer functions for the global y-direction are shown below in Figure 5.7, Figure 5.8, and Figure 5.9. Figure 5.6 shows the location of the accelerometers for these transfer functions. Figure 5.7 shows the transfer function from the disturbance input to an accelerometer on the aluminum node that supports the shaker assembly. Figure 5.8 shows a transfer function to the node at the origin of the global coordinate system. Figure 5.9 shows the transfer function to the center of the top plate of the structure. In each figure the first three modes match well with the data, although the sensor collocated with the shaker (Figure 5.7) matches the data far better than the other two. Because the disturbance is nearly collocated with this accelerometer, the accuracy of the model at the bottom of the structure is not surprising.

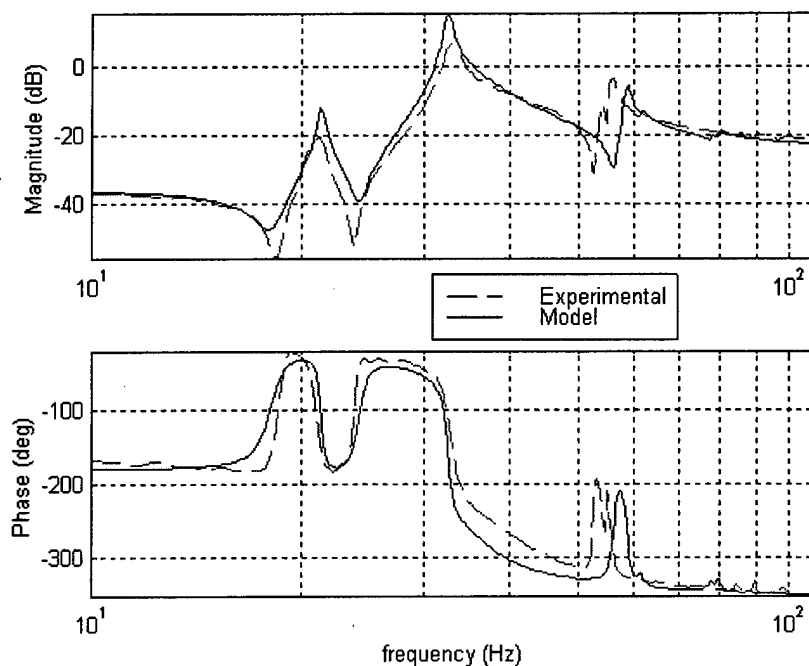


Figure 5.7: Experimental and model transfer function from the shaker voltage input an accelerometer at the bottom center node of the system. Both the shaker and sensor are oriented parallel to the y-axis in the global coordinate system.

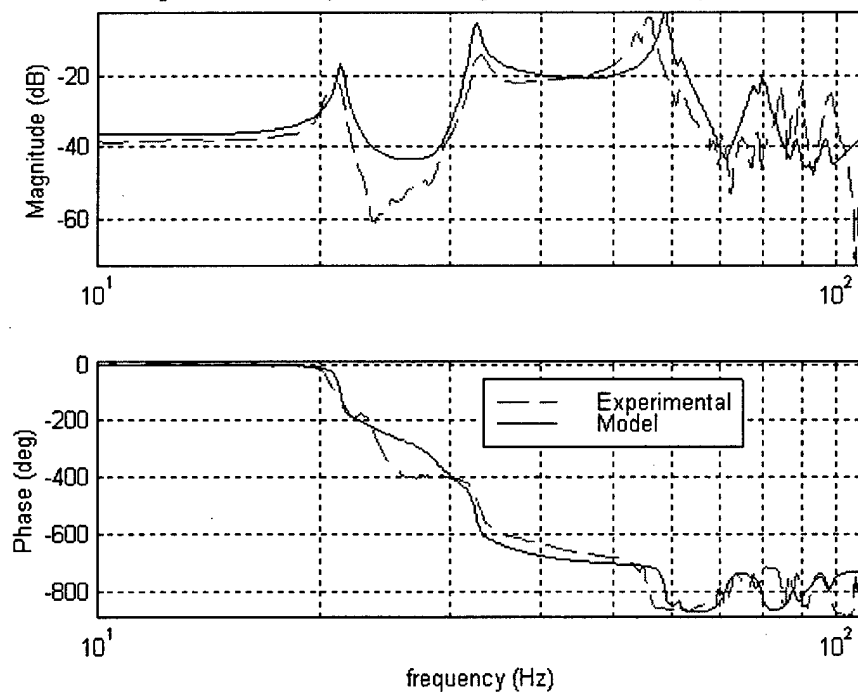


Figure 5.8: Experimental and model transfer function from the shaker voltage input to an accelerometer at the middle center node of the system. Both the shaker and sensor are oriented parallel to the y-axis in the global coordinate system.

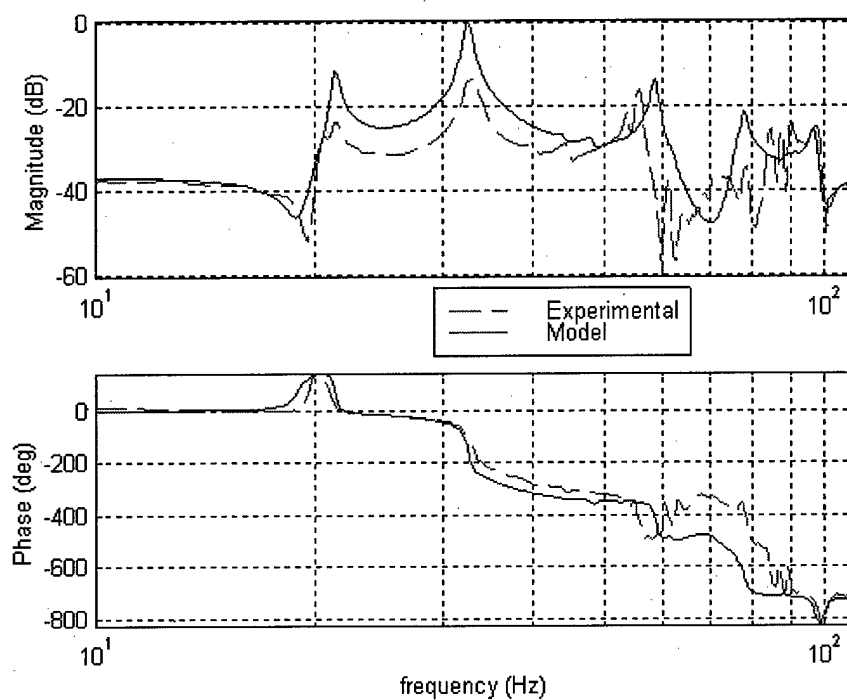


Figure 5.9: Experimental and model transfer function from the shaker voltage input to an accelerometer at the top center node of the system. Both the shaker and sensor are oriented parallel to the y-axis in the global coordinate system.

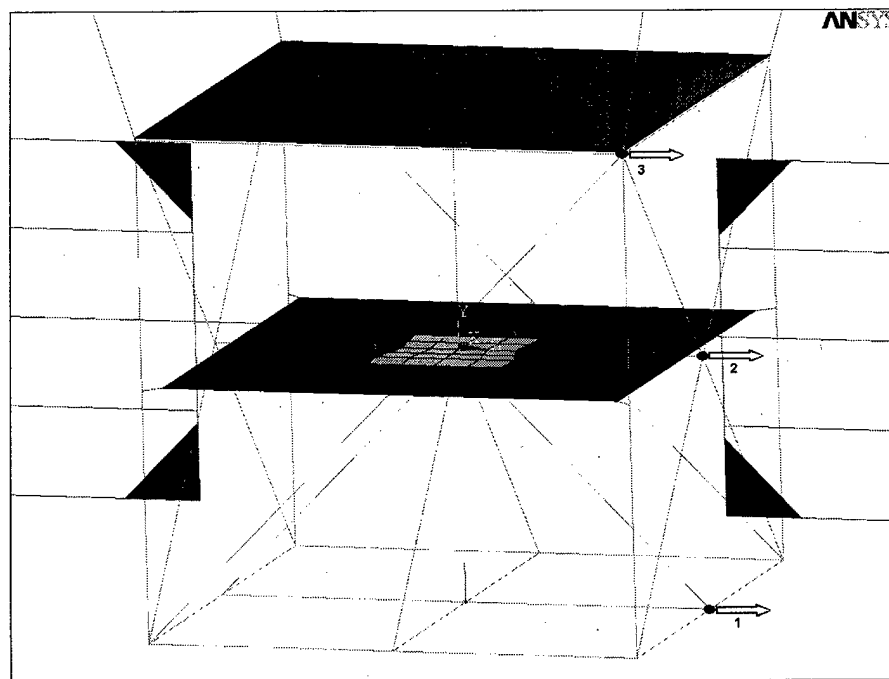


Figure 5.10: The dots with numbers show the location of the accelerometers that produced the three transfer functions displayed below. The arrows indicate the orientation of the accelerometers as well as the shaker.

Three transfer functions for the global z-direction are shown in Figure 5.11, Figure 5.12, and Figure 5.13 with the shaker rotated so that it aligns with the z-axis. Figure 5.10 shows the sensor locations for these transfer functions. The transfer function in Figure 5.11 is to the sensor at the bottom middle node on the positive z-axis side of the structure. In Figure 5.12 it is to the sensor at the middle node on the positive z-axis side of the structure. In Figure 5.13 it is to the sensor at the top corner on the positive z-axis side and negative x-axis side. Figure 5.11 shows the model matching the data much more closely than in the other figures, most likely a result of the sensor being closer to the disturbance source. The non-collocated sensors in Figure 5.12 and Figure 5.13 show that the first three modes match well, although the pole-zero structure for the sensor at the top of the structure (Figure 5.13) does not match well with the data. In each figure the phase plots match reasonably well.

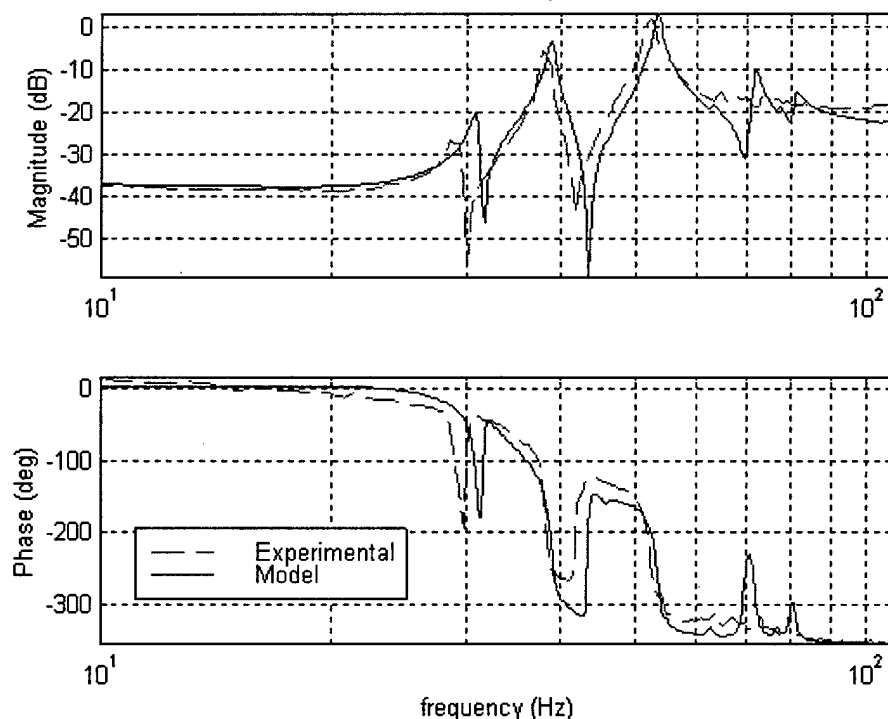


Figure 5.11: Experimental and model transfer function from the shaker voltage input to an accelerometer at the right bottom center node of the system. Both the shaker and sensor are oriented parallel to the z-axis in the global coordinate system.

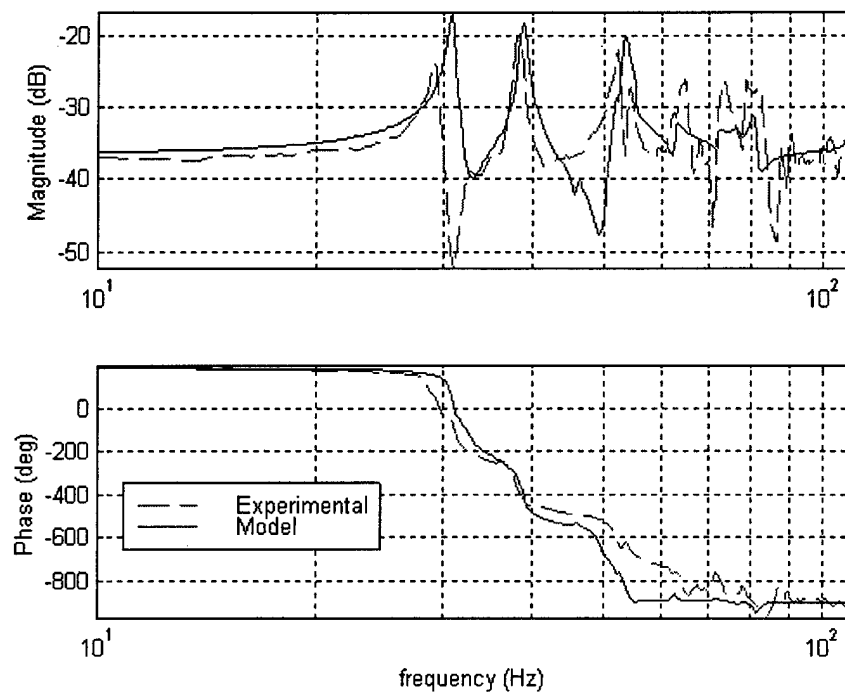


Figure 5.12: Experimental and model transfer function from the shaker voltage input an accelerometer at the right middle center node of the system. Both the shaker and sensor are oriented parallel to the z-axis in the global coordinate system.

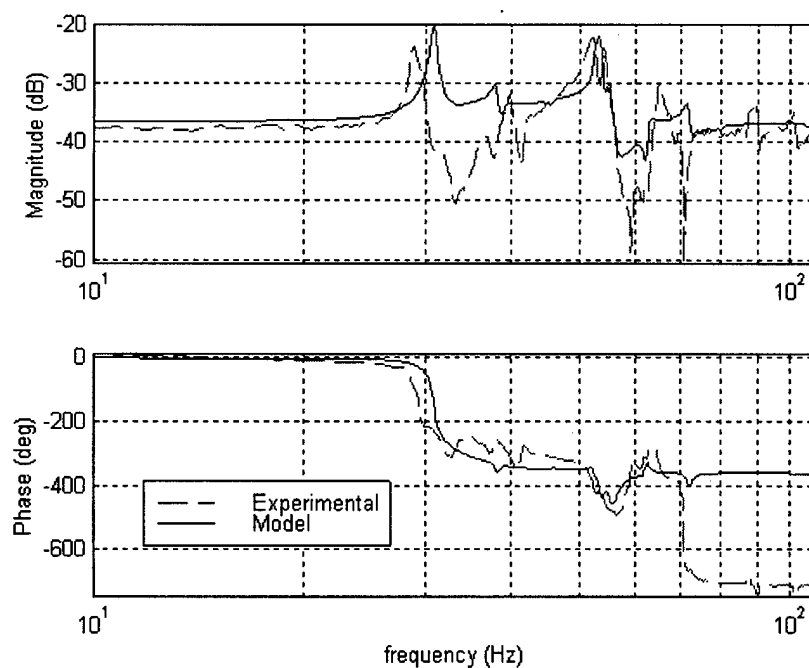


Figure 5.13: Experimental and model transfer function from the shaker voltage input to an accelerometer at the right top front node of the system. Both the shaker and sensor are oriented parallel to the z-axis in the global coordinate system.



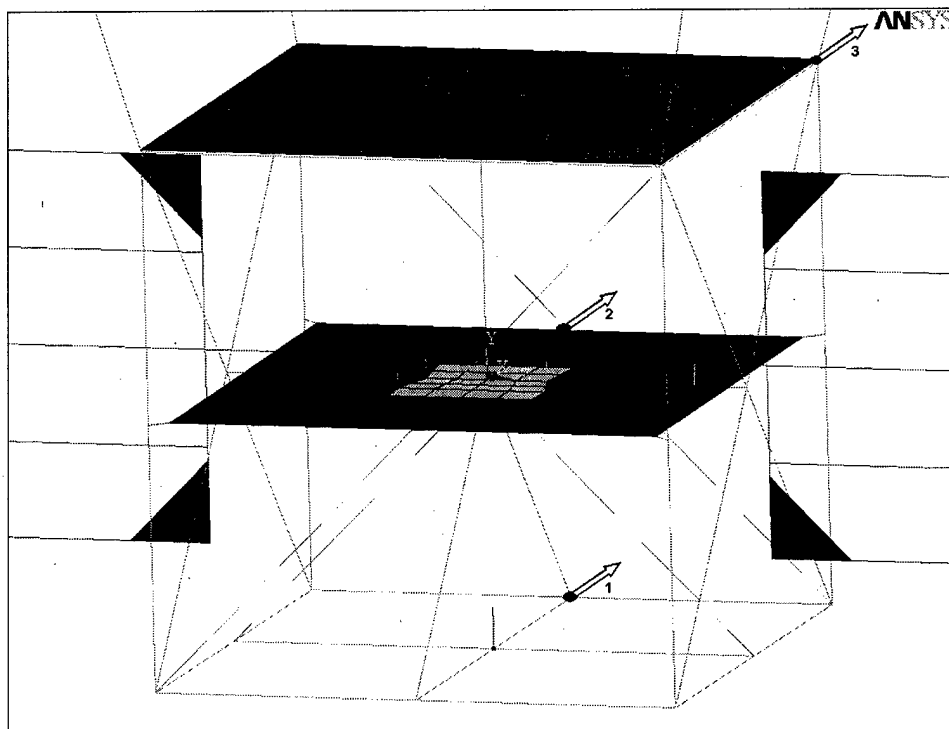


Figure 5.14: The dots with numbers show the location of the accelerometers that produced the three transfer functions displayed below. The shaker and the accelerometers are oriented in the global x-direction (positive to the back).

Three transfer functions for the global x-direction are shown below in Figure 5.15, Figure 5.16, and Figure 5.17. Figure 5.14 shows the sensor locations for these transfer functions. The transfer function in Figure 5.15 is to the sensor at the bottom middle node on the positive x-axis side of the structure. In Figure 5.16 it is to the sensor at the middle node on the positive x-axis side of the structure. In Figure 5.17 it is to the sensor at the top corner on the positive x-axis side and positive z-axis side. Figure 5.15 shows the model is a fair match with the data at frequencies above the first mode. The right pole-zero structure is present but the frequencies are noticeably shifted. Figure 5.16 and Figure 5.17 show that the model is again a fair match, but the modes are shifted and distinct zeros at 30Hz and 35 Hz are absent from the model. In each figure the phase plots match well, but the pole-zero structure at high frequency is not captured in the model transfer functions.

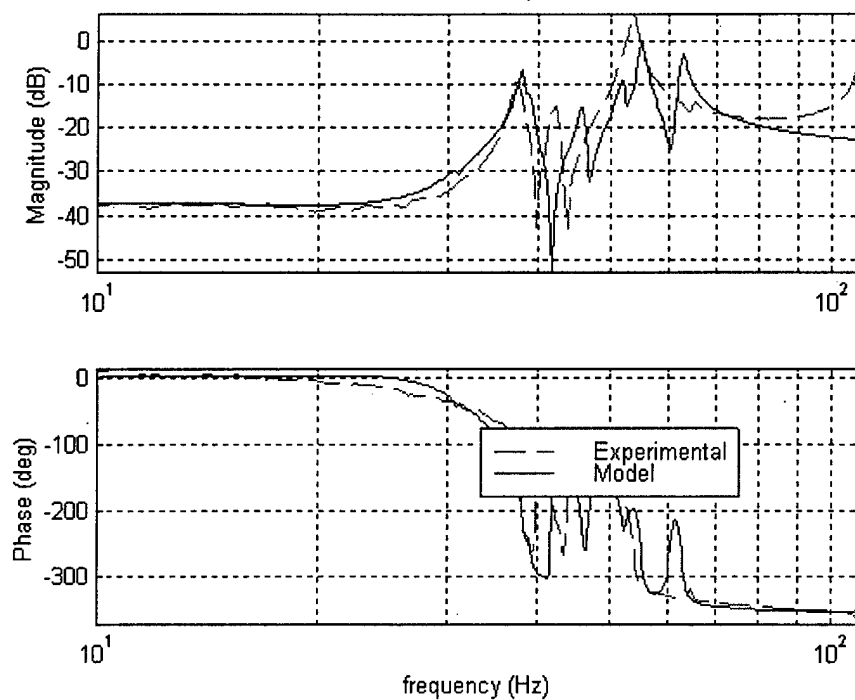


Figure 5.15: Experimental and model transfer function from the shaker voltage input to an accelerometer at the back bottom center node of the system. Both the shaker and sensor are oriented parallel to the x-axis in the global coordinate system.

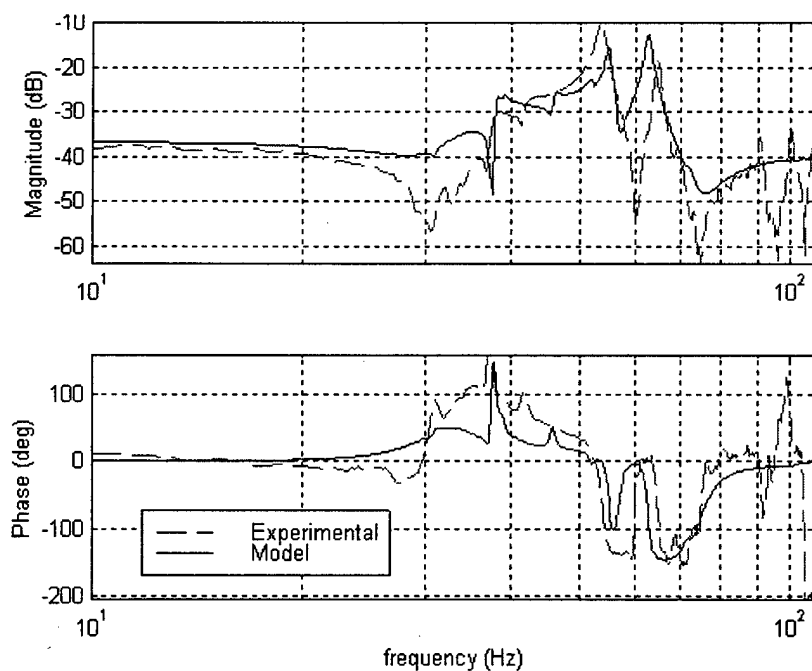


Figure 5.16: Experimental and model transfer function from the shaker voltage input to an accelerometer at the back middle center node of the system. Both the shaker and sensor are oriented parallel to the x-axis in the global coordinate system.

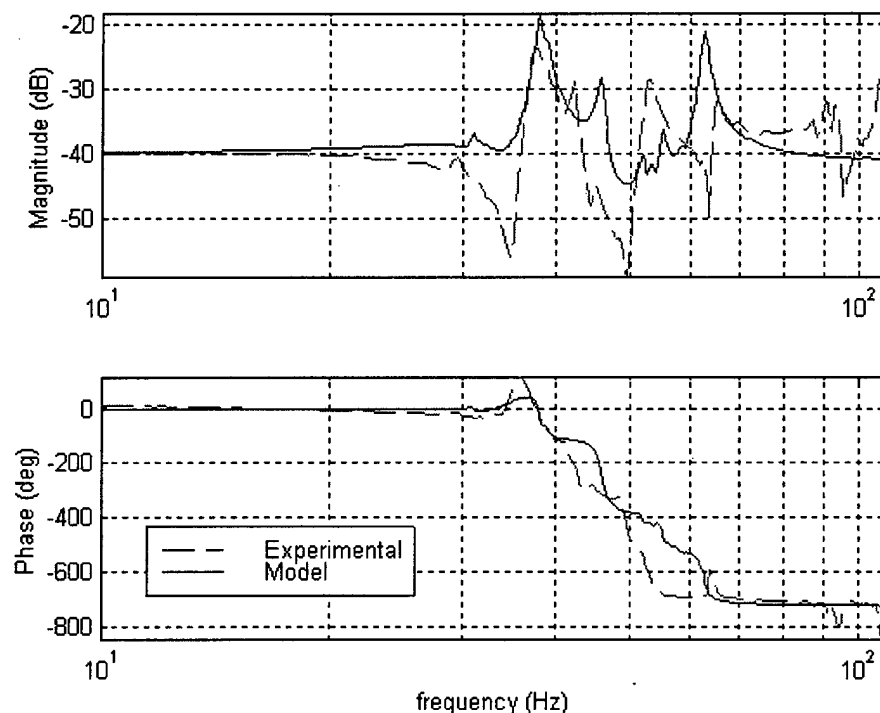


Figure 5.17: Experimental and model transfer function from the shaker voltage input to an accelerometer at the back top right node of the system. Both the shaker and sensor are oriented parallel to the x-axis in the global coordinate system.

There are a number of reasons why the model doesn't match the data exactly for every transfer function. The first is simply that there are inherent errors associated with discretizing a physical structure. The FEM is more likely to match lower frequency modes because the discretization errors become larger as the frequency increases. Second, there is a lot of uncertainty built into the model, particularly at the joints. The areas of high uncertainty were deliberately parameterized quite heavily so that a model update procedure could vary these parameters to help improve the model. Finally, the solar arrays are really free to rotate about the z-axis. However, the solar array connection is modeled as a rigid connection so that it is coupled to the rest of the system for the other five degrees of freedom. This boundary condition error might also affect the modeshapes of the model. Many of these problems can be improved by using a model update procedure on the FEM to improve the correlation between the model and the experimental plots.

## Chapter 6: Model Updating

This chapter describes the procedure used to update the model and improve the correlation between the FEM and the experimental data for the spacecraft test-bed. The parameters used to update the model are listed and described, and rationale for the selection of these parameters is explained. The mathematical method for the update procedure is briefly presented. The transfer functions from the updated finite element model are plotted on the same axes as experimental data and original model to show the effectiveness of the update. A comparison between modal frequencies of the experimental data, original model, and updated model is shown. A summary of the final element real-constant sets and material properties for the updated model is also presented.

### 6.1 Parameters Varied

The areas with highest uncertainty in the FEM of the spacecraft test-bed are highly parameterized. Each element type on the test-bed has at least 2 geometric properties, such as diameter and wall thickness, that can be varied independently. Each element type also has its own material properties that can vary independently. The joints are the most uncertain elements; thus, they are the most highly parameterized and densely meshed entities in the finite element model. Table 6.1 summarizes all parameters that were used in the model updating process, and lists the abbreviations used to reference the parameters in the following text.

Table 6.1: List of the parameters used in the model updating process.

| Parameter                         | Description   | Abbreviation     |
|-----------------------------------|---|------------------|
| Pipe flexibility factor           | Division factor for PIPE16 bending stiffness  | <i>Flex</i>      |
| Node wall thickness               | Wall thickness of element.  | <i>Node</i>      |
| Pipe-end wall thickness           | Wall thickness of the ends of the truss members   | <i>Ends</i>      |
| Middle plate thickness            | Thickness of the middle plate   | <i>Mid_plate</i> |
| Middle plate connection thickness | Thickness of the aluminum angles used to connect the middle plate to the truss          | <i>Mid_con</i>   |
| Disturbance node mass             | Mass added to the node supporting the shaker  | <i>Dist</i>      |
| Array drive shaft stiffness       | Stiffness of the steel shaft driving the solar arrays                                   | <i>Shaft</i>     |
| Bearing stiffness                 | Stiffness of the aluminum blocks modeling the pillow-block bearings for the array drive | <i>Bearing</i>   |
| Truss material stiffness          | Stiffness of the material that models the aluminum pipes, pipe ends, and nodes.         | <i>Stiff</i>     |
| Top plate stiffness               | Stiffness of the material in the top plate  | <i>Top_Stiff</i> |

The parameters *flex*, *node*, and *ends* were chosen to update the physical properties of all the major joints—where the most uncertainty exists. The parameters *mid\_plate* and *mid\_con* were chosen to improve the model's representation of the middle plate and the joints it shares with the truss. The parameters *stiff* and *top\_stiff* were chosen to affect the stiffness of nearly the whole structure without changing the amount of material. The *dist* parameter helps correct the error created by representing the shaker assembly with a solid aluminum beam. The assembly is actually heavier than the short beam in the model, and it is easier to vary a mass than an element cross-section. The two parameters *shaft* and *bearing* were chosen because the bearings that house the steel drive shafts have plastic linings much more flexible than steel. As a result, the actual stiffness of the joints connecting the arrays to the structure are much lower than the stiffness of steel. The shafts are very important because they transfer the higher frequency solar array dynamics to the main truss.

Other parameters could be updated as well, but the process was limited by time constraints as well as by the low number of experimental transfer functions used. Because only nine experimental transfer functions were used, the maximum number of parameters for each update step is eight (to maintain an over determined least-squares problem). Changing the parameters shown in Table 6.1 drastically affects areas of the model where uncertainty is high, which is the main reason these parameters were chosen.

## 6.2 Finite Difference Method

This section details the technique of updating the finite element model using the Finite Difference method in the frequency domain. For detailed coverage of the Finite Difference method reference the text by Crawley, Campbell, and Hall [4]. In this method, a new model is generated from the original model with one parameter slightly perturbed (1-5%). This is repeated for the total number of parameters being updated. A finite difference determines the change in the FEM due to the variation of individual parameters. Using the assumption that the updated model is simply a first order expansion of the original one, then,

$$G_{yw_u}(j\omega) = G_{yw_o}(j\omega) + \sum_{k=1}^n \frac{G_{yw_k}(j\omega) - G_{yw_o}(j\omega)}{\theta_k - \theta_{k_o}} \bullet \Delta\theta \quad (6.1)$$

where  $G_{yw_u}$  is the experimental transfer function from the  $w$ th input to the  $y$ th output of the updated model,  $G_{yw_k}$  is the transfer function of the perturbed model,  $G_{yw_o}$  is the transfer function of the original model,  $\theta_k$  and  $\theta_{k_o}$  are the values of the perturbed and original  $k$ th parameters respectively. There are  $n$  total parameters being updated, and  $\omega$  is a vector of frequencies identical to the frequency vector of the experimental transfer function. Then, a cost function is defined as,

$$J = \left\| \left[ G_{yw_d}(j\omega) \right] - \left[ G_{yw_o}(j\omega) \right] - \left[ \sum_{k=1}^n \frac{G_{yw_k}(j\omega) - G_{yw_o}(j\omega)}{\theta_k - \theta_{k_o}} \right] \Delta\theta \right\|^2 \quad (6.2)$$

where  $G_{yw_d}$  is the experimental data, and  $\Delta\theta$  is the column vector of parameters. Obviously, when  $\Delta\theta$  is zero and the model matches the data,  $J=0$  is at a minimum. The next step is to minimize this cost; as long as the initial model is close to the data (i.e. the modes are within a few percent), the updating process will converge to the best model possible, recommending new values for the given the set of parameters.

There are only nine experimental transfer functions—three x-disturbance to x-output, three y-disturbance to y-output, and three z-disturbance to z-output. The experimental and model transfer functions must be arranged so that the input-output characteristics for each SISO transfer function in the  $G_{yw_d}$ ,  $G_{yw_o}$ , and  $\partial G_k / \partial \theta_k$  vectors match up correctly. The input-output state space model for the FEM generates twenty-seven transfer functions, so care must be taken to extract the correct entries from the model to compare with the data. The cost function for the model updating procedure turns out to be equation 6.3 on the following page.

$$J = \left[ \begin{array}{c} G_{xx\_d1} \\ G_{xx\_d2} \\ G_{xx\_d3} \\ G_{yy\_d1} \\ G_{yy\_d2} \\ G_{yy\_d3} \\ G_{zz\_d1} \\ G_{zz\_d2} \\ G_{zz\_d3} \end{array} \right] - \left[ \begin{array}{c} G_{xx\_o1} \\ G_{xx\_o2} \\ G_{xx\_o3} \\ G_{yy\_o1} \\ G_{yy\_o2} \\ G_{yy\_o3} \\ G_{zz\_o1} \\ G_{zz\_o2} \\ G_{zz\_o3} \end{array} \right] - \left[ \begin{array}{ccc} \frac{\partial G_{xx1\_1}}{\partial \theta_1} & \dots & \frac{\partial G_{xx1\_8}}{\partial \theta_8} \\ \vdots & & \vdots \\ \frac{\partial G_{xx3\_1}}{\partial \theta_1} & & \frac{\partial G_{xx3\_8}}{\partial \theta_8} \\ \frac{\partial G_{yy1\_1}}{\partial \theta_1} & \dots & \frac{\partial G_{yy1\_8}}{\partial \theta_8} \\ \vdots & & \vdots \\ \frac{\partial G_{yy3\_1}}{\partial \theta_1} & & \frac{\partial G_{yy3\_8}}{\partial \theta_8} \\ \frac{\partial G_{zz1\_1}}{\partial \theta_1} & & \frac{\partial G_{zz1\_8}}{\partial \theta_8} \\ \vdots & & \vdots \\ \frac{\partial G_{zz3\_1}}{\partial \theta_1} & \dots & \frac{\partial G_{zz3\_8}}{\partial \theta_8} \end{array} \right] \left[ \begin{array}{c} \Delta \theta_1 \\ \Delta \theta_2 \\ \Delta \theta_3 \\ \Delta \theta_4 \\ \Delta \theta_5 \\ \Delta \theta_6 \\ \Delta \theta_7 \\ \Delta \theta_8 \end{array} \right]^2 \quad (6.3)$$

where the finite difference is given by,

$$\frac{\partial G_{k\_ywa}}{\partial \theta_k} = \frac{G_{ywa\_k} - G_{ywa\_o}}{\theta_k - \theta_{k\_o}} \quad (6.4)$$

where  $a$  corresponds to the number of the sensor used (1,2 or 3) to get the three experimental transfer functions in each direction. For example,  $G_{xx1\_2}$  corresponds to the transfer function for a x-input to a x-output, at the first sensor, for the model with the perturbed second parameter. The cost function can then be written using compact matrices, where  $\Delta G$  is the difference between the data and original model, and  $S$  is the finite difference matrix,

$$J = \|\Delta G - [S][\Delta \theta]\|^2 \quad (6.5)$$

which is in the form of a least squares problem. It can then be solved for  $\Delta \theta$  using the pseudo-inverse of the  $S$  matrix. The vector  $\Delta \theta$  is the recommended change in the parameters of the original model that minimizes the difference between the experimental and model transfer functions. The recommended changes are made to the original model, and then that model becomes the new "original" model for another update iteration.

Three m-files were written to perform the model updating procedure, each listed in Appendix B.

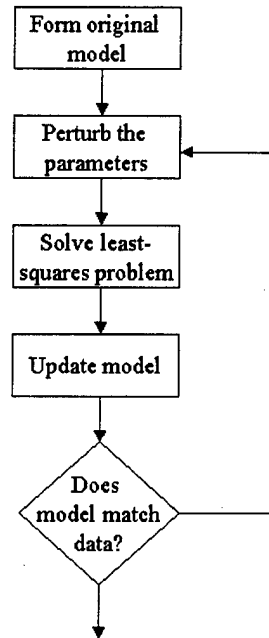


Figure 6.1: Flow Chart of the update process.

### 6.3 Updating Results

Using the nine experimental transfer functions shown in Chapter 5, three updating iterations were performed on the original finite element model. In each step, between five and eight of the ten parameters listed in Table 6.1 were varied separately to create slightly perturbed models. The modeshapes and natural frequencies were exported from ANSYS to MATLAB so that the perturbed state space models could be formulated. In the first iteration, the parameters were perturbed five percent, in the second two percent, and in the third two percent. The updating was restricted to the frequency range of 10-80Hz because the original model did not capture the higher frequency dynamics very well. One cannot expect updating to improve the model if the correct pole-zero structure does not exist, so the range from 80-110Hz in the data was omitted. The goal was to match the first three modes in each transfer function as well as possible, all of which are well below 80Hz.

The modal damping matrix was also updated (as needed) prior to each iteration, although not with a least-squares technique. The damping ratios for individual modes



were estimated using the half-power bandwidth of modes in the experimental transfer functions. The equation for estimating  $\zeta$  is,

$$\frac{1}{2\zeta_r} = \frac{\omega_r}{\omega_2 - \omega_1} \quad (6.6)$$

where  $\zeta_r$  is the damping ratio for the  $r$ th mode at the frequency  $\omega_r$ , and  $\omega_1$  and  $\omega_2$  are the frequencies of the half power points for the  $r$ th mode. This method provided an initial estimate for  $\zeta_r$ , the values of  $\zeta_r$  were then slightly varied to help match each model transfer function peak to a corresponding peak in the experimental data. The final damping ratios for each mode can be found in the *model\_create.m* m-file as well as Table 6.2.

The transfer function results from the update procedure are displayed in the same order as the original results shown in Chapter 5. The first three plots show transfer functions generated with sensors measuring acceleration in the global y-direction in response to a random y-disturbance input. In Figure 6.2, the model is nearly an exact match with the experimental data except for the depth of the zeros. The updated parameters successfully shifted the third mode from near 58 Hz in the original model, to 56 Hz to match the data. Again in Figure 6.3 and Figure 6.4, updating improved the model by aligning the 56Hz mode peaks. While the updated parameters align the peaks of the modes quite well, little is done to improve the correlation between the experimental and modeled zeros. This is most likely due to the fact that the low magnitude zeros are not weighted very well within the cost function when compared to the poles or peaks. There is a 40-80dB difference in some of the transfer functions. A possible solution to this problem is to use a logarithmic based cost function, which sometimes works well when identifying lightly damped zeroes in structural identification.

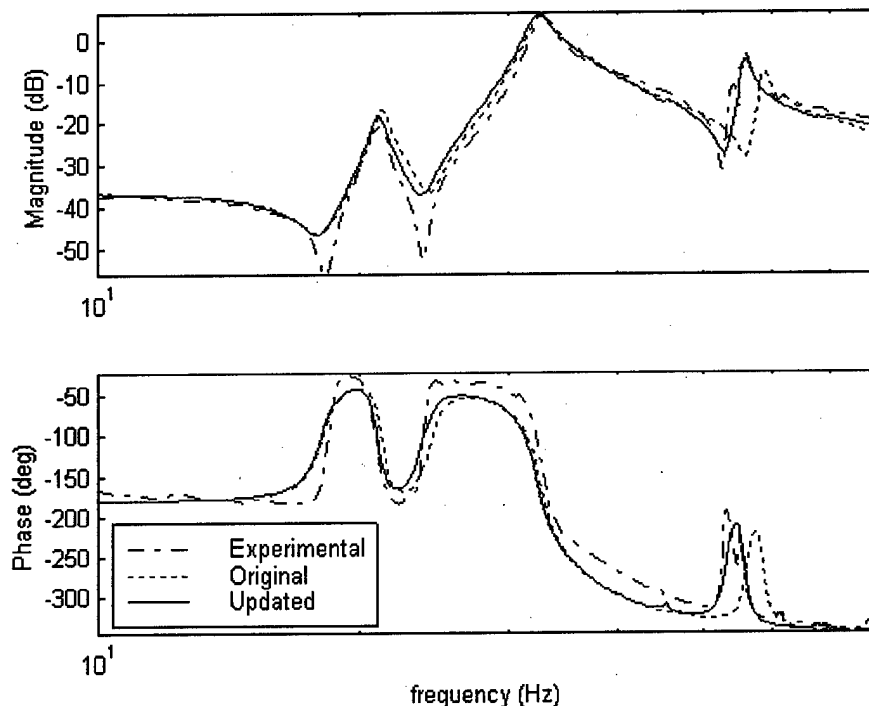


Figure 6.2: Experimental and model transfer functions from the shaker voltage input to an accelerometer at the bottom center node of the system. Both the shaker and sensor are oriented parallel to the y-axis in the global coordinate system.

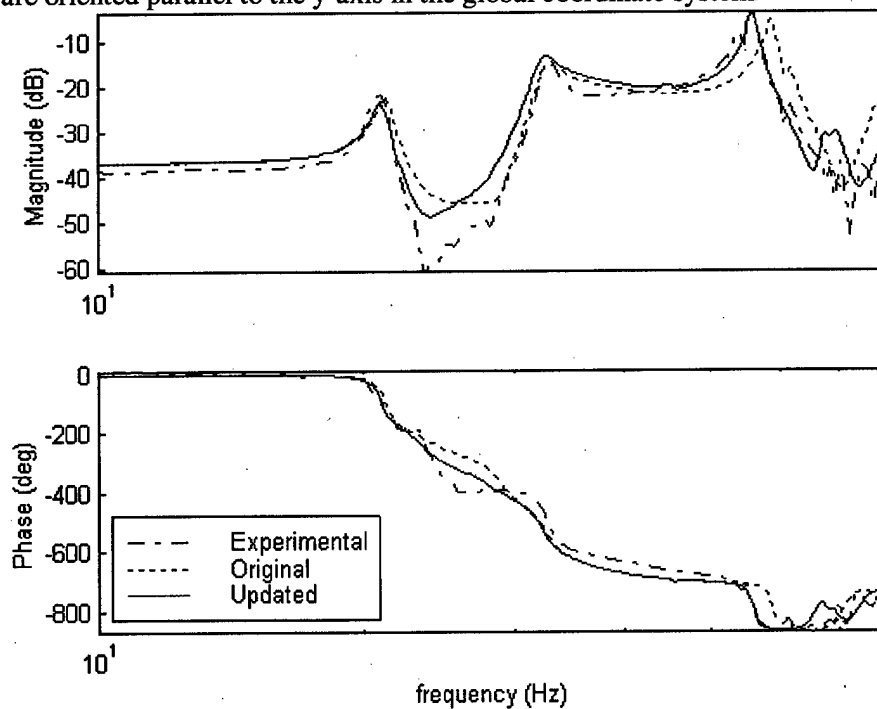


Figure 6.3: Experimental and model transfer function from the shaker voltage input to an accelerometer at the middle center node of the system. Both the shaker and sensor are oriented parallel to the y-axis in the global coordinate system.

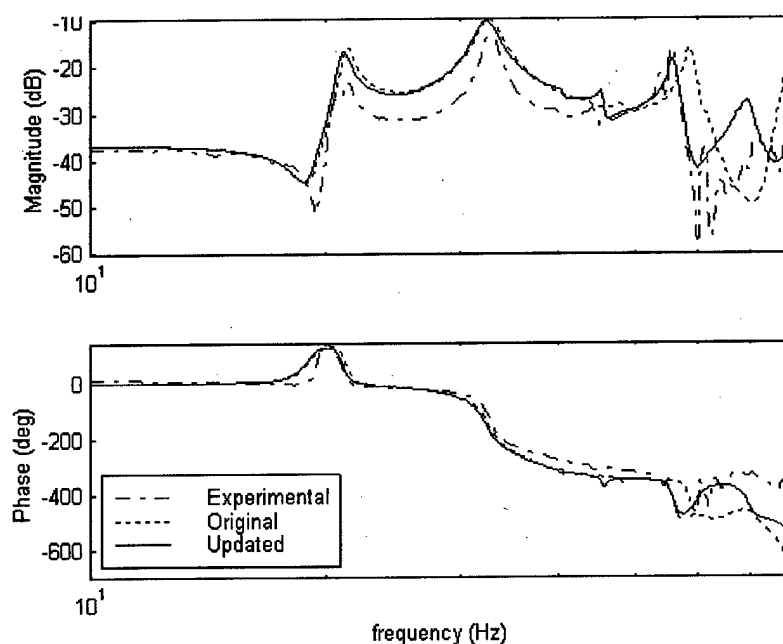


Figure 6.4: Experimental and model transfer function from the shaker voltage input to an accelerometer at the top center node of the system. Both the shaker and sensor are oriented parallel to the y-axis in the global coordinate system.

The next three plots show transfer functions generated with sensors measuring acceleration in the global z-direction in response to a random z-disturbance input. In Figure 6.5, the model again closely matches the experimental data. The model's first mode is slightly stiffer, and the pole-zero pattern between 60 Hz and 80 Hz is more pronounced than that in the data. The updated parameters successfully shifted the first three modes lower to help match the peaks better than the original model. In Figure 6.6, updating improved the model in the same manner as the previous plot because the first 3 modes were shifted to lower frequencies. However the zeros in Figure 6.6 do not match well, again most likely because of their lack of influence on the cost. Figure 6.7 shows the transfer function with the worst correlation between model and data. The first and third modes match well, but the pole-zero pattern between 30 Hz and 50 Hz does not. The phase plot also deviates significantly from the experimental data above 70 Hz. One reason for these discrepancies could be that the accelerometer was further from the disturbance source than the sensors that produced the previous two figures. The model may approximate the dynamics of the physical structure better near the disturbance source, but be more inaccurate further from the source.

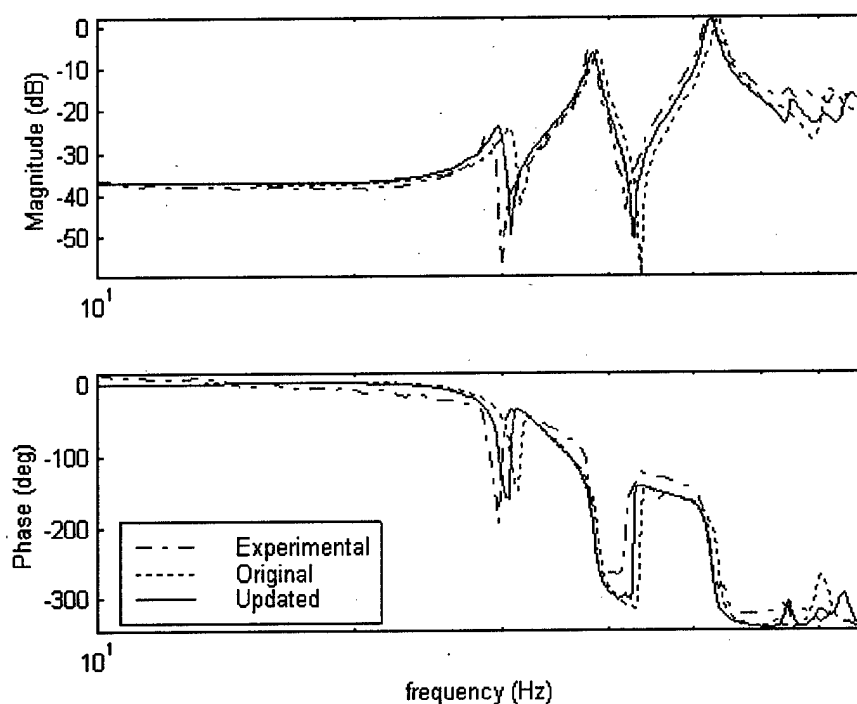


Figure 6.5: Experimental and model transfer function from the shaker voltage input to an accelerometer at the right bottom center node of the system. Both the shaker and sensor are oriented parallel to the z-axis in the global coordinate system.

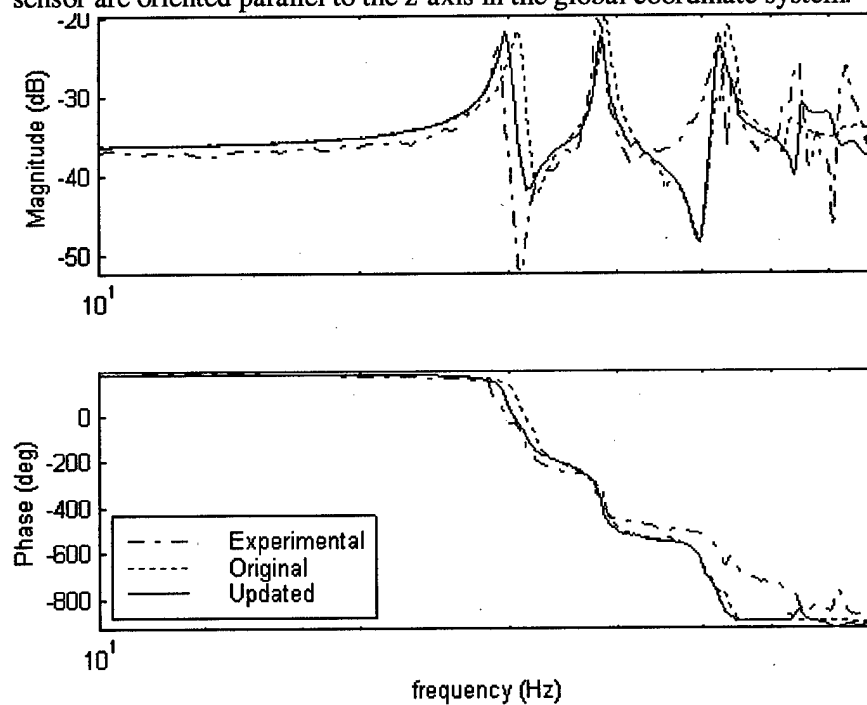


Figure 6.6: Experimental and model transfer function from the shaker voltage input to an accelerometer at the right middle center node of the system. Both the shaker and sensor are oriented parallel to the z-axis in the global coordinate system.

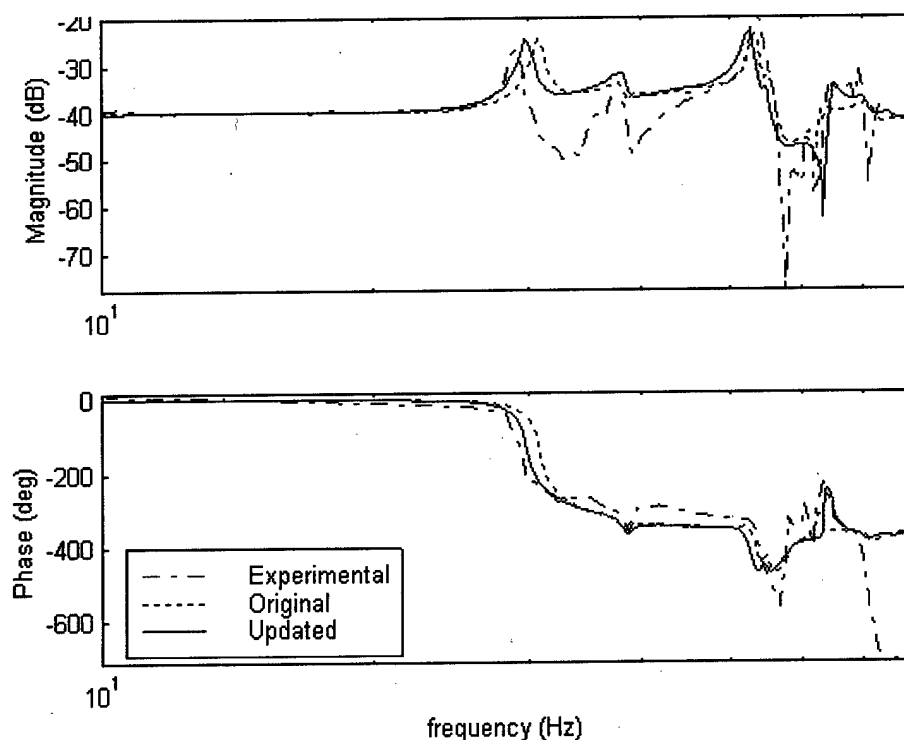


Figure 6.7: Experimental and model transfer function from the shaker voltage input to an accelerometer at the right top front node of the system. Both the shaker and sensor are oriented parallel to the z-axis in the global coordinate system.

The next three plots show transfer functions generated with sensors measuring acceleration in the global x-direction in response to a random x-input. In Figure 6.8 the updated model transfer function fits the experimental data much better than the original model. The first three modes all shifted to lower frequency to better match the data. Figure 6.10 shows the final model matching the experimental modal peaks, but the first experimental zero at 30 Hz is non-existent in the model. The phase plot matches well after the first major mode. Figure 6.10 also shows that the updated model captures the dynamics of the structure more accurately than the original model. The modal peaks match the data closely in this transfer function, but again the zeros are not quite as accurate.

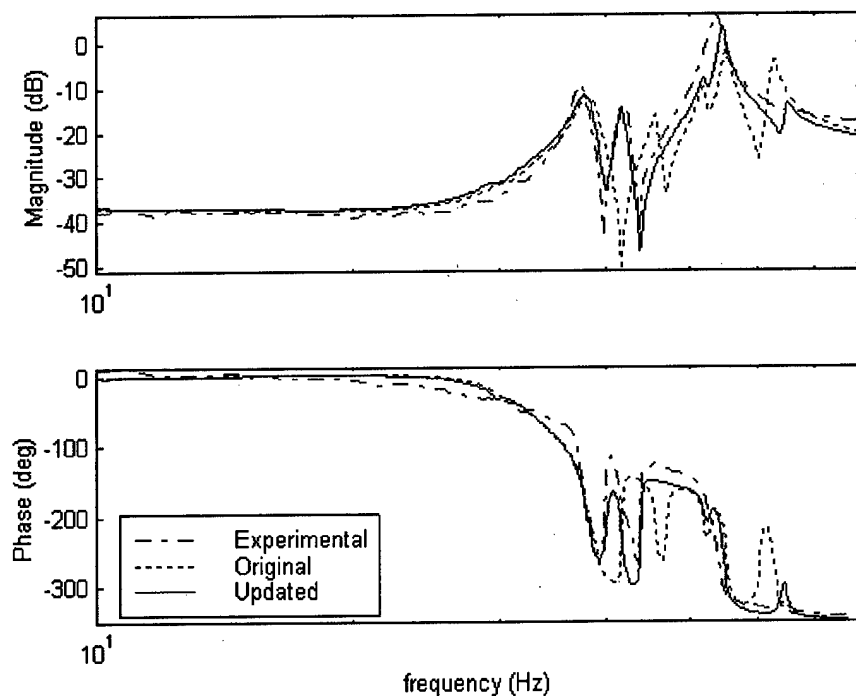


Figure 6.8: Experimental and model transfer function from the voltage input to the shaker to an accelerometer at the back bottom center node of the system. Both the shaker and sensor are oriented parallel to the x-axis in the global coordinate system.

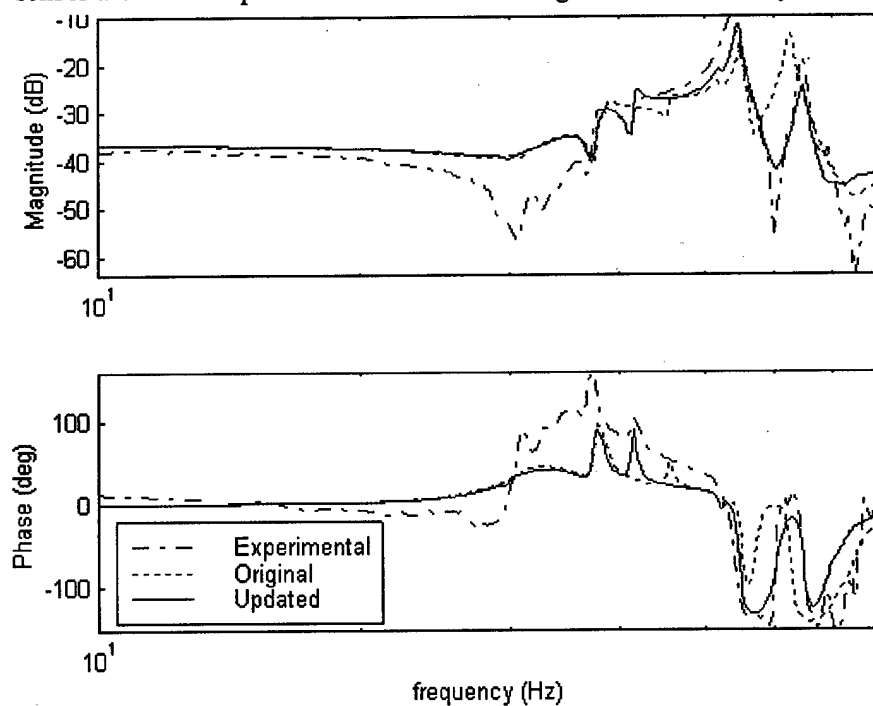


Figure 6.9: Experimental and model transfer function from the voltage input to the shaker to an accelerometer at the back middle center node of the system. Both the shaker and sensor are oriented parallel to the x-axis in the global coordinate system.

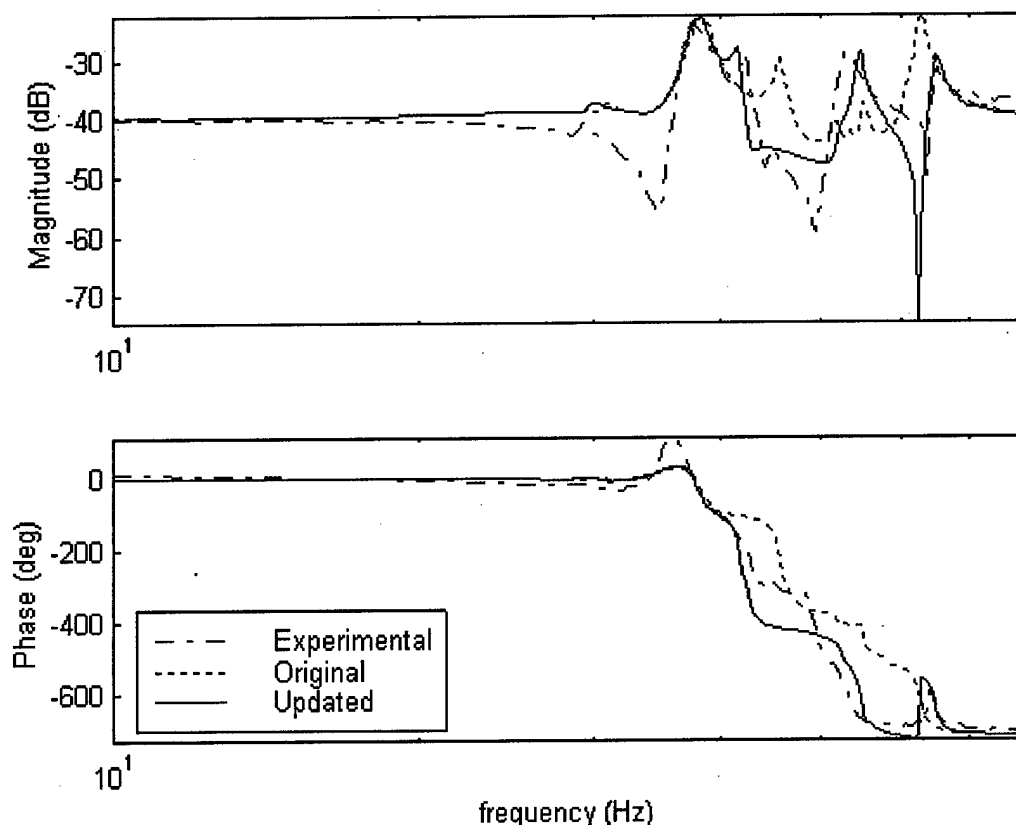


Figure 6.10: Experimental and model transfer function from the voltage input to the shaker to an accelerometer at the back top right node of the system. Both the shaker and sensor are oriented parallel to the x-axis in the global coordinate system.

The results of the updating procedure are summarized in Table 6.2. The first column is a list of the first four modes in each global direction (in the 10 Hz-110Hz frequency range). The percent error between each model and the experimental data is included in the table for easy comparison. The table shows that updating the model significantly reduced the error between the modal peaks of the model and experimental transfer functions. The average error for the updated model is significantly lower than the original model. The table also lists the final damping ratios assigned to the first four modes in each direction. The other modes were assigned a damping ratio of 0.01.

Table 6.2: This table lists the frequencies for the first four modes in each global direction for the original model, experimental data, and the updated model. The error reduction from updating the model listed as well as the damping ratio for each mode.

| Mode          | Experimental Data (Hz) | Original Model (Hz) | Error | Updated Model (Hz) | Error | Modal Damping Ratio ( $\zeta$ ) |
|---------------|------------------------|---------------------|-------|--------------------|-------|---------------------------------|
| Ux1           | 37.3                   | 38.1                | 2.1%  | 37.7               | 1.1%  | 0.017                           |
| Ux2           | 42.4                   | 45.8                | 8.0%  | 41.7               | 1.7%  | 0.009                           |
| Ux3           | 53.6                   | 55.1                | 2.8%  | 54.6               | 1.9%  | 0.01                            |
| Ux4           | 64.6                   | 62.7                | 2.9%  | 64.8               | 0.3%  | 0.01                            |
|               |                        |                     |       |                    |       |                                 |
| Uy1           | 21.1                   | 21.3                | 1.0%  | 21.1               | 0.0%  | 0.017                           |
| Uy2           | 32.5                   | 32.6                | 0.3%  | 32.3               | 0.6%  | 0.03                            |
| Uy3           | 56                     | 58.8                | 5.0%  | 56                 | 0.0%  | 0.013                           |
| Uy4           | 71                     | 77.6                | 9.3%  | 69.5               | 2.1%  | 0.02                            |
|               |                        |                     |       |                    |       |                                 |
| Uz1           | 28.7                   | 30.8                | 7.3%  | 29.7               | 3.5%  | 0.013                           |
| Uz2           | 37.8                   | 38.8                | 2.6%  | 38.3               | 1.3%  | 0.01                            |
| Uz3           | 53.5                   | 53.4                | 0.2%  | 52.6               | 1.7%  | 0.018                           |
| Uz4           | 64.3                   | 62.8                | 2.3%  | 64.8               | 0.8%  | 0.01                            |
| Average Error |                        |                     | 3.7%  |                    | 1.3%  |                                 |

## 6.4 Updated Finite Element Model Properties

Table 6.3 on the following page summarizes all information contained in the updated finite element model. The elements are listed according to the "real-constant" set number because this is how the elements are identified in the ANSYS graphical user interface. In Table 6.3,  $R_o$  refers to the outer radius of a pipe,  $wall$  refers to the wall thickness of a pipe or tube, and  $K$  is a spring constant. In the "material properties" column,  $E$  is the elastic modulus,  $G$  is the shear modulus, and  $\rho$  is the density. The highlighted real-constants and material properties were the parameters varied in the model updating process. Table 6.4 summarizes the changes made to these parameters.



Table 6.3: Summary of the finite element model information for the updated model.

| Real Constant # | Element Type | Part the Element Models  | Real Constant Values  | Material Properties   |
|-----------------|--------------|--|---|---|
| 1               | Pipe16       | The full diameter portion of the main truss members                  | $R_o=30\text{mm}$<br>Wall=1.5mm<br><b>Flex Factor=1.827</b> | $E=70\text{e9 N/m}^2$<br>$G=26\text{e9 N/m}^2$<br>$\rho=2800 \text{ kg/m}^3$  |
| 2               | Beam4        | The solar arrays' long square aluminum tubes                         | 25.4mm x 25.4mm<br>Wall=1.4mm                               | $E=70\text{e9 N/m}^2$<br>$G=26\text{e9 N/m}^2$<br>$\rho=2800 \text{ kg/m}^3$  |
| 3               | Shell63      | The middle aluminum plate  | <b>Thickness=5.6mm</b>                                      | $E=72\text{e9 N/m}^2$<br>$G=26\text{e9 N/m}^2$<br>$\rho=2800 \text{ kg/m}^3$  |
| 4               | Shell63      | The top aluminum plate   | Thickness=7.8mm   | $E=70\text{e9 N/m}^2$<br>$G=25\text{e9 N/m}^2$<br>$\rho=2800 \text{ kg/m}^3$  |
| 5               | Beam4        | The solar array drive shafts   | $R=12.7\text{mm}$ (solid)                                   | $E=76\text{e9 N/m}^2$<br>$G=80\text{e9 N/m}^2$<br>$\rho=7800 \text{ kg/m}^3$  |
| 7               | Beam4        | The aluminum bearing mounts and bearings                             | 38.1mm x 38.1mm<br>(solid)                                  | $E=49\text{e9 N/m}^2$<br>$G=26\text{e9 N/m}^2$<br>$\rho=2800 \text{ kg/m}^3$  |
| 8               | Beam4        | Stiffened aluminum square tubing at the solar array attachment point | 25.4mm x 25.4mm<br>Wall=3.9mm wall                          | $E=72\text{e9 N/m}^2$<br>$G=26\text{e9 N/m}^2$<br>$\rho=2800 \text{ kg/m}^3$  |
| 9               | Shell63      | Triangular steel solar array stiffeners                              | Thickness=2.8mm   | $E=210\text{e9 N/m}^2$<br>$G=80\text{e9 N/m}^2$<br>$\rho=7800 \text{ kg/m}^3$ |
| 11              | Combin14     | Main suspension springs  | $K=490 \text{ N/m}$   | N/A   |
| 12              | Combin14     | Solar array support suspension springs (deleted from the model)      | $K=22 \text{ N/m}$  | N/A   |
| 13              | Mass21       | Mass added to the attachment point of the shaker assembly            | <b>0.62kg</b>   | N/A   |
| 14              | Beam4        | Shaker assembly  | 76.2mm x 76.2mm<br>(solid)                                  | $E=70\text{e9 N/m}^2$<br>$G=26\text{e9 N/m}^2$<br>$\rho=2800 \text{ kg/m}^3$  |
| 15              | Beam4        | Small beam that attaches the middle plate to the truss nodes         | <b>7.01mm</b> x 25.4mm<br>(solid)                           | $E=70\text{e9 N/m}^2$<br>$G=25\text{e9 N/m}^2$<br>$\rho=2800 \text{ kg/m}^3$  |
| 17              | Beam4        | The ends of the truss members  | $R_o=8.25\text{mm}$<br><b>Wall=4.92mm</b>                   | $E=70\text{e9 N/m}^2$<br>$G=26\text{e9 N/m}^2$<br>$\rho=2800 \text{ kg/m}^3$  |
| 18              | Beam4        | The aluminum truss nodes   | $R_o=22.2\text{mm}$<br><b>Wall=3.3mm</b>                    | $E=70\text{e9 N/m}^2$<br>$G=26\text{e9 N/m}^2$<br>$\rho=2800 \text{ kg/m}^3$  |
| 19              | Mass21       | Added mass to the middle joint on the middle plate                   | 0.5kg   | N/A   |
| 20              | Shell63      | Part of the middle plate around the center truss node                | Thickness=4.5mm   | $E=72\text{e9 N/m}^2$<br>$G=26\text{e9 N/m}^2$<br>$\rho=2800 \text{ kg/m}^3$  |
| 21              | Beam4        | Joint at the center of the structure                                 | $R_o=8.25\text{mm}$<br>Wall=1.75mm                          | $E=70\text{e9 N/m}^2$<br>$G=26\text{e9 N/m}^2$<br>$\rho=2800 \text{ kg/m}^3$  |

Table 6.4: Summary of change in the parameters.

| <b>Parameter</b> | <b>Original Value</b> | <b>Updated Value</b> | <b>Change</b> |
|------------------|-----------------------|----------------------|---------------|
| <i>Flex</i>      | 1.5                   | 1.827                | 22%           |
| <i>Node</i>      | 1.6mm                 | 3.3mm                | 106%          |
| <i>Ends</i>      | 3.75mm                | 4.92mm               | 31%           |
| <i>mid_plate</i> | 5.7mm                 | 5.6mm                | -2%           |
| <i>mid_con</i>   | 6.35mm                | 7.01mm               | 10%           |
| <i>Dist</i>      | 0.8kg                 | 0.62kg               | -22%          |
| <i>Shaft</i>     | 210GPa                | 76Gpa                | -64%          |
| <i>Bearing</i>   | 70Gpa                 | 49Gpa                | -30%          |
| <i>Stiff</i>     | 72Gpa                 | 70Gpa                | -3%           |
| <i>Top_Stiff</i> | 72Gpa                 | 70Gpa                | -3%           |

## Chapter 7: Conclusions and Recommendations

### 7.1 Conclusions

The spacecraft test-bed described in this thesis will be an effective platform for conducting vibration isolation and pointing research with the UW hexapod. The test-bed can mimic typical spacecraft disturbances such as reaction wheel imbalances, fluid slosh, solar array drive mechanical vibration, and low frequency coupling with the solar array modes. The structure's dimensions and mass are representative of a "typical" precision pointing spacecraft. Furthermore, the test-bed's suspension system approximates the 0-g environment with very low frequency bounce and pendulum modes, and offers adjustability to ensure the hexapod top plate can be properly aligned with the base of the hexapod. With these features, the test-bed provides a more realistic setting in which to test the effectiveness of six-axis active vibration isolation and pointing technology. With this test-bed more practical results can now be achieved when conducting research with the UW hexapod.

The spacecraft test-bed is even more useful for future research because of the finite element model developed for the structure. Finite element modeling was effective in capturing the dynamics of the spacecraft test-bed, because care was taken to minimize errors in the assumptions used to create the model. Comparing experimental data with the model verified that the model does capture the dynamics of the physical structure well in the range of 10 to 80 Hz; the average error for the first twelve flexible modes of the system was 3.7%. The finite element model of the test-bed structure can be combined with the existing model of the hexapod in order to conduct vibration and pointing research based on a model of the integrated system's dynamics. The model also serves as a baseline to compare with system identification methods used to capture the dynamics of the model.

The finite element model was significantly improved with the model updating process. Updating parameters in high uncertainty areas, such as the structure's joints, helped to shift the poles of the model's transfer functions to better correspond with the experimental data. The average error for the first twelve flexible modes was improved

from 3.7% to 1.3% as a result of model updating. Updating also helped compensate for the inaccuracy of the finite element model's representation of the solar array attachment. The plastic lining of the pillow block bearings that support each array drive shaft is much less stiff than steel, and model updating indicated that the stiffness of the drive shafts should be reduced so that the model would improve. Despite the procedure's success in improving the location of the model's poles, the zeros of the model do not match the data quite as well as desired. One explanation for this problem is that the zeros do not influence the cost function as much, because their magnitudes are 40-80dB less than the poles.

## 7.2 Recommendations

There are areas for improvement in both the physical structure and the finite element model of the spacecraft test-bed. The following are several specific areas for improvement, followed by a more detailed discussion of each. First, despite careful attention to boundary conditions, there are still uncertainties in the boundary of the model that should be revised. Second, improvements can also be made in the process used to update the finite element model. Third, the hexapod should be added to the model of the spacecraft test-bed, and different orientations of the solar arrays should be investigated. All data was collected with the arrays oriented parallel to the vertical plane, and the finite element model only captures the dynamics of this orientation.

Two boundary conditions are poorly addressed in the finite element model. The first is the omission of the soft springs that provide added support for the solar arrays. These springs were not included because they caused numerical problems with the ANSYS solver. If included, the elements that modeled the springs caused the ratio of the stiffest to least-stiff element in the model to exceed  $10^8$ ; significant round-off errors can result when this ratio exceeds  $10^8$ . The second error is in how the arrays attach to the truss structure in the model. The arrays are free to rotate about the z-axis on the physical structure, but the connection is modeled with a typical six degree-of-freedom node. The most appropriate approach to modeling this connection is separate finite element models connected subsequently in MATLAB while allowing the rotation degree of freedom to be

free. The model would improve if either of these boundary condition problems could be solved.

The model updating process produced good results, but can be improved. The process's worst fault is that it consumes too much time. Perturbing a single parameter in the model, obtaining the modal analysis solution, and saving the frequencies and modeshapes requires 25 to 30 minutes. If seven or eight parameters are perturbed, the process becomes very time consuming for a single iteration. The process could be significantly improved if there were a way to automate saving the ANSYS results files. One solution might be to write ANSYS batch files that automatically saves the frequencies and each mode shape in a separate file. With this improvement, more experimental transfer functions could be used which would then increase the number of allowable parameters in each iteration. There certainly could be more parameters included in the update process if this improvement were made. The number of experimental transfer functions must increase if more parameters are used.

The finite element model of the test-bed would be more useful if the hexapod's base and top plates were included. There is currently a model of the hexapod struts and top plate, so the hexapod's bottom plate should be added to the spacecraft test-bed structure before an attempt is made to combine the two models. Adding the base plate to the test-bed presents a difficult modeling challenge because some of the mass (the electronics boxes) is not rigidly attached to the plate. It will also be difficult to quantify the effect of the hexapod's cabling on the structure.

The problems described in the preceding paragraphs should be addressed before any active vibration isolation and pointing research resumes. In the meantime, the spacecraft test-bed also provides an excellent platform for system identification research. The structure is very clean without the hexapod, and produces clean experimental transfer functions. System identification techniques could be used as an independent method for validating the accuracy of the current finite element model.

## Bibliography

- [1]. ANSYS *Elements Reference*. 001084. 10th ed. Houston, PA: Swanson Analysis Systsems Inc., [1999]
- [2]. Blevin, Robert D. *Formulas for Natural Frequencies and Mode Shape*. Malabar, Florida: R.E. Krieger, 1979.
- [3]. Blackwood, G.H., S. Dubovitsky, R.P. Linfield, and P.W. Gorham. "Interferometer Instrument Design for New Millennium Deep Space 3." In *Astronomical Interferometry: Proceedings of the Meeting in Kona, Hawaii, March 20-24, 1998*, by the Society of Photo-Optical Instrumentation Engineers (SPIE), 173-183. Bellingham, Washington: SPIE, 1998.
- [4]. Crawley, E., M. Campbell, and S. Hall. *High Performance Structures: Dynamics and Control*. (to be published) Massachusetts: Cambridge University Press, 1999.
- [5]. Friswell, M., and J. Mottershead. *Finite Element Model Updating in Structural Dynamics*. Boston, MA: Kluwer Academic Publishers, 1995.
- [6]. Golden, Daniel S. "Origins." Database on-line. Available from <http://origins.jpl.nasa.gov/index.html>, August 1999.
- [7]. Hauge, Geir S. "Six-Axis Active Vibration Isolation for Spacecraft." M.S. thesis, University of Washington, 1999.
- [8]. Jacobs, J., T. Hyde, J. Boyd, S. Hadden, and L. Davis. "Structural Control of a Flexible Satellite Bus for Improved Jitter Performance." In *Smart Structures and Materials 1998: Industrial and Commercial Applications of Smart Structures Technologies: Proceedings of the Meeting in San Diego, California, March 3-5, 1998*, by the Society of Photo-Optical Instrumentation Engineers (SPIE), 93-104. Bellingham, Washington: SPIE, 1998.
- [9]. Larson, Wiley J., and James R. Wertz. *Space Mission Analysis and Design*, 2d ed. Torrance, CA: Microcosm, Inc., 1992.
- [10]. Lau, Kenneth, Stephen Lichten, Lawrence Young, and Bruce Haines. "An Innovative Deep Space Application of GPS Technology for Formation Flying Spacecraft." In *Guidance, Navigation and Control: Proceedings of the Conference in San Diego, California, July 29-31, 1996*, by the American Institute of Aeronautics and Astronautics (AIAA), 1-9. Reston, Virginia: AIAA, 1996.
- [11]. Peralta, Renee. "Micro Precision Interferometer Testbed." Database on-line. Available from <http://huey.jpl.nasa.gov/itp/www/mpi/index.html>. August 1999.

- [12]. O'Brien, John F., Renaud Goullioud, and Gregory W. Neat. "Micro-Precision Interferometer: Evaluation of New Disturbance Isolation Solutions." In *Smart Structures and Materials 1998: Passive Damping and Isolation: Proceedings of the Meeting in San Diego, California, March 2-3, 1998*, by the Society of Photo-Optical Instrumentation Engineers (SPIE), 387-398. Bellingham, Washington: SPIE, 1998.
- [13]. Patterson, David P. "Teledesic: A Global Broadband Network." In *Aerospace Conference: Proceedings of the Meeting in Aspen, Colorado, March 21-28, 1998*, by the Institute of Electrical and Electronics Engineers (IEEE), 547-552. Piscataway, New Jersey: IEEE, Inc., 1998.
- [14]. Sellers, P. *Understanding Space: An Introduction to Astronautics*. New York: McGraw Hill, 1994.
- [15]. Skormin, V. A., M. A. Tascillo, and T.E. Busch. "Demonstration of a Jitter Rejection Technique for Free-Space Laser Communication." *IEEE Transactions on Aerospace and Electronic Systems*: vol 33, no. 2, (April 1997): 568-575.
- [16]. "Space Technology 3." Database on-line. Available from <http://spacetechnology3.jpl.nasa.gov/indexm.html>, August 1999.
- [17]. Sullivan, Jeanne M., James Goodding, Michelle Idle, Alok Das, Terance Hoffman, and L. Porter. "Performance Testing for an Active/Passive Vibration Isolation and Steering System." In *Dynamics Specialists: Proceedings of the Conference in Salt Lake City, Utah, 18-19 April, 1996*, by the American Institute of Aeronautics and Astronautics (AIAA), 87-97. Reston, Virginia: AIAA, 1996.
- [18]. Thayer, Doug G. "Multi-Sensor Control for 6-Axis Active Vibration Isolation." Ph.D. diss., University of Washington, 1998.
- [19]. Unwin, S., and R. Danner. "SIM: Taking the Measure of the Universe." Database on-line. Available from <http://sim.jpl.nasa.gov/library/intro-overview.html>, December 1998.
- [20]. Van Allen, Robert L., and James D. Dillow. "Pointing and Tracking Technology in Evolution Performance and Promise." In *Annual Rocky Mountain Guidance and Control Conference: Proceedings of the Meeting in Keystone, Colorado, February 1-5, 1995*, by the American Astronautical Society (AAS), 1-19. San Diego, California: AAS, 1995.
- [21]. *Visual Analysis Reference Manual*. Bozeman, Montana: Integrated Engineering Software, [1998].

## Appendix A. Modeling M-files

The following m-files were used to verify the model of the electromagnetic shaker as well as to setup the state space model of the FEM and overlay model transfer functions on experimental data.

```
%-----
%1 September 1999
%Clint ZumBrunnen
%Thesis Work
%
%check_shake.m
%
%This m-file overlays the experimental transfer function
%for the voice coil disturbance generator with a model
%that is used in conjunction with the FEM of the structure.
%
%The data file is called shaker.mat and must be present in
%the Exp_data directory.
%-----

%Load the right data file
file2=('shaker');
file2=['e:\thesis\matlab\no_hextop\truss_only\exp_data\' ,file2];
load (file2);

fp=401;
w_e=o2ilx(1:fp,:);

%Convert the data to decibels and unwrapped phase
mag_e=20*log10(abs(o2il));
phase_e=unwrap(angle(o2il))*180/pi+360;;

%Plot the experimental data
subplot(211),
semilogx(w_e(1:fp,:),mag_e(1:fp:),'b--')
title('Transfer function from input voltage to acceleration output
[a(t)/e(t)]');
grid on
hold on
axis tight
subplot(212),
semilogx(w_e(1:fp,:),phase_e(1:fp:),'b--')
grid on
hold on
axis tight

%Create the model of the electromagnetic shaker in TF form
v_c=tf([.00005 0 0],[1/220^2 2*.17/220 1]);
[mag_s,phase_s,w]=bode(v_c,2*pi*w_e);
w=w/(2*pi);
```



```
%Convert the model to the same form as the data
mag_s=20*log10(squeeze(mag_s));
phase_s=squeeze(phase_s);

%Overlay the model on the data
subplot(211),
semilogx(w(1:fp,:),mag_s(1:fp:),'r')
grid on
hold on
axis tight
subplot(212),
semilogx(w(1:fp,:),phase_s(1:fp:),'r')
hold on
grid on
axis tight
```

```

%-----
%August 1999
%Clint ZumBrunnen
%Thesis Work
%
%Get_phi.m
%
%This m-file imports the phi matrix to MATLAB
%
%This m-file must reside in the same directory as the modeshapes
%extracted from ANSYS. The user must manually input the number
%of modes and nodes for the model.
%-----
n=1124; %number of nodes
modes=80; %number of modes
t=1;
p=1;
j=1;
new=[];
phi_t=[];
phi=[];
%Loop to extract the modeshapes from the ANSYS output file
for t=1:modes;
    file=[(num2str(t)),'.txt'];
    fid=fopen(file,'r');
    format short

    i=1;
    for i=1:41;
        fscanf(fid,'%s1');
        i=i+1;
    end
    phi_t=(fscanf(fid,'%12g'));
    for p=1:(ceil(n/37)-1)
        i=1;
        for i=1:35;
            fscanf(fid,'%s1');
            i=i+1;
        end
        phi_t=[phi_t; (fscanf(fid,'%12g'))];
        p=p+1;
    end
    %Loop to get rid of the nodal numbers in the matrix so that
    %only DOFs are left.
    for j=1:n
        new=[new; phi_t((j-1)*7+2:(j-1)*7+7,1)];
        j=j+1;
    end
    phi_t=[];
    phi_t=new;
    new=[];
    phi=[phi phi_t];
    t=t+1;
end
clear phi_t

```

```

%-----
%August 1999
%Clint ZumBrunnen
%Thesis work
%
%Get_freqs.m
%
%This m-file creates the frequency matrix (Wr)
%
%This m-file requires that the file Get_phi.m be run first
%
%-----

new=[];
modes=min(size(phi));      %number of modes extracted
file=['freqs.txt'];
fid=fopen(file,'r');       %open the right file
format short

%Loop to load the frequencies from the ANSYS output
i=1;
for i=1:15;
    fscanf(fid,'%s1');      %scan out all the text junk
    i=i+1;
end
Wr=(fscanf(fid,'%12g'));   %get all the numbers

for j=1:modes
    new=[new; Wr((j-1)*5+2,1)];
    j=j+1;
end
Wr=new;

```

```

%-----
%August 1999
%Clint ZumBrunnen
%Thesis work
%
%pre_model_x.m
%
%Setup the right Disturbance direction, node, and output direction
%
%-----

DOFs=max(size(phi));           %number of nodal DOFs
n=max(size(Wr));               %number of expanded modes

dist_node=input('Node where disturbance enters: ');
    %node where disturbance enters
dist_direct = input('Input Disturbance DOF: ','s');
%X,Y,Z,ROTX,ROTY,ROTZ
output_direct = input('Input Output DOF: ','s');

if dist_direct=='Ux'
    i_DOF=0;
elseif dist_direct=='Uy'
    i_DOF=1;
elseif dist_direct=='Uz'
    i_DOF=2;
elseif dist_direct=='Rotx'
    i_DOF=3;
elseif dist_direct=='Roty'
    i_DOF=4;
elseif dist_direct=='Rotz'
    i_DOF=5;
end

if output_direct=='Ux'
    o_DOF=0;
elseif output_direct=='Uy'
    o_DOF=1;
elseif output_direct=='Uz'
    o_DOF=2;
elseif output_direct=='Rotx'
    o_DOF=3;
elseif output_direct=='Roty'
    o_DOF=4;
elseif output_direct=='Rotz'
    o_DOF=5;
end

node=[929 902 855 4 2 5 519 745 517];
num_data=max(size(node));

```

```

%-----
%August 1999
%Clint ZumBrunnen
%Thesis work
%
%model_create.m
%
%State Space Model of Test-Bed without Hexapod Top
%For use with the truss_only models with 1124 nodes
%Disturbance enters at node 1123 for Uy, and 1124 for Ux,Uz
%Run this file after loading the phi and Wr matrices from
%the <nominal>,<update1>,< update2>,or <update3> directories
%
%The m-files get_phi and get_freqs must run prior to this
%file in the directory. The m-file pre_model_x,
%pre_model_y, or pre_model_z must also run prior to this
%file to define the nodes on the FEM that match the data
%sets.
%
%-----

%Create Damping Matrix
    z=0.01;
    W=diag(Wr)*2*pi;
    Cr=-2*z*W;

%-----For loop to generate plots of all data at one time--
    %p=input('Input the # of the set of data to overlay: ');
    for p=1:num_data
        %fix=input('Input the phase fix: ');
        fix=0;

%defines the right node for output
output_node = node(p);

%-----Import the Experimental Data file-----
file=[output_direct num2str(p)];
file2=['e:\thesis\matlab\no_hextop\truss_only\exp_data\' ,file];
load (file2);

fp=max(size(o2ilx));
w_e=o2ilx;

mag_e=20*log10(abs(o2il));
phase_e=unwrap(angle(o2il))*180/pi+fix;
points=logspace(1,log10(max(w_e)),fp);           %create a logspace with
equal number of points

%-----Create the model I/O system to overlay----

%Create the state space model for the shaker input
    [As,Bs,Cs,Ds]=tf2ss(.00005*[1 0 0 ],[1/220^2 2*.17/220 1]);
    sys_s=ss(As,Bs,Cs,Ds);
    Ka=1/9.8;
%Define the disturbance input matrix for the test-bed

```

```

beta=[zeros(1,(dist_node-1)*6+i_DOF) 1 zeros(1,DOFs-((dist_node-
1)*6+i_DOF+1))]; %direction at bottom middle node

%Define the output matrices for the test-bed
Cyn=Ka*[zeros(1,(output_node-1)*6+o_DOF) 1 zeros(1,DOFs-
((output_node-1)*6+o_DOF+1))];
Cyn_dot=[zeros(1,DOFs)];

%Create the A and B matrices for the FEM State Space Model
A=[zeros(n,n) eye(n,n);
   -W^2      -2*z*W];
B=[zeros(n,1);phi'*beta*.07*1/Ka];

%For formulate the C and D matrices for acceleration output.
%Add in the 0.07kg factor to convert the acceleration input from
%the shaker to a force input.
C=[Cyn*phi*[-W^2 -2*z*W]];
D=[Cyn*phi*phi'*beta*.07*1/Ka];

%Combine the two state space models and add a D correction term
d_cor=input(['Input D correction factor for data set ',file,': ']);
d_cor=0.01;
mod=ss(A,B,C,D);
sys=sys_s*mod;
[An,Bn,Cn,Dn]=ssdata(sys);
Dn=Dn+d_cor;
sys=ss(An,Bn,Cn,Dn);

%Format the model data to overlay on experimental data
fig_num=p;
figure(fig_num)
[mag,phase,w]=bode(sys,2*pi*w_e);
w=w/(2*pi);
mag=20*log10(squeeze(mag));
phase=squeeze(phase);

%plot the experimental data
subplot(211),
semilogx(w_e,mag_e,'r--')
title([dist_direct,' disturbance to ',output_direct,' output at node
',num2str(output_node)]);
hold on
subplot(212),
semilogx(w_e,phase_e,'r--')
hold on

%plot the model results
subplot(211)
semilogx(w,mag,'b-')
ylabel('Magnitude (dB)')
axis tight
grid on
subplot(212)
semilogx(w,phase,'b-')
ylabel('Phase (deg)')

```

```
xlabel('frequency (Hz)')  
axis tight  
grid on  
legend('Experimental','Model',0);  
p=p+1;
```

## Appendix B. Updating M-files

The following m-files perform the model updating process.

```
%-----
%August 1999
%Clint ZumBrunnen
%Thesis work
%
%pre_update.m
%
%This m-file loads the phi and Wr matrices for each of the
%perturbed models used in the updating process. It also creates
%the matrix 'theta' which is the amount each parameter changed.
%Then the file calls <update.m>.
%
%-----
clear all
theta=[];
Wr7=[];

cd update1
get_phi;
get_freqs;

cd ..
cd theta1
get_phi;
get_freqs;
theta(1)=-.02*1.8269;      %flexibility factor

cd ..
cd theta2
get_phi;
get_freqs;
theta(2)=-.02*.0033;      %node wall thickness

cd ..
cd theta3
get_phi;
get_freqs;
theta(3)=-.02*.004915;    %truss member end wall thickness

cd ..
cd theta4
get_phi;
get_freqs;
theta(4)=-.02*.0056;      %middle plate thickness

cd ..
cd theta5
get_phi;
get_freqs;
```



```
theta(5)=-.02*.62;      %disturbance node mass

cd ..
cd theta6
get_phi;
get_freqs;
theta(6)=-.02*81;      %solar array drive shaft stiffness

cd ..
cd theta7
get_phi;
get_freqs;
theta(7)=-.02*50;      %solar array drive shaft stiffness

cd ..

update
```

```

%-----
%August 1999
%Clint ZumBrunnen
%Thesis work
%
%update.m
%
%This m-file carries out the updating process. It loads the
%experimental data, creates the nominal state space model, calls
%<delta_models.m> to load the perturbed state space models, and then
%solves the linear least squares problem with the pseudo inverse.
%
%-----
clear a* A* b* B* c* C* d* D* e* E* f* F* g* G* h* H* i* I* j* J* k* K*
clear l* L* m* M* n* N* o* O* q* Q* r* R* s* S* u* U* v* V*
clear p w w_e z

%-----Form G_data-----
data=[];
sets=[2 5 7 2 14 26 2 5 7];
for p=1:3;
    cd exp_data
    file=['Ux', num2str(sets(p)), '.mat'];
    load (file)
    data=[data abs(o2i1)];
    cd ..
end

for p=4:6;
    cd exp_data
    file=['Uy', num2str(sets(p)), '.mat'];
    load (file)
    data=[data abs(o2i1)];
    cd ..
end

for p=7:9;
    cd exp_data
    file=['Uz', num2str(sets(p)), '.mat'];
    load (file)
    data=[data abs(o2i1)];
    cd ..
end
data=data(1:280,:);
w_e=o2i1x;
w_e=w_e(1:280,1);
G_data=[data(:,1);
        data(:,2);
        data(:,3);
        data(:,4);
        data(:,5);
        data(:,6);
        data(:,7);
        data(:,8);
        data(:,9)];

```

```

%-----Create the nominal I/O system model-----

%-----Create the state space model for the shaker input-----
[As,Bs,Cs,Ds]=tf2ss(.00005*[1 0 0 ],[1/220^2 2*.17/220 1]);
sys_s=ss(As,Bs,Cs,Ds);

%-----Define the disturbance input matrix for the test-bed-----
DOFs=max(size(phi));
dist_node=1124;
beta=zeros(1,(dist_node-1)*6) 1 0 0 zeros(1,DOFs-((dist_node-1)*6+3));
      zeros(1,(dist_node-1)*6) 0 1 0 zeros(1,DOFs-((dist_node-1)*6+3));
      zeros(1,(dist_node-1)*6) 0 0 1 zeros(1,DOFs-((dist_node-1)*6+3));
%-----Input is at the bottom center node

%-----Define the output matrices for the test-bed-----
output_node=[902 2 12 911 3 217 920 4 13]; %[Ux1 Ux2 Ux3 Uy1 Uy2 Uy3 Uz1 Uz2 Uz3]
Cyn=Ka*[zeros(1,(output_node(1)-1)*6) 1 0 0 zeros(1,DOFs-((output_node(1)-1)*6+3));
      zeros(1,(output_node(1)-1)*6) 0 1 0 zeros(1,DOFs-((output_node(1)-1)*6+3));
      zeros(1,(output_node(1)-1)*6) 0 0 1 zeros(1,DOFs-((output_node(1)-1)*6+3));
      zeros(1,(output_node(2)-1)*6) 1 0 0 zeros(1,DOFs-((output_node(2)-1)*6+3));
      zeros(1,(output_node(2)-1)*6) 0 1 0 zeros(1,DOFs-((output_node(2)-1)*6+3));
      zeros(1,(output_node(2)-1)*6) 0 0 1 zeros(1,DOFs-((output_node(2)-1)*6+3));
      zeros(1,(output_node(3)-1)*6) 1 0 0 zeros(1,DOFs-((output_node(3)-1)*6+3));
      zeros(1,(output_node(3)-1)*6) 0 1 0 zeros(1,DOFs-((output_node(3)-1)*6+3));
      zeros(1,(output_node(3)-1)*6) 0 0 1 zeros(1,DOFs-((output_node(3)-1)*6+3));
      zeros(1,(output_node(4)-1)*6) 1 0 0 zeros(1,DOFs-((output_node(4)-1)*6+3));
      zeros(1,(output_node(4)-1)*6) 0 1 0 zeros(1,DOFs-((output_node(4)-1)*6+3));
      zeros(1,(output_node(4)-1)*6) 0 0 1 zeros(1,DOFs-((output_node(4)-1)*6+3));
      zeros(1,(output_node(5)-1)*6) 1 0 0 zeros(1,DOFs-((output_node(5)-1)*6+3));
      zeros(1,(output_node(5)-1)*6) 0 1 0 zeros(1,DOFs-((output_node(5)-1)*6+3));
      zeros(1,(output_node(5)-1)*6) 0 0 1 zeros(1,DOFs-((output_node(5)-1)*6+3));
      zeros(1,(output_node(6)-1)*6) 1 0 0 zeros(1,DOFs-((output_node(6)-1)*6+3));
      zeros(1,(output_node(6)-1)*6) 0 1 0 zeros(1,DOFs-((output_node(6)-1)*6+3));
      zeros(1,(output_node(6)-1)*6) 0 0 1 zeros(1,DOFs-((output_node(6)-1)*6+3));
      zeros(1,(output_node(7)-1)*6) 1 0 0 zeros(1,DOFs-((output_node(7)-1)*6+3));
      zeros(1,(output_node(7)-1)*6) 0 1 0 zeros(1,DOFs-((output_node(7)-1)*6+3));
      zeros(1,(output_node(7)-1)*6) 0 0 1 zeros(1,DOFs-((output_node(7)-1)*6+3));
      zeros(1,(output_node(8)-1)*6) 1 0 0 zeros(1,DOFs-((output_node(8)-1)*6+3));
      zeros(1,(output_node(8)-1)*6) 0 1 0 zeros(1,DOFs-((output_node(8)-1)*6+3));
      zeros(1,(output_node(8)-1)*6) 0 0 1 zeros(1,DOFs-((output_node(8)-1)*6+3));
      zeros(1,(output_node(9)-1)*6) 1 0 0 zeros(1,DOFs-((output_node(9)-1)*6+3));
      zeros(1,(output_node(9)-1)*6) 0 1 0 zeros(1,DOFs-((output_node(9)-1)*6+3));
      zeros(1,(output_node(9)-1)*6) 0 0 1 zeros(1,DOFs-((output_node(9)-1)*6+3))];

%-----Create the updated damping matrix-----
z=ones(80,1)*.01;
z(12)=.017;
z(13)=.013;
z(14)=.03;
z(15)=.0172;
z(16)=.01;

```

```

z(17)=.01;
z(18)=.009;
z(19)=.01;
z(20)=.01;
z(21)=.01;
z(22)=.018;
z(23)=.01;
z(24)=.01;
z(25)=.0124;
z(26)=.01;
z(27)=.01;
z(28)=.02;
z(29)=.02;
z(30)=.01;
z(31)=.01;
z(32)=.02;
z(34)=.01;
z=diag(z);
W=diag(Wr)*2*pi;
Cr=-2*z*W;
n=max(size(Wr));

%-----Create the A and B matrices for the FEM State Space Model-----

A=[zeros(n,n) eye(n,n);
   -W^2        -2*z*W];
B=[zeros(n,3);phi'*beta*.07*1/Ka];

%For formulate the C and D matrices for acceleration output.
%Add in the 0.07kg factor to convert the acceleration input from
%the shaker to a force input.
C=[Cyn*phi*[-W^2 -2*z*W]];
D=[Cyn*phi*phi'*beta*.07*1/Ka];

%Combine the two state space models and add a D correction term

%-----Create d_cor matrix-----
d_cor=zeros(27,3);
d_cor(1,1)=.015;
d_cor(4,1)=.015;
d_cor(7,1)=.01;
d_cor(11,2)=-.015;
d_cor(14,2)=.015;
d_cor(17,2)=.015;
d_cor(21,3)=.015;
d_cor(24,3)=-.015;
d_cor(27,3)=.01;

%-----Create state space system for nominal model-----
mod=ss(A,B,C,D);
sys=sys_s*mod;
[An,Bn,Cn,Dn]=ssdata(sys);
Dn=Dn+d_cor;
sys=ss(An,Bn,Cn,Dn);

```

```
%-----Extract the correct transfer functions from the model-----  
[mag,phase,w]=bode(sys,w_e*2*pi);  
G_nominal=[squeeze(mag(1,1,:));  
squeeze(mag(4,1,:));  
squeeze(mag(7,1,:));  
squeeze(mag(11,2,:));  
squeeze(mag(14,2,:));  
squeeze(mag(17,2,:));  
squeeze(mag(21,3,:));  
squeeze(mag(24,3,:));  
squeeze(mag(27,3,:))];  
  
delta_models  
  
%-----Solve the linear least squares problem with the pseudo-inverse--  
change=pinv(delta)*([G_data-G_nominal])
```

```

%-----
%August 1999
%Clint ZumBrunnen
%Thesis work
%
%delta_models.m
%
%This m-file (called by the m-file <update.m>) creates the updated
%damping matrix for the perturbed models, and then creates each
%perturbed model. The plotting routine at the end was added to
%insure that the transfer functions extracted from the state space
%model were the right ones to correspond with the data
%
%-----
delta=[];
Wr_theta=[Wr1 Wr2 Wr3 Wr4 Wr5 Wr6 Wr7];
phi_theta=[phi1 phi2 phi3 phi4 phi5 phi6 phi7];
num_w=length(w_e);
G_new=[];

%-----Create the models with perturbed parameters-----

for k=1:7
phi_loop=phi_theta(:,((k-1)*80+1):k*80);
%-----Create the damping matrix
    z=ones(80,1)*.01;
    z(12)=.017;
    z(13)=.013;
    z(14)=.03;
    z(15)=.0172;
    z(16)=.01;
    z(17)=.01;
    z(18)=.009;
    z(19)=.01;
    z(20)=.01;
    z(21)=.01;
    z(22)=.018;
    z(23)=.01;
    z(24)=.01;
    z(25)=.0124;
    z(26)=.01;
    z(27)=.01;
    z(28)=.02;
    z(29)=.02;
    z(30)=.01;
    z(31)=.01;
    z(32)=.02;
    z(34)=.01;
    z=diag(z);
    W=diag(Wr_theta(:,k))*2*pi;
    Cr=-2*z*W;
    n=max(size(Wr));

%-----Create the A and B matrices for the FEM State Space Model

```